Observability of narrow $X \to t\bar{t}$ resonances from theories beyond the Standard Model at LHC with CMS

Petra Van Mulders

Promotors : Jorgen D'Hondt en Stefaan Tavernier

VRIJE UNIVERSITEIT BRUSSEL · SCIENTIA VINCERE TENEBRAS ·

juni, 2006

Vakgroep Natuurkunde
Faculteit van de Wetenschappen
Vrije Universiteit Brussel

Proefschrift ingediend met het oog op het behalen
van de Wettelijke Graad van Licentiaat in de Natuurkunde

Contents

Introduction

In the past decades, physicists extensively tested the Standard Model of elementary particle physics with very high precision. No discrepancies with the Standard Model predictions were observed. However, physicists believe that the Standard Model is not the complete answer to our questions. The Standard Model doesn't provide a complete theory of Nature, as for example the gravitational force is not included. Many models are proposed as an extension of the Standard Model. These models need experimental verification, which becomes possible in the range of energy the Large Hadron Collider at CERN is designed to explore from its starting date in 2007. With the discovery of the top quark at the Tevatron, a new field of top quark physics is opened. The large mass of the top quark is very close to the electroweak symmetry breaking scale. This suggests that the top quark may play a special role in the symmetry breaking mechanism providing masses to the particles in the Standard Model. In addition, the particles predicted in some models beyond the Standard Model may couple preferentially to the top quark, which makes it an interesting field of research. An interesting part of the verification of these models is to study the observability of new resonances decaying into top quarks in the environment of a realistic detector. This study is the subject matter of this thesis.

In the first chapter a summary of the Standard Model is given with its virtues and its shortcomings as a motivation that the model should be extended. An example of a possible extension of the Standard Model will be given in the second chapter. Technicolor models are summarized and the Z' boson on which the study is applied is introduced. The third chapter deals with the experimental environment for the verification of new physics. The main properties of the Large Hadron Collider and the Compact Muon Solenoid experiment are given. Because no data are available yet, all data are simulated, as well as the detector response to the generated events. The production of the Z' boson is the subject of the fourth chapter as well as its decay into a top quark pair. Reconstruction of the $t\bar{t}$ invariant mass distribution in which resonances could appear is considered in the fifth chapter as well as the tools necessary to perform this reconstruction. In the last chapter, the significance of the signal is calculated with two different methods. Model-independent lower limits will be given on the $\sigma \times BR$ for the discovery of $t\bar{t}$ resonances. Thus it is possible to interpret the result within any model which predict a resonance particle. In the last chapter, the results are discussed en compared with other studies.

Dankwoord

Veel mensen hebben me geholpen en gesteund, mij de vele virtuele, letterlijke of figuurlijke schouderklopjes gegeven die soms nodig waren, bedankt! Dank aan mijn promotor Prof. S. Tavernier. Verder wil ik Jorgen laten weten dat het zonder zijn hulp allemaal niet mogelijk was geweest, dus ook naar hem werp ik een lieve blik! Steven, enorm bedankt voor alle hulp, steun en uitleg als ik "de computerwereld" weer eens niet de baas kon. Dankzij de motivatie, ervaring en het inzicht van Jan was het voor mij minder moeilijk om op te boksen tegen dingen die als vanzelfsprekend werden gezien, maar het voor mij niet waren of zijn. Er zijn nog veel mensen op het IIHE die ik mijn dank verschuldigd ben, al was het maar voor de warme sfeer waarmee ik opgenomen ben. In het bijzonder wil ik ook mijn bureaucollega Daan bedanken voor de fijne uren samen, ondanks de soms wat ontoegankelijke muziek ;-).

Irina en Tanika, ik weet dat het niet altijd even gemakkelijk was als ik weer eens helemaal "op" thuiskwam, maar ik ben blij dat jullie me bleven steunen als dat nodig was! Ook Johan en Annarella wil ik bedanken voor de vele mails en lange telefoongesprekken als ik iets kwijt moest! Damien, ik hoop dat ik je ook zo zal kunnen helpen als jij mij hebt kunnen helpen, ondanks het feit dat je soms het gevoel had dat je machteloos was!

Chapter 1

The Standard Model

The Standard Model is a quantum field theory that provides a description of the elementary constituents of matter and their interactions. This framework in which the elementary particles, the half-integer spin fermions and the integer spin gauge bosons, are summarized is currently the best formalism of our knowledge of particle physics. All experimental data in particle physics are in agreement with the Standard Model. The only ingredient of the Standard Model that has escaped detection so far is the elusive Higgs boson. Although the Standard Model has had great success in explaining experimental results, it has never been accepted as a complete theory of fundamental physics. The search for the Standard Model Higgs boson is not the only challenge left for the years to come. With the Large Hadron Collider some theories beyond the Standard Model become accessible to experiment. In this chapter the Standard Model with its virtues and its open questions is described.

1.1   The building blocks of the Standard Model

The Standard Model combines the theory of the electroweak interaction and the theory of quantumchromodynamics or the strong interaction. Both theories model the forces between fermions by coupling them to gauge bosons which mediate the forces.

The fermions can be arranged in three generations, the first one consisting of the electron, the up and down quark, and the electron neutrino. All ordinary matter is made from the first generation particles. The charged higher generation particles decay into the first generation ones and can only be produced for a very short time in high-energy experiments. The particles are arranged in generations because the four fermions in each generation behave almost identical as their counterparts in the other generations, the only difference being their masses. Fermions are further divided into quarks, which come in three colors, and leptons. Unlike quarks, leptons do not possess "color" and their interactions are only weak or electromagnetic, and fall off in strength with distance. The strong or "color" force between quarks becomes stronger with distance, so that quarks are always found in colorless combinations, which are the hadrons. This phenomenon is called quark confinement. The fermions are given in Table 1.1.

The bosons in the Standard Model are the photon γ, the W^+, W^- and Z^0 bosons, eight

gluons g and the Higgs boson. Gravitons, the bosons believed to mediate the gravitational interaction, are not accounted for in the Standard Model as it does not include this gravitational force. Table 1.2 shows the gauge bosons and the force they mediate.

Fermions	Generation			Q	I_3 (left-handed)	Y
	1	2	3			
Leptons	ν_e	ν_μ	ν_τ	0	1/2	-1
	e^-	μ^-	τ^-	-1	-1/2	-1
Quarks	u^i	c^i	t^i	2/3	1/2	1/3
	d^i	s^i	b^i	-1/3	-1/2	1/3

Table 1.1: *The three families of left-handed fermions in the Standard Model with some of their quantum numbers like the electric charge Q, the third component of weak isospin I_3 and the hypercharge Y related by $Q=I_3+Y/2$. Each of them has a corresponding anti-fermion particle and the index i refers to the three possible color charges of the quarks.*

Gauge bosons	Interaction	Spin	Mass (GeV/c^2)
γ	Electromagnetic	1	0
W^+ and W^-	Charged current Weak	1	$\simeq 80$
Z^0	Neutral current Weak	1	$\simeq 91$
g	Strong	1	0

Table 1.2: *The gauge bosons of the Standard Model with their spin properties and an indication of their mass value.*

The particles in Table 1.1 and 1.2 are the basic constituents of the Standard Model. In 1927, Dirac proposed that the electron has an anti-particle, the positron. The Dirac equation

$$i\hbar\gamma^\mu\partial_\mu\Psi = mc\Psi \tag{1.1}$$

was supposed to describe free electrons with energy given by the relativistic formula

$$E^2 = \mathbf{p}^2c^2 = m^2c^4$$

In equation 1.1 Ψ is the electron field and the γ^μ are matrices that can be represented as a function of the Pauli matrices. These matrices are defined by the following two properties:

$$\{\gamma^\mu, \gamma^\nu\} = 2\eta_{\mu\nu} \tag{1.2}$$

$$(\gamma^\mu)^\dagger = \gamma^0\gamma^\mu\gamma^0 \tag{1.3}$$

The problem with the Dirac equation was that it admitted for every positive energy solution, a corresponding solution with negative energy. This problem was solved by reexpressing the

negative energy solutions as positive energy states of a different particle: the anti-electron, or positron. Later it turned out that for every kind of particle in the Standard Model there must exist a corresponding anti-particle having the same mass, but opposite electric charge and magnetic moment.

1.2   Structure and framework of the Standard Model

The mathematical framework in which the Standard Model is embedded is a quantum field theory [1]. This theory is based on a variational principle which is similar to Hamilton's principle of least action in classical mechanics. We define the action as $S = \int \mathcal{L} \, d^4x$. Where $\mathcal{L}$ is the Langrangian density and d^4x stands for the four-dimensional element $dx^0 d^3\mathbf{x}$. The Langrangian density depends on a set of generic fields and their derivatives. The equations of motion or the Euler-Lagrange equations are then obtained by demanding that for a variation of the fields, the action S has a stationary value $\delta S = 0$. These equations are Lorentz-invariant because $\mathcal{L}$ is a scalar. An example of a Lagrangian density is the Dirac Lagrangian

$$\mathcal{L} = c\overline{\Psi}(i\hbar\gamma^\mu\partial_\mu - mc)\Psi \tag{1.4}$$

An important feature of the theory is that all the symmetry properties and the consequent conservation laws are contained in the Lagrangian density.

The theoretical pillar of the Standard Model is local gauge invariance with respect to the gauge group $\mathrm{G}_{SM} \equiv \mathrm{SU(3)}_c \otimes \mathrm{SU(2)}_L \otimes \mathrm{U(1)}_Y$. This means that the Lagrangian describing the particle fields is invariant under a set of symmetry transformations defined by the group G_{SM}. As a consequence of this gauge invariance under local phase transformations one needs to introduce gauge fields. The Lie algebra provides us with these gauge fields, which are the $8 + 3 + 1$ generators of the symmetry group. In this stadium all the particles in the theory are massless due to the fact that the theory is also invariant under the group itself, a global symmetry. We shall describe the mechanism that breaks the global symmetry in the following subsection.

The different groups that form the Standard Model group are:

- $\mathrm{SU(3)}_c$: the symmetry group of the strong force with 8 massless gauge boson fields G^a_μ, gluon fields. The subindex c stands for the color charge. The coupling constant of the strong interaction is called g_s and is related to α_s by $\alpha_s = g_s^2/4\pi$ (a $\in \{1,...,8\}$) ;

- $\mathrm{SU(2)}_L$: the symmetry group of left handed (subindex L) chirality states with 3 massless boson fields and coupling constant g ;

- $\mathrm{U(1)}_Y$: the symmetry group with one neutral massless boson field and coupling constant g'. The subindex Y stands for the hypercharge.

Gauge invariance completely determines the spin-1 particle content of the Standard Model. The algebra of SU(3) describes the strong force mediated by the gluon fields. The electromagnetic and the weak force are combined to the electroweak force defined by the $\mathrm{SU(2)}_L \otimes \mathrm{U(1)}_Y$

---

[1] For an introduction to quantum field theory, reference [1] is recommended.

algebra with the boson fields W^i_μ and B_μ, mediating the interactions with the coupling constants g and g'. The B_μ field is the U(1)$_Y$ singlet and the fields $\{W^i_\mu | i = 1, 2, 3\}$ form a triplet with respect to SU(2)$_L$. These boson fields correspond, when arranged into appropriate linear combinations, to the photon γ and to the $W^\pm$ and Z^0 bosons:

$$A_\mu = \sin\theta_W W^3_\mu + \cos\theta_W B_\mu = \frac{1}{\sqrt{g^2 + g'^2}}\left(g'W^3_\mu + gB_\mu\right)$$

$$Z_\mu = \cos\theta_W W^3_\mu - \sin\theta_W B_\mu = \frac{1}{\sqrt{g^2 + g'^2}}\left(gW^3_\mu - g'B_\mu\right) \tag{1.5}$$

The $W^\pm$ bosons are linear combinations of the remaining two triplet fields and couple only with left-handed chirality states:

$$W^\pm_\mu = \mp\frac{1}{\sqrt{2}}(W^1_\mu \pm iW^2_\mu) \tag{1.6}$$

The parameter θ_W is the Weinberg mixing angle which is related to the coupling constants in the following way:

$$g = -e/\sin\theta_W \qquad\qquad g' = -e/\cos\theta_W. \tag{1.7}$$

The spin-$\frac{1}{2}$ content of the Standard Model consists in three generations of quarks and leptons, whose transformation properties under G$_{SM}$ are summarized below:

$$q_{\alpha L} = \begin{pmatrix} u_{\alpha L} \\ d_{\alpha L} \end{pmatrix} \sim (3, 2, 1/6)$$

$$l_{\alpha L} = \begin{pmatrix} \nu_{\alpha L} \\ d_{\alpha L} \end{pmatrix} \sim (1, 2, -1/2)$$

$$u_{\alpha R} \sim (3, 1, 2/3), d_{\alpha R} \sim (3, 1, -1/3), e_{\alpha R} \sim (1, 1, -1), \tag{1.10}$$

In 1.10, α=1,2,3 is a generation index. We have used left- and right-handed chiral projections, defined by $P_{L,R} = (1 \pm \gamma^5)/2$, where γ^5 is defined as $i\gamma^0\gamma^1\gamma^2\gamma^3$. One should read these transformation properties as follows: the first number between the braces denotes the color charge. The second number denotes if the lepton is a singlet or a doublet under SU(2). The last number denotes the U(1)$_Y$ hypercharge. Notice the absence of right-handed neutrinos $\nu_{\alpha R}$. This is because the right-handed neutrino's are invariant under U(1), so they have a zero electric charge. They are also invariant under SU(2), as they are singlets under SU(2), and they have no color charge and therefore invariant under SU(3). Also it is assumed that there is no direct coupling between lepton families, or between quark and lepton families and that the neutrinos do not interact with photons. Given the quantum number assignments of equation 1.10, gauge invariance completely determines the interactions between fermions and gauge bosons described by the following Lagrangian density:

$$\begin{aligned} \mathcal{L}_{gauge} \quad = \quad & -\tfrac{1}{4}\, G^{a\ \mu\nu} G^a_{\ \mu\nu} - \tfrac{1}{4}\, W^{i\ \mu\nu} W^i_{\ \mu\nu} - \tfrac{1}{4}\, B^{\ \mu\nu} B_{\ \mu\nu} \\ & -i\, \bar{l}_{\alpha L}\gamma^\mu\, \mathcal{D}_\mu l_{\alpha L} - i\, \bar{e}_{\alpha R}\gamma^\mu\, \mathcal{D}_\mu e_{\alpha R} \\ & -i\, \bar{q}_{\alpha L\ i}\, \gamma^\mu\, (\mathcal{D}_\mu)^i_j\, q^j_{\ \alpha L} - i\, \bar{u}_{\alpha R\ i}\, \gamma^\mu\, (\mathcal{D}_\mu)^i_j\, u^j_{\ \alpha R} - i\, \bar{d}_{\alpha R\ i}\, \gamma^\mu\, (\mathcal{D}_\mu)^i_j\, d^j_{\ \alpha R} \end{aligned}$$

where

$$
\begin{aligned}
G^a{}_{\mu\nu} &= \partial_\mu G^a_\nu - \partial_\nu G^a_\mu - g_s f^{abc} G^b_\mu G^c_\nu, \\
W^i{}_{\mu\nu} &= \partial_\mu W^i{}_\nu - \partial_\nu W^i{}_\mu - g\epsilon^{ijk} W^j{}_\mu W^k{}_\nu, \\
B_{\mu\nu} &= \partial_\mu B_\nu - \partial_\nu B_\mu, \\
\mathcal{D}_\mu l_{\alpha L} &= (\partial_\mu + i\tfrac{g}{4}\vec{\sigma}\cdot\vec{W}_\mu - i\tfrac{g'}{2}B_\mu)l_{\alpha L}, \\
\mathcal{D}_\mu e_{\alpha R} &= (\partial_\mu - ig'B_\mu)e_{\alpha R}, \\
(\mathcal{D}_\mu)^i_j q^j_{\alpha L} &= (\delta^i_j\partial_\mu + \delta^i_j i\tfrac{g}{4}\vec{\sigma}\cdot\vec{W}_\mu + \delta^i_j i\tfrac{g'}{6}B_\mu - i\tfrac{g_s}{2}(\lambda^a)^i_j G^a_\mu)q^j_{\alpha L}, \\
(\mathcal{D}_\mu)^i_j u^j_{\alpha R} &= (\delta^i_j\partial_\mu + \delta^i_j i\tfrac{2}{3}g'B_\mu - i\tfrac{g_s}{2}(\lambda^a)^i_j G^a_\mu)u^j_{\alpha R}, \\
(\mathcal{D}_\mu)^i_j d^j_{\alpha R} &= (\delta^i_j\partial_\mu - \delta^i_j i\tfrac{1}{3}g'B_\mu - i\tfrac{g_s}{2}(\lambda^a)^i_j G^a_\mu)d^j_{\alpha R},
\end{aligned}
$$

and the symbols λ^a and $\frac{\sigma^i}{2}$, appearing in the covariant derivative D_μ, stand for the hermitean generators of the different G_{SM} factors in the representation defined by 1.10. The values for the hypercharge Y are already implemented in the covariant derivative. The f^{abc} stand for the $SU(3)$ group structure constants, the ϵ_{ijk} are the SU(2)$_L$ group structure constants denoted by the totally anti-symmetric Levi-Civita tensor in 3 real dimensions, the σ^i are the three Pauli matrices and the $(\lambda^a)^i_j$ are the components of the 8 linear independent Gell-Mann matrices with $a,b,c = \{1,...,8\}$ and $i,j,k = \{1,2,3\}$. The Dirac spinors of the particle fields ψ_i are represented by l, e, q, u and d.

1.3 Electroweak symmetry breaking

As mentioned in the previous section all particles described by the Lagrangian $\mathcal{L}_{gauge}$ remain massless. This is due to the fact that the theory remains invariant under the group G_{SM} considered as a global symmetry. However it is possible to give the particles their observed masses. Therefore it is necessary to break the internal symmetry in such a way that the theory remains gauge invariant. To avoid the introduction of massless spin-zero Goldstone bosons, we break the symmetry locally. The Goldstone bosons are in this way absent and the remaining degrees of freedom are "eaten" by the massive vector particles associated with the broken local symmetries. This fundamental observation was first made, in the relativistic context, by R.Brout, F.Englert [2] and P.W.Higgs [3].

In order to break the gauge invariance locally, gauge invariant terms must be added in $\mathcal{L}_{gauge}$. We are able to write down the most general form consistent with SU(2)$_L$⊗U(1)$_Y$ gauge invariance:

$$
\begin{cases}
\mathcal{L}_{Higgs} &= (\mathcal{D}_\mu\Phi)^\dagger(\mathcal{D}^\mu\Phi) - V(\Phi) \\
V(\Phi) &= \mu^2\Phi^\dagger\Phi + \lambda(\Phi^\dagger\Phi)^2
\end{cases}
\tag{1.11}
$$

with

$$
\mathcal{D}_\mu\Phi = (\partial_\mu + i\,\frac{g}{4}\,\vec{\sigma}\cdot\vec{W}_\mu + i\,\frac{g'}{2}\,B_\mu)\Phi.
\tag{1.12}
$$

where λ and μ^2 are real constants.

The so-called Higgs field or scalar complex spin-zero SU(2)-doublet Φ is defined as:

$$\Phi = \begin{pmatrix} \phi^+ \\ \phi^o \end{pmatrix} \longrightarrow \begin{cases} \phi^+ = \frac{\phi_1 + i\phi_2}{\sqrt{2}} \\ \\ \phi^o = \frac{\phi_3 + i\phi_4}{\sqrt{2}} \end{cases} \tag{1.13}$$

where the ϕ_i are the real fields. The Higgs field has the following transformation properties:

$$\Phi = \begin{pmatrix} \phi^+ \\ \phi^o \end{pmatrix} \sim (1, 2, +1/2) \tag{1.14}$$

It is clear that the Higgs field has no color charge, it is a doublet under SU(2) and has a U(1) hypercharge of 1/2.

For $\mu^2 < 0$, the potential V(Φ) is minimized when

$$\langle \Phi^\dagger \Phi \rangle = v^2 = \frac{|\mu^2|}{\lambda} > 0. \tag{1.15}$$

Thus, one particular vacuum state is given by,

$$\Phi = \begin{pmatrix} 0 \\ v \end{pmatrix} \tag{1.16}$$

The most general Φ field configuration can be written in the same notation as

$$\Phi = \frac{1}{\sqrt{2}} e^{i\alpha(x)\frac{\sigma}{2}} \begin{pmatrix} 0 \\ v + h(x) \end{pmatrix} \tag{1.17}$$

In this expression, $\alpha(x)$ parametrizes the SU(2) gauge transformation. The field $h(x)$ is a gauge invariant fluctuation away from the vacuum state; this is the physical Higgs field. The mass of this field is given by $m_H^2 = 2\lambda\, v$. Notice that $h(x)$ is the only gauge invariant degree of freedom in Φ, and so the symmetry breaking sector gives rise to only one new particle, the scalar Higgs boson.

In this way, we obtain masses for the gauge boson fields, while the photon remains massless:

$$m_W = \frac{1}{2} v \, |g| \qquad\qquad m_Z = \frac{1}{2} v \sqrt{g^2 + g'^2} \tag{1.18}$$

or at tree level

$$m_W = \cos\theta_W \, m_Z. \tag{1.19}$$

With this symmetry breaking mechanism, we have obtained masses for the gauge bosons and the Higgs boson itself, but the fermion fields remain massless. To generate mass for the fermions, one adds gauge invariant Yukawa couplings to the Lagrangian density:

$$\mathcal{L}_{Yukawa} = -G_{\alpha\beta}^l \bar{l}_{\alpha R} e_{\beta R} \Phi - G_{\alpha\beta}^d \bar{q}_{\alpha L} d_{\beta R} \Phi - G_{\alpha\beta}^u \bar{q}_{\alpha L} u_{\beta R} \tilde{\Phi} + h.c. \tag{1.20}$$

where the $G_{\alpha\beta}^{l,u,d}$ are the unknown Yukawa matrices (for example $m_e = G^e v$) which can be related to the Cabibbo-Kobayashi-Maskawa (CKM) matrix [2] and $\tilde{\Phi}$ is defined as $i\sigma^2\Phi^\dagger$.

As a result, the Lagrangian density describing the Standard Model is:

$$\mathcal{L} = \mathcal{L}_{gauge} + \mathcal{L}_{Higgs} + \mathcal{L}_{Yukawa} \tag{1.21}$$

1.4   Flavor physics

Flavor is a quantum number of elementary particles related to their weak interactions. Examples of flavor quantum numbers are the electric charge and the hypercharge. In the electroweak theory flavor symmetry is gauged, and flavor changing processes exist. In quantum chromodynamics (QCD), on the other hand, flavor is a global symmetry. Flavor symmetry is defined as follows: if there are two or more particles which have identical interactions, then they may be interchanged without affecting the physics. Any (complex) linear combination of these two will give the same physics, as long as they are orthogonal to each other. An example of flavor symmetry is:

$$M \begin{pmatrix} u \\ d \end{pmatrix},$$

where u en d are the two fields, and M is a SU(2) matrix.

Quarks have, like leptons, different quantum numbers. An example is the baryon number. All quarks carry a baryon number 1/3. The quantum numbers of the quarks can be combined to the hypercharge and the electric charge quantum numbers. A quark of a given flavor is an eigenstate of the weak interaction part of the Lagrangian: it will interact in a definite way with the weak gauge bosons. On the other hand, a fermion of a fixed mass (i.e. an eigenstate of the kinetic and strong interaction part of the Lagrangian) is a superposition of various flavors. As a result, the flavour content of a quantum state may change as it propagates freely. The transformation from flavor to mass basis for quarks is given by the CKM matrix. This matrix defines the strength of the flavor changes under weak interactions of quarks. In the Standard Model, all the tree-level flavor-changing-neutral current (FCNC) couplings, i.e. those of the photon, of the Z^0 and of the physical Higgs boson, are flavor diagonal. FCNC processes are induced only by loop effects, controlled by the CKM matrix and sufficiently suppressed to guarantee agreement with experimental data on flavour physics. It is interesting to know that the CKM matrix allows for CP violation if there are at least three generations. As flavor quantum numbers are additive, anti-particles have flavor equal in magnitude to the particle but opposite in sign.

In QCD, flavor symmetry is closely related to chiral symmetry. QCD contains six flavors of quarks. However, their masses differ. As a result they are not strictly interchangeable with each other. The two quarks of the first generation, the up and down quark, are close to having equal masses, and the theory of these two quarks possesses an approximate $SU(2)$ symmetry. Under some circumstances one can take N_f flavors to have the same masses and obtain an effective $SU(N_f)$ flavor symmetry. If the masses of the quarks can be neglected entirely,

---

[2]In the next section we will return to the meaning of the CKM matrix.

each flavor of quark possesses a chiral symmetry. One can then make flavor transformations independently on the left- and right-handed parts of each quark field. The flavor group is then a chiral group $SU_L(N_f) \times SU_R(N_f)$. If all quarks have equal masses, then this chiral symmetry is broken to the vector symmetry of the diagonal flavor group which applies the same transformation to both helicities of the quark. The symmetry is broken explicitly. The chiral symmetry can be spontanously broken even if the quarks are massless, if for some reason the vacuum of the theory contains a chiral condensate. This gives rise to an effective mass for the quarks.

1.5   Shortcomings of the Standard Model

The Standard Model description of the spontaneous electroweak symmetry breaking has been tested to an impressive level of precision at LEP, at the Tevatron and in other experiments at lower energies. Many observable quantities that are sensitive to the Standard Model radiative corrections have been measured with very high accuracy. Figure 1.1 [4] shows that the measured values are in excellent agreement with the Standard Model predictions. In this figure, the pull is also shown which is defined as the difference of the observed value from the value predicted by the Standard Model divided by it the uncertainty. No significant deviations are observed.

The only ingredient missing is the Standard Model Higgs boson. However, it is possible with the experimental results to perform a global fit as a function of the mass of the unobserved Higgs boson as we can see in figure 1.2 [4].

The most important message of electroweak precision tests concerns possible physics beyond the Standard Model: only very delicate deviations from the Standard Model predictions are allowed. This is a very strong constraint and has allowed to eliminate several extensions or modifications of the Standard Model proposed in the past.

One can ask why we should look for beyond the Standard Model physics anyway. Despite the remarkable achievements, there are indications to believe that the Standard Model, while it is simple and renormalizable, is not the ultimate theory of elementary particles. For instance, 19 arbitrary parameters are embedded in the theory, which may seem to many for a fundamental theory. And why should there be three different factors in the Standard Model gauge group, with the associated coupling constants taking the values they do? Why should fermions transform according to such an odd choice of chiral representations of $SU(2)_L \otimes U(1)_Y$, so that parity is violated in weak interactions? While the theory can be constructed to accommodate the breaking of electroweak symmetry, it provides no explanation for it. Furthermore there is no explanation for the existence of three fermion generations with the same gauge boson quantum numbers, nor for the complicated observed pattern of masses, mixing angles and phases. Moreover, it is quite obvious that the Standard Model must be extended, as the theory does not include a quantum theory of gravitational interactions! In addition are some of the Standard Model couplings not asymptotically free, making it inconsistent as a formal quantum field theory.

The different shortcomings of the Standard Model lead to a search for extended or entirely new models. The search is driven by some general ideas of physics beyond the Standard Model [5]. There is no "best way" to build Standard Model extensions, but the short-
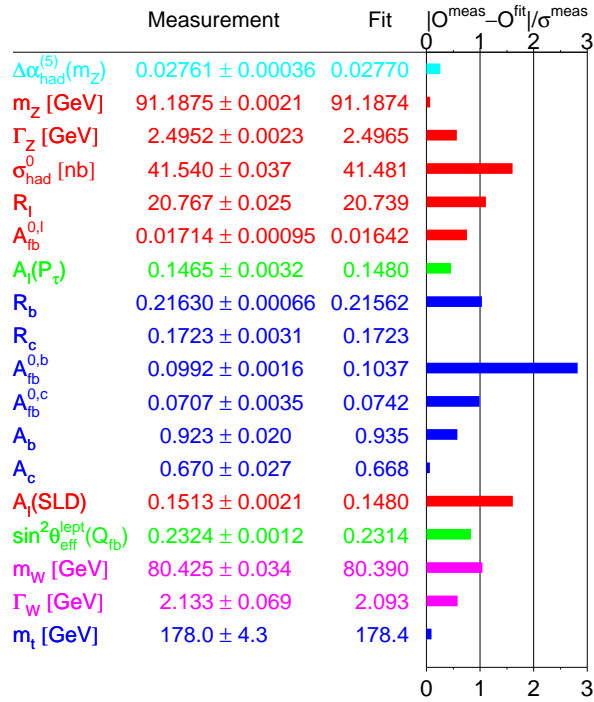
Figure 1.1: *Global Standard Model fit of all relevant measured electroweak observables to their predictions using radiative corrections up to second order (QED to third order). The pull is defined as the difference between the observed value and the predicted value divided by the uncertainty.*

comings imply that the Standard Model should be seen as an effective field theory, valid up to some physical energy cut-off scale Λ. The basic rule is to write down the most general local Lagrangian compatible with the Standard Model symmetries, scaling all couplings by appropriate powers of Λ. The dimensionless coefficients are usually interpreted as parameters. These parameters are either fitted to experimental data or theoretically determined from the fundamental theory replacing the Standard Model at the scale Λ. A question that naturally emerges is where this cut-off scale Λ is at which the Standard Model must be replaced by a more fundamental theory. Two plausible answers can be given:

1. The first answer is inspired by the Planck scale and is suggested by the measured strength of all the known fundamental interactions (including the gravitational). Thus, Λ is not much below $M_P \equiv \frac{1}{\sqrt{8\pi G_N}} \simeq 2.4 \times 10^{18}$ GeV, where G_N is the gravitational constant.

2. The other answer suggests that Λ is not much above the Fermi scale $M_F \equiv \frac{1}{\sqrt{G_F}} \simeq 250$
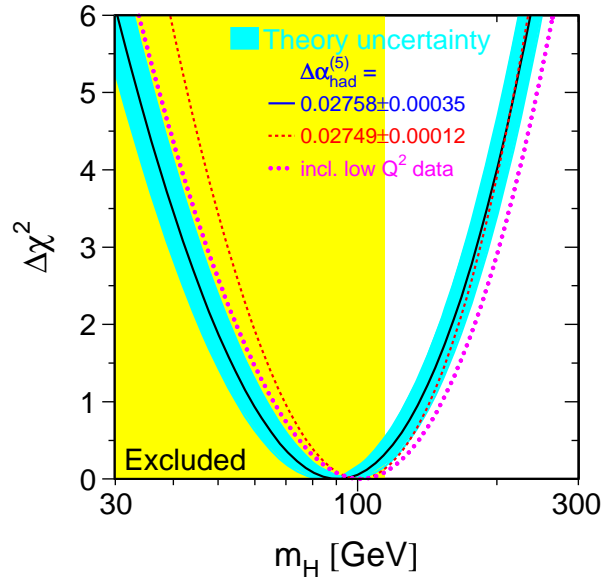
Figure 1.2: $\Delta\chi^2 \equiv \chi^2 - \chi^2_{min}$ versus m_H curve. The line is the result of the fit using all electroweak data; the band represents an estimate of the theoretical error due to missing higher order corrections. The vertical band shows the 95% CL exclusion limit on m_H from the direct search.

GeV, as electroweak symmetry breaking may imply new physics.

As the second answer is within the reach of the high energy physics experiments to come, it is clear that this answer will be explored. The answer inspired on the Fermi scale gives rise to two different paths to follow:

- Following the first path leads to embedding the Standard Model in a model with broken supersymmetry [7]. The supersymmetry-breaking mass splittings between the Standard Model particles and their superpartners are of the order of the electroweak symmetry.

- Following the second path leads to the replacement of the elementary Standard Model Higgs boson by some fermion condensate. This condensate is then induced by a new strong interaction near the Fermi scale.

In the next chapter, the so-called Technicolor models inspired by following the second path will be described.

Chapter 2

Technicolor models

In the previous chapter some shortcomings of the Standard Model are mentioned. More general problems are discussed in this chapter. Theoretical models have been suggested which provide solutions to some of these problems, for instance based on the mechanism of electroweak symmetry breaking.

2.1 Naturalness, triviality and fine-tuning

To understand better the motivations for new physics near the electroweak scale, the naturalness problem is described [8]. Such problem arises whenever there is insisted, on the presence of an elementary Higgs field in the Langrangian to describe the breaking of the electroweak symmetry, and we want to extrapolate the model to a scale Λ much larger than the Fermi scale. The tree level potential of the Standard Model is characterized by a mass parameter μ^2 and by a dimensionless quartic coupling λ. As summarized in the previous chapter, one combination of these two parameters is fixed by fitting the vacuum expectation value (VEV) v of the Standard Model Higgs field to the measured value of the Fermi constant, defining the scale of electroweak symmetry breaking. The squared mass m_H^2 of the physical Higgs particle, proportional to μ^2, or equivalently, to λv^2 is instead a free parameter of the Standard Model. While the lower bound on the Higgs mass comes from experiment, arguments based on unitarity and triviality suggest that self-consistency of the Standard Model is broken unless $m_H < \mathcal{O}(1 \text{ TeV})$. This is hard to reconcile, from the effective field theory point of view, with the fact that, already at one-loop, there are quadratically divergent contributions to the Higgs boson mass. Thus, there is no natural reason why m_H and v should be much less than the energy scale at which the essential physics of the model changes. How can the Higgs boson mass be of the order of the electroweak scale and not of the order of the physical ultraviolet cut-off of the theory? One can say that Higgs models are unnatural.

The problem outlined above is generic for theories containing elementary spin-zero fields [5]. The only known candidate to solve this problem is supersymmetry. Alternatively, we need to dispose of elementary spin-zero fields [1].

---

[1]There exists other naturalness problems of the Standard Model [9] [10].

The Standard Model suffers from another problem concerning the Higgs sector, namely fine-tuning. Corrections to the Higgs mass, due to loop diagrams, diverge quadratically with energy and require repeated fine-tuning with the inclusion of more and more loops in the calculation.

There is also other theoretical discomfort with the Standard Model concerning the elementary Higgs boson picture of electroweak and flavor symmetry breaking - the cornerstone of the Standard Model. For example, elementary Higgs models provide no dynamical explanation for electroweak symmetry breaking. Another example of the discomfort is the fact that elementary Higgs models provide no insight to flavor physics. Every aspect of flavor is completely mysterious, from the primordial symmetry defining the number of quark and lepton generations to the bewildering patterns of flavor breaking. The presence of Higgs bosons has no connection to the existence of multiple and identical fermion generations. The flavor-symmetry breaking Yukawa couplings of Higgs bosons to fermions are arbitrary free parameters, put in by hand.

A further problem of elementary Higgs boson models is that they are "trivial" [11]. To a good approximation, the self-coupling $\lambda(M)$ of the minimal one-doublet Higgs boson at the energy scale M is given by

$$\lambda(M) \cong \frac{\lambda(\Lambda)}{1 + (24/16\pi^2)\lambda(\Lambda)log(\Lambda/M)} \tag{2.1}$$

This vanishes for all M as the cut-off Λ is taken to infinity, hence the description "trivial". Triviality implies that elementary Higgs Langrangians must be considered to describe effective theories. This effective theories are meaningful only below a cut-off scale Λ_∞ at which new physics sets in. The larger the Higgs couplings are, the lower the scale Λ_∞. This relationship provides the triviality bounds on Higgs masses:

$$m_H(\Lambda_\infty \cong \sqrt{2\lambda(m_H)}v) = \frac{2\pi v}{\sqrt{3log\Lambda_\infty/m_H}} \tag{2.2}$$

The effective theory has some range of validity if the Higgs mass is somewhat less than the cut-off scale.

2.2   Technicolor

Since, the naturalness and other open problems of the Standard Model are due to its Higgs sector, the most convenient strategy in the search for a solution is to get rid of elementary spin-zero fields in the Langrangian, replacing the Higgs doublet with some dynamical fermion condensate, induced by some new strong interaction. To break the electroweak symmetry, there is no need for elementary Higgs bosons [2]. It is possible to give mass to the gauge bosons without introducing elementary Higgs bosons. This mechanism is known as the dynamical Higgs mechanism. Suppose the world was described by the standard SU(3)⊗SU(2)⊗U(1) Langrangian with gauge bosons, three generations of quarks and leptons, like $\mathcal{L}_{gauge}$ in chapter 1. If the small electroweak couplings of the quarks are ignored,

---

[2]For this section I mainly used reference [12]

their interactions respect a large global chiral symmetry $SU(6)_L \otimes SU(6)_R$. In models of dynamical electroweak symmetry breaking, like the dynamical Higgs model, chiral symmetry breaking in an asymptotically-free gauge theory is assumed to be responsible for breaking the electroweak symmetry. The simplest models of this sort rely on QCD-like "Technicolor" interactions. Consider an $SU(N)_{TC}$ gauge group, with a coupling constant g_{TC}. The Standard Model fermions described in 1.10 are singlets under $SU(N)_{TC}$. Suppose that there exists also a generation of massless technifermions, with the following transformation properties in the fundamental representation of the gauge group

$$SU(N)_{TC} \otimes SU(3)_c \otimes SU(2)_L \otimes U(1)_Y$$

$$T_L = \begin{pmatrix} U_L \\ D_L \end{pmatrix} \sim (N, 1, 2, 0)$$

$$U_R \sim (N, 1, 1, 1/2), D_R \sim (N, 1, 1, -1/2) \tag{2.4}$$

The fermion kinetic terms for this theory are

$$\mathcal{L} = i\overline{U}_L \gamma^\mu \, \mathcal{D}_\mu U_L + i\overline{U}_R \gamma^\mu \, \mathcal{D}_\mu U_R + i\overline{D}_L \gamma^\mu \, \mathcal{D}_\mu D_L + i\overline{D}_R \gamma^\mu \, \mathcal{D}_\mu D_R \tag{2.5}$$

and, like QCD for vanishing masses of the up and down quark, they have a chiral $SU(2)_L \otimes SU(2)_R$ symmetry.

As in QCD, exchange of techni-gluons in the spin-zero, isospin-zero channel is attractive causing the formation of a condensate

$$\left\langle \overline{U}_L U_R \right\rangle = \left\langle \overline{D}_L D_R \right\rangle \neq 0, \tag{2.6}$$

which dynamically breaks $SU(2)_L \otimes SU(2)_R$ to the diagonal $SU(2)_V$. These broken chiral symmetries imply the existence of three massless Goldstone bosons, like the pions accompany the chiral symmetry breaking in QCD. These pions decay, and the pion decay constant f_π, which couples the pions to the W boson is measured to a value of 93 MeV.

Now consider gauging $SU(2)_L \otimes U(1)_Y$ with the left-handed fermions transforming as weak doublets and the right-handed ones as weak singlets. To avoid gauge anomalies, in this one-doublet Technicolor model, we will take the left-handed techni-fermions to have hypercharge zero and the right-handed up and down techni-fermions to have hypercharge $\pm 1/2$. The spontaneous breaking of the chiral symmetry breaks the weak interactions down to electromagnetism. The would-be Goldstone bosons become the longitudinal components of the W and Z gauge bosons which acquire a mass

$$M_W = \frac{g F_{TC}}{2}, M_Z = \frac{\sqrt{g^2 + g'^2} F_{TC}}{2} \tag{2.7}$$

Here F_{TC} is the analog of f_π in QCD. In order to obtain the experimentally observed masses, we must have that $F_{TC} \approx 246$ GeV and hence this model is essentially QCD scaled up by a factor of [13]

$$\frac{F_{TC}}{f_\pi} \approx 2500. \tag{2.8}$$

Such a dynamical description of the spontaneous breaking of the gauge symmetry is very elegant, but the model is too simple to be realistic. An important feature of the Standard Model is missing: there is no breaking of the flavor symmetry, and fermion masses and mixing are not reproduced. From this point of view, the Standard Model description with an elementary Higgs boson has an advantage.

2.3   Extended Technicolor and 'walking' Technicolor

We have seen in the previous section that Technicolor interactions are able to give masses to the W and Z bosons, but not to the fermions. Additional interactions must be introduced in order to produce the masses for the leptons and quarks of the Standard Model. These interactions are for example "Extended Technicolor" (ETC) gauge interactions. In ETC, SU(N_{TC}) Technicolor, SU(3) color and flavor symmetries are embedded into a larger gauge group. This ETC group, G_{ETC}, is spontaneously broken at a certain scale $\Lambda_{ETC} > \Lambda_{TC}$ down to SU(N_{TC})$\times$G$_{SM}$. In this way, technifermions are able to interact with the Standard Model fermions. The ETC gauge bosons mediate transitions among the techni-fermions themselves, leading to interactions which can explicitely break unwanted chiral symmetries. Mass terms are generated by interactions involving the exchange of the ETC gauge bosons and of techni-fermions. The typical size of these mass terms is [12]

$$m_q \approx \frac{g_{ETC}^2 \langle \overline{q}_L q_R \rangle_{\Lambda_{ETC}}}{\Lambda_{ETC}^2} \tag{2.9}$$

To reproduce the observed quark mixing, there must be ETC interactions coupling quarks of the same charge from different generations. But, this leads to phenomenological problems with flavor changing neutrals currents (FCNC). To avoid problems of this kind in a natural way, we should have $\Lambda_{ETC} \geq 500$ TeV, which is much larger than expected naively by scaling from QCD [14]. In ETC models, the existence of heavy fermions and the observed suppression of FCNC are incompatible. To avoid this kind of problems and to explain the observed masses of the heavy fermions, models with Technicolor gauge couplings which run very slowly, or "walk", were suggested [16]. In these models, there must be a non-conventional dynamical behaviour at high scales, which does not follow the QCD paradigma. However, this is still insufficient to explain the observed value of the top quark mass [12].

2.4   Topcolor and Topcolor-Assisted Technicolor

The top quark is much heavier than the other fermions and must therefore couple stronger to the symmetry-breaking sector. This suggests that the third generation may play a special role in the dynamics of electroweak symmetry breaking. It is thus natural to consider whether some or all of electroweak symmetry breaking is due to a dynamical condensate of top-quarks, generated by a new strong gauge force coupling preferentially to the third generation

at an energy scale, Λ_t. In 1991 C. Hill proposed the following model [17]: consider a gauge group SU(3)$_h \times$SU(3)$_l \times$ SU(2)$\times$U(1) which is spontaneously broken to SU(3)$_{QCD} \times$ U(1) by top quark condensation. SU(3)$_h$ couples to the third generation and has a coupling g_h and SU(3)$_l$ couples to the first and second generation and has a coupling g_l, and $g_h >> g_l$. This scheme produces degenerate top quarks and bottom quarks. Extra interactions must be introduced to split the top and bottom quark masses. In order to achieve a phenomenologically acceptable theory, the Topcolor coupling g_h must be extremely fine-tuned. As the degenerate top and bottom quarks caused a problem, one searched for a strong dynamics that causes the top quark to condense, $\langle t\bar{t} \rangle \neq 0$ while simultaneously suppressing the formation of a large bottom quark condensate, $\langle b\bar{b} \rangle \approx 0$. To makes this possible, additional strong U(1) interactions were introduced. Still, it was not possible to get the correct scale of the top quark mass with top quark condensation alone. Therefore, in 1994 [19], Topcondensation was combined with Technicolor in models of Topcolor-assisted Technicolor or TC2. TC2 postulates that the large top quark mass is due to combination of (i) a small fundamental component ϵm_t, generated by extended Technicolor interactions (or Higgs), plus (ii) a large dynamical condensate component $(1 - \epsilon)m_t$, generated by Topcolor dynamics at the scale 1TeV, which is coupled preferentially to the third generation. If $\epsilon = 0$, the model is based on a pure Topcondensation model. With $\epsilon \neq 0$ the requirement that the top quark condensate generates the electroweak symmetry breaking completely is relaxed. Electroweak interactions are still broken by Technicolor interactions at a scale of 1TeV, as Technicolor is the most natural mechanism for electroweak symmetry breaking. The masses of the light quarks and the leptons are generated by extended Technicolor. In combination with Technicolor, Topcolor is not unnatural.

In detail, TC2 depends on seperate color and weak hypercharge interactions for the third and the first two generations. For the Topcolor dynamics, consider the following gauge group structure: SU(3)$_h \times$SU(3)$_l \times$SU(2)$\times$U(1)$_h \times$U(1)$_l$, where the third generation of quarks and leptons transforms under the Topcolor gauge group $SU(3)_h \times U(1)_h$ while the first and the second generation transforms under a seperate group $SU(3)_l \times U(1)_l$. At a scale assumed to be $\approx$1 TeV, before Topcolor becomes confining, the gauge group must be dynamically broken to the diagonal subgroup of ordinary color and weak hypercharge SU(3)$_{QCD} \times$U(1). At this energy, the $SU(3)_h \times U(1)_h$ couplings are strong while the $SU(3)_l \times U(1)_l$ couplings are weak. A techni-condensate is responsable for this breaking, but a large residual global symmetry is left. This symmetry implies the existence of a degenerate, massive color octet of "topgluons" and a color singlet Z'.

2.5   The Z' boson and experimental limits

In TC2, the electroweak gauge group is SU(2)$\times$U(1)$_h \times$U(1)$_l$, where the U(1)$_h$ couples to the heavy third generation quarks and the U(1)$_l$ to the lighter first two generations, with the coupling constants g_h and g_l and $g_h >> g_l$. At a scale above the weak scale, the two hypercharge groups break to their diagonal subgroup, the U(1) we know from the Standard Model. This breaking gives rise to a massive Z' boson that is a linear combination of the original two hypercharge bosons. The Z' boson couples to fermions as [23]

$$-i\frac{e}{cos\theta}\left(\frac{sin\chi}{cos\chi}Y_l - \frac{cos\chi}{sin\chi}Y_h\right) \qquad (2.10)$$

where Y_h and Y_l are the fermion's hypercharges under the U(1)$_h$ and U(1)$_l$ group. The parameter χ is the mixing angle between the two original hypercharge sectors, with

$$cot\chi = \left(\frac{g_h}{g_l}\right)^2$$

From 2.10 it is clear that the Z' couples to left-handed and right-handed fermions at leading order. The overall coupling is of hypercharge.

In the past few years some experiments had the capabilities, high enough energies and the large data samples, to begin direct searches for the new phenomena predicted by models of new strong dynamics. No new particles have been found yet, but the experiments performed by LEP and Tevatron gave us experimental limits and constraints on Technicolor, extended Technicolor and walking Technicolor. In Technicolor, there will generally occur isovector and isosinglet vector mesons, $\rho_T^\pm$, ρ_T^0 and ω_T^0, the analogues of $\rho(770)$ and $\omega(782)$ in QCD [13]. These vector mesons have decays to weak gauge bosons and techni-pions and are therefore particularly interesting phenomenologically. Another example of visible resonance structures may be provided in processes like $p\overline{p}$ or $e^+e^- \to W^+W^-$ and make large contributions to techni-pion pair production. For instance L3 used 176,4 pb^{-1} of data collected at an average center of mass energy of 188,6 GeV to search for color singlet ρ_T [27]. The search took into account the four major techni-ρ decay modes: $\rho_T \to WW, W\pi_T, \pi_T\pi_T, \gamma\pi_T$ for the following range of techni-ρ and technipion masses:

$$150 GeV < M_{\rho_T} < 250 GeV \qquad\qquad 50 GeV < M_{\pi_T} < 150 GeV$$

In the WW decay channel, all decay modes of the W bosons were included. The result is that an upper limit of 0,47 pb was set at 95% C.L. on the possible increase of the $e^+e^- \to WW$ cross section due to contributions from Technicolor.

The Tevatron experiments give us limits on Topcolor and Topcolor-assisted Technicolor Models. The Z' boson present in some models of Topcolor-assisted Technicolor and resonances predicted by other models will preferentially couple to the top quark. Therefore, the CDF and D0 collaborations performed searches for narrow $t\overline{t}$ resonances in $p\overline{p}$ collisions at 1,96 TeV in Run II. D0 excluded at 95% C.L. the existence of the Z' boson with a mass $M_{Z'} < 680$ GeV and width $\Gamma_{Z'} = 0,012 M_{Z'}$. The search for a narrow width resonance in the l+jets final states has been performed using data corresponding to an integrated luminosity of around 370 pb^{-1}. Model-independent upper limits on $\sigma_X \times B(X \to t\overline{t})$ have been obtained for different hypothesized masses of a narrow-width heavy resonance decaying into $t\overline{t}$. These limits were obtained by analyzing the reconstructed $t\overline{t}$ invariant mass distribution and using a Bayesian method. The result is shown in Figure 2.1 [29]. The CDF collaboration performed the same search using data corresponding to an integrated luminosity of 680 pb^{-1}. They excluded at 95% C.L. the existence of a Z' boson with a mass $M_{Z'} < 725$ GeV and width $\Gamma_{Z'} = 0,012 M_{Z'}$.
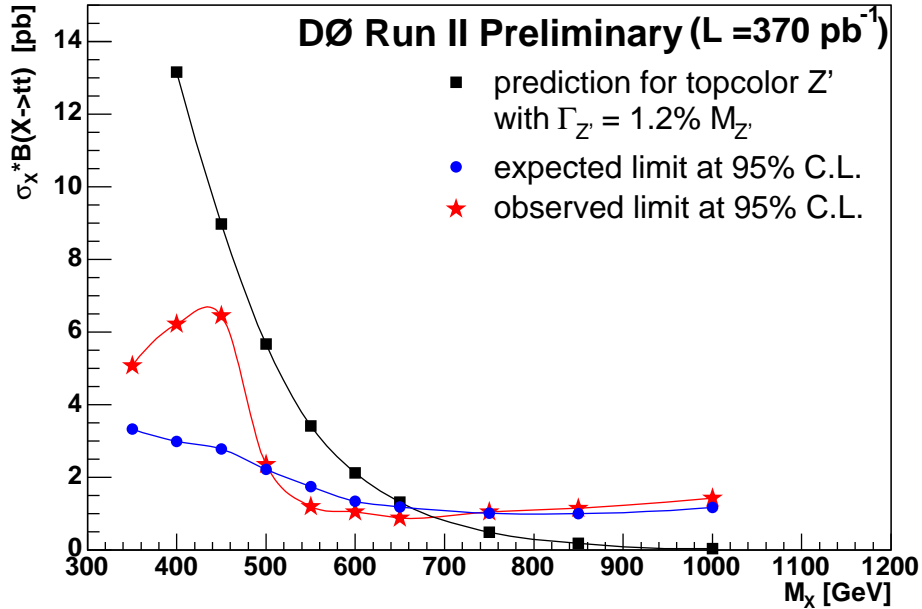
Figure 2.1: *Expected and observed 95% C.L.upper limits on $\sigma_X \times B(X \to t\bar{t})$ compared with the predicted Topcolor-assisted Technicolor cross section for a Z' boson with a width of $\Gamma_{Z'} = 0,012 M_{Z'}$ as a function of resonance mass M_X as obtained with the D0 experiment.*

2.6 Outlook

In this chapter the possibility that the origin of mass involves a new strong dynamics near the TeV scale was considered. Dynamical electroweak symmetry breaking can provide a natural explanation for the weak scale. It can also provide clues about the magnitudes and the origins of the fermions masses and mixings. Technicolor generates the weak scale in essentially the same way the strong scale is generated by QCD. But, Technicolor is an incomplete theory and extended Technicolor was introduced to generate the light fermion masses. However, this was not sufficient and models such as walking Technicolor were needed to accomodate heavier fermion masses.

The discovery of the heavy top quark led to alternate dynamical models for electroweak symmetry breaking, based on the idea of Topcolor. Topcolor by itself is a fine-tuned theory in which the top quark condenses. However, the top quark mass predicted by Topcolor models was found to be too big in comparison with the experimental value for its mass. In combination with Technicolor, there are models in which technidynamics can coexist and the top quark acquires a dynamical mass through Topcolor. These models, Topcolor-assisted Technicolor, predict a rich phenomenology that will be accesible to the Large Hadron Collider.

Strong dynamical models of electroweak symmetry breaking are untill these days entirely consistent with all known experimental limits. However, it is not certain these models are true. Dynamical electroweak symmetry breaking is an attractive idea, still looking for a

complete and satisfactory model. We should keep an eye on the possible models of dynamical electroweak symmetry breaking and analyze future experimental data without prejudice. The experimental study at LHC of possible deviations from the Standard Model predictions may shed light on possible strongly-interacting dynamics at work in the symmetry-breaking sector of the Standard Model.

There is of course a wide variety of possible models beyond the Standard Model, which were not discussed here, for instance models based on supersymmetry, or Technicolor models in combination with supersymmetry, or models in which extra dimensions occur.

All these models predict new particles and some of these particles are predicted within the reach of the LHC. Many of these particles couple preferentially to the third generation of quarks. Therefore I will concentrate on the observability of $t\bar{t}$ resonances at the Large Hadron Collider. For this, in the next chapters a method is described by means of the Z' boson predicted by Topcolor-Assisted Technicolor models.

Chapter 3

The Large Hadron Collider and the CMS experiment

The Standard Model provides the best description of the elementary particles and their interactions. Despite this remarkable achievement, the Standard Model leaves several questions unanswered. Therefore, scientists are looking for a new type of physics beyond the Standard Model. In order to look for this new type of physics, the Large Hadron Collider or LHC is now being built. In this chapter an overview of the experimental facility is provided. The basic features of the accelerator will be described. In the second part of this chapter a review of the CMS experiment will be given.

3.1   Proton collisions at the Large Hadron Collider

The Fermilab Tevatron proton-antiproton Collider is currently the world's highest energy hadron collider. The Tevatron Collider has a circumference of four miles. In 1995 both the experiments installed at Fermilab, CDF and D0 discovered the top quark. The Tevatron accelerator is capable of colliding a proton and an anti-proton at a combined energy of about 2 TeV. Despite the remarkable achievements of the Tevatron collider, the Higgs boson isn't found yet. To explore regions of higher energy, the LHC is under construction at CERN in Geneve.

   The LHC is being built in the 27 km circumference tunnel formerly used by the Large Electron-Positron collider (LEP), at CERN. This challenging accelerator will collide proton bunches at a center of mass energy $\sqrt{s}$ of about 14 TeV. At its planned starting date in 2007, the LHC will be the largest hadron collider in the world and the detectors will be able to measure with high precision and efficiency the properties of the particles that are produced in the pp collisions.

   To explore physics near the TeV scale, an accelerator needs more energy then for instance LEP. The synchrotron radiation of the electrons and the magnets in the LEP collider set an upper limit to its energy reach. There are two possibilities to avoid the problem of synchrotron radiation and still reach higher energies: one could increase the radius of the collider or one could increase the mass of the accelerated particles. This can be seen from the following formula for synchrotron energy loss:

$$-\Delta E = \frac{4\pi\alpha}{3R}\beta^3\gamma^4 \sim \frac{E^4}{Rm^4} \tag{3.1}$$

with $\beta = v/c$ and $\gamma = E/mc^2$, where R is the radius of the accelerator, E the energy of the particle and m its mass. It is clear that increasing the radius of the collider is less easy then increasing the mass of the particles. Therefore it was decided to use protons instead of electrons, as the mass of protons is about 2000 times larger. However, increasing the mass and using protons, poses complications as a large magnetic dipole field is needed to compensate the centrifugal force of the particles. This problem could be solved by using superconducting magnets. Another complication deals with the structure of protons. Protons are not elementary particles, but consists of quarks and gluons, generally called partons, which carry only a fraction of the momentum of the protons. Thus, the effective center of mass energy used for the production of new particles is much less than de center of mass energy of the LHC:

$$\sqrt{s_{eff}} = \sqrt{x_a x_b s},$$

where x_a and x_b are the fractions of the momentum of the protons carried by the partons. Thus, $\sqrt{s_{eff}}$ is strongly depended on the parton distribution functions which are the distributions of the momentum of the partons in the proton. Protons consist of three valence quarks which will carry the biggest fraction of the momentum. But, in the proton there are also "sea" quarks, due to gluon radiation of the valence quarks. The parton distribution functions depend on the momentum transfer Q^2 in the interaction. For high enough Q^2, the valence quarks and the "sea" quarks are distinguishable, which means that there will be a high contribution for low fractions of the initial proton momentum. For low Q^2, only the valence quarks will be distinguishable and there will be a bigger contribution for higher fractions of the proton momentum.

Most hadron colliders in the past produced $p\bar{p}$ collisions, but the LHC will produce pp collisions. This was decided because it could be difficult to produce sufficient amounts of antiprotons. For physics searches this poses not a problem as the distribution of gluons in protons and antiprotons is the same and as the most important contribution in the production of new particles is due to the gluons rather than to the quarks. The difficulty with pp collisions was that the collider would need a different design. In colliders, like LEP, a single beam pipe could be used with an elliptic transverse shape where the particles and antiparticles could circulate in opposite directions next to eachother. This is not possible for a same charge collider. The proton beams must circulate in opposite directions inside two separate beam pipes and two opposite magnetic field configurations are required. The design of the LHC dipole magnets realizes these requirements as can be seen in Figure 3.1.

A single cryostatic structure incorporates the two beam pipes together with their superconducting dipole magnets. To bend the 7 TeV protons around the ring, magnetic fields of 8,4 Tesla must be produced. The dipoles will operate at 1,9 K as this is the temperature where helium becomes a superfluid. At this temperature, the LHC magnets will be capable to carry currents of 15000 A. The particles will be kept in orbit by oppositely polarized quadrupoles which are able to focus and defocus the proton bunches. Sextupole and dipole correctors are used to correct the inaccuracies of the main dipoles. The LHC will be made of more than 5000 superconducting magnets.
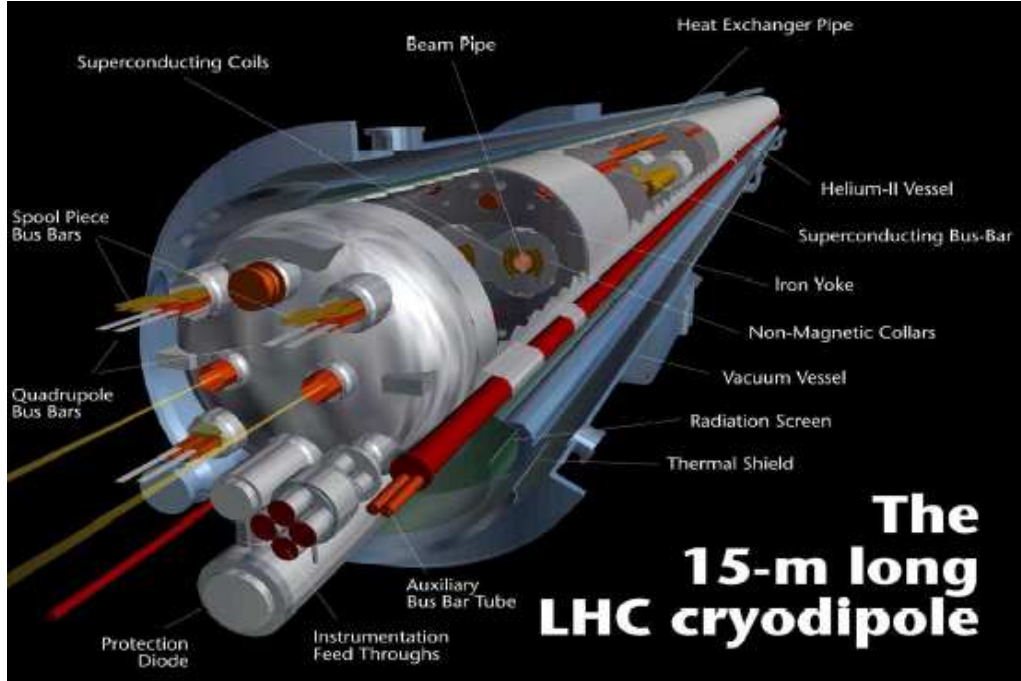
Figure 3.1: *The LHC dipole*

The performance of a collider is defined by the center of mass energy $\sqrt{s}$ and the luminosity $\mathcal{L}$. The center of mass energy $\sqrt{s}$ increases with the energy of the colliding particles, the luminosity $\mathcal{L}$ is proportional to the number of collisions per second. The number of interactions corresponding to a certain type of physics events with a cross section σ is related to the integrated luminosity through the following relation:

$$N = \sigma \int \mathcal{L}dt \tag{3.2}$$

As the cross section σ of parton-parton processes decreases proportional to $1/E^2$, it is clear that an increase of the energy of the collider requires an increase in its luminosity proportional to E^2 to keep the same statistical significance. In practice, for a hadron collider, there is also the complication of taking into account the structure functions or PDFs, which were mentioned earlier. Thus, the largest possible luminosity is required. The design luminosity of the LHC is 10^{34}cm^{-2}s^{-1} ("high luminosity" running). For the first three years, the LHC will run at the lower luminosity of 2.10^{33}cm^{-2}s^{-1} ("low luminosity" running). The luminosity of an accelerator is given by

$$\mathcal{L} = f\left(\frac{n_1 n_2}{4\pi\sigma_x\sigma_y}\right) \tag{3.3}$$

where f is the revolution frequency, n_1 and n_2 are the number of particles in the bunches and σ_x and σ_y are the widths which characterize the Gaussian transverse beamprofiles. An integrated luminosity of 10 fb^{-1} per year will be collected in the low luminosity period and 50 fb^{-1} per year in the high luminosity period.

400 MHz superconducting radiofrequency cavities with a voltage ranging from 8 to 16 MV/m will produce the boost of the protons. The nominal number of protons per bunch will be about 10^{11}: bunches will have a very small transverse spread, σ_x, $\sigma_y \approx 15\mu$m, while the longitudinal length is about 7,5 cm at the collision points. The average number of inelastic pp collisions per bunch crossing will be high (up to 20 events) because of the large number of protons per bunch. A complication is that the rate of events at LHC will be several order of magnitude larger than the maximum allowed for the data storage devices. The total inelastic cross-section is estimated to be 100 mb or an average of 10^9 interactions taking place per second in the high luminosity period. Thus, the interesting events that may occur will be superimposed on top of the 20 events, which is called pile-up. Minimizing pile-up is possible by operating at a high collision frequency, so that the luminosity is kept constant. The LHC bunch crossing rate will be 40 MHz, or a bunch crossing will occur every 25 ns. This high frequency imposes requirements on the response times of the detectors. A very high time resolution is needed to distinguish between events belonging to different bunch crossings. Furthermore, a strong online selection (triggering) is required to reduce the interaction rate by 7 orders of magnitude. To distinguish between particles very close in space, detector units must be finely segmented.

A summary of the most important design parameters of the LHC in the proton-proton mode is given in Table 3.1.

Design or technical parameter	Value	Units
Ring circumference	26.7	km
Design luminosity	10^{34}	$\text{cm}^{-2}\text{s}^{-1}$
Beam lifetime at design luminosity	≈ 28	h
Dipole magnetic field at 7 TeV	8.33	T
Magnet temperature	1.9	K
Radiofrequency	400.8	MHz
Acceleration time	20	minutes
Injection beam energy	450	GeV
Energy at collision	14	TeV
Number of bunches	2808	
Number of protons per bunch	10^{11}	
Beam spacing	25	ns
Bunch crossing frequency	40	MHz
Beam transverse dimensions	0.3×0.3	mm^2
Beam transverse dimensions at collison	16×16	μm^2
Bunch length	7.5	cm

Table 3.1: *The most important design or technical parameters of the LHC in the pp-mode.*

The existing CERN facilities have been upgraded to supply the LHC with pre-accelerated protons. To pre-accelerate the protons, they go through the already existing machines: first the protons go to a linear accelerator or linac, which brings them up to 50 MeV. Then, they go through a booster which brings them up to 1.4 GeV. The Proton Synchrotron or PS will

bring them up to 25 GeV and after that the protons enter the Super Proton Synchrotron or SPS from which they are injected in the LHC with an energy of 450 GeV. In the LHC the protons will be accelerated to their final energy of 7 TeV. To fill both LHC rings, 24 SPS cycles are required. The nominal number of bunches in one LHC ring will be 2808 out of 3546 available bunch places. This discrepancy is due to the rise and fall time of the kicker magnets. The filling procedure takes about seven minutes. After that, the beam lives in the LHC for about 22 hours. Only the first ten hours data will be taken because after that, due to the collisions, the luminosity will be decreased too much. In Figure 3.2 the chain of accelerators is shown.
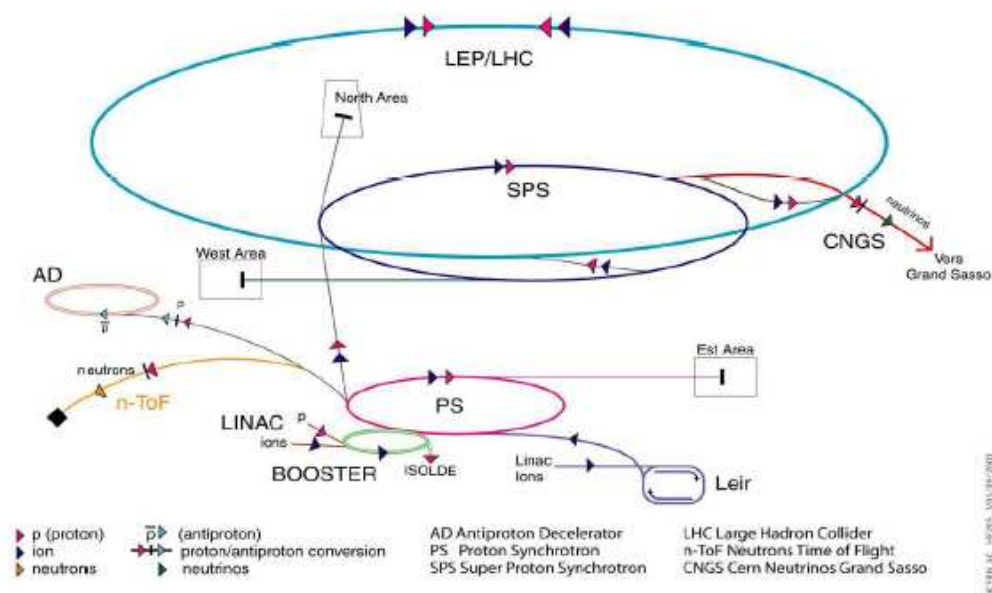
Figure 3.2: *The chain of accelerators at CERN.*

The proton bunches in the LHC will collide at four interaction regions, where four experiments are being built. These four particle detectors are ATLAS (A Toroidal LHC ApparatuS), CMS (Compact Muon Solenoid), LHCb and ALICE (A Large Ion Collider Experiment). The ATLAS and CMS experiments are based on general purpose detectors, whose research is aiming for the full spread of physics possible at LHC in the *pp*-mode, but whose research is in particular focused on the search for new particles. LHCb is specifically dedicated to b-physics and CP-violation. The fourth experiment is specialized in heavy ion physics and quark gluon plasma, which will be very usefull when the LHC accelerates ions instead of protons. Figure 3.3 shows the geographical location of the experiments in the LHC tunnel.

Main goals for the physics research at the LHC are:

- search for the Higgs boson predicted in the Standard Model and if the Higgs boson doesn't exist, study alternative models of electroweak symmetry breaking at the TeV scale.
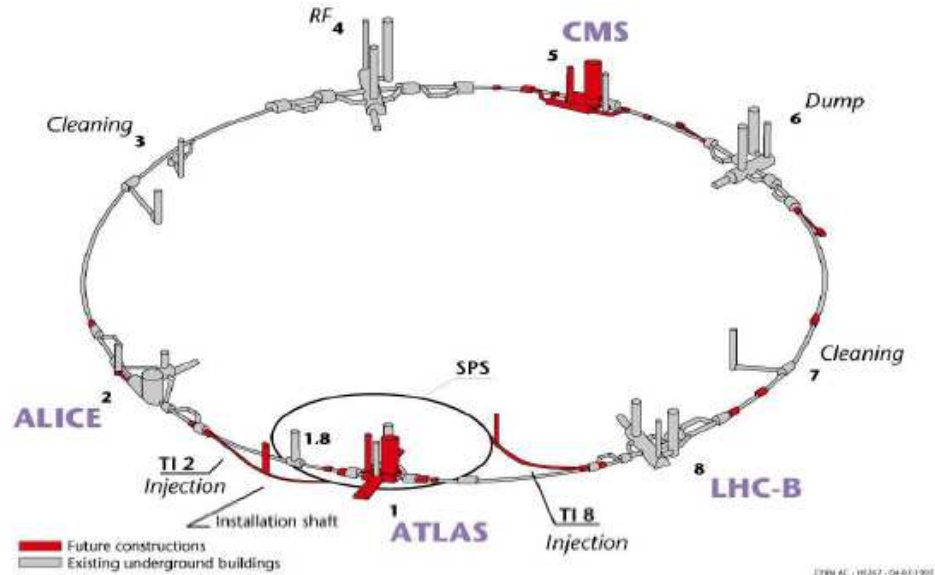
Figure 3.3: *The LHC tunnel with the detector infrastructure*

- study of the top and bottom (CP violation) production processes.

- search for phenomena of new physics beyond the Standard Model such as supersymmetry particles or technicolor particles.

- detailed investigations of the Standard Model physics, especially QCD.

- investigate properties of quark gluon plasma in heavy ion collisions.

Most of these processes will provide final states with high p_T leptons, high E_T hadron jets, b-jets and large missing energy. Therefore, good detectors are needed. In the next section the basic detector requirements and the capabilities of the CMS experiment will be described.

3.2 The Compact Muon Solenoid Detector

The CMS detector is built to identify particles and measure their position momenta and energy. The CMS experiment will look for the Standard Model Higgs boson and new physics. Physics of the heavy top and bottom quarks will be studied. The detector was designed to distinguish cleanly the diverse signatures from new physics. The detector has a cylindrical symmetry around the beam direction. It is composed of several sub-systems, positioned around each other in concentric layers around the interaction point. In the forward regions, endcaps are placed to cover an angle of almost 4π.

An overview of the detector and the various subdetectors is given in Figure 3.4. The detector has a length of 20 m, a diameter of 14 m and a weight of about 12000 tons. From the interaction point to the periphery one is able to distinguish the following subsystems:

- The tracking subsystem, which must achieve a track identification with very high resolution in the central region of the detector.

- The electromagnetic calorimeter (ECAL), which is dedicated to the very precise measurement of the energy of the electrons and photons.

- The hadron calorimeter (HCAL), which measures the energy of the hadronic particles.

- The superconducting solenoid, with a length of 12 m and a diameter of 6 m, which will provide a uniform magnetic field of 4 T to bend the charged particles.

- An accurate and efficient muon subsystem, as the decay of the Higgs boson in four muons is the clearest signature in the mass range of 140 to 500 GeV. A very good identification and momentum measurement for muons will be usefull in other events as well.

Each of the above subsystems, except for the solenoid, consists of a central "barrel" part and two "forward" parts forming the endcaps. Outside the endcaps two hadron calorimeters (Very Forward Calorimeter) are placed. Figure 3.5 shows the concentric layers of the CMS detector.
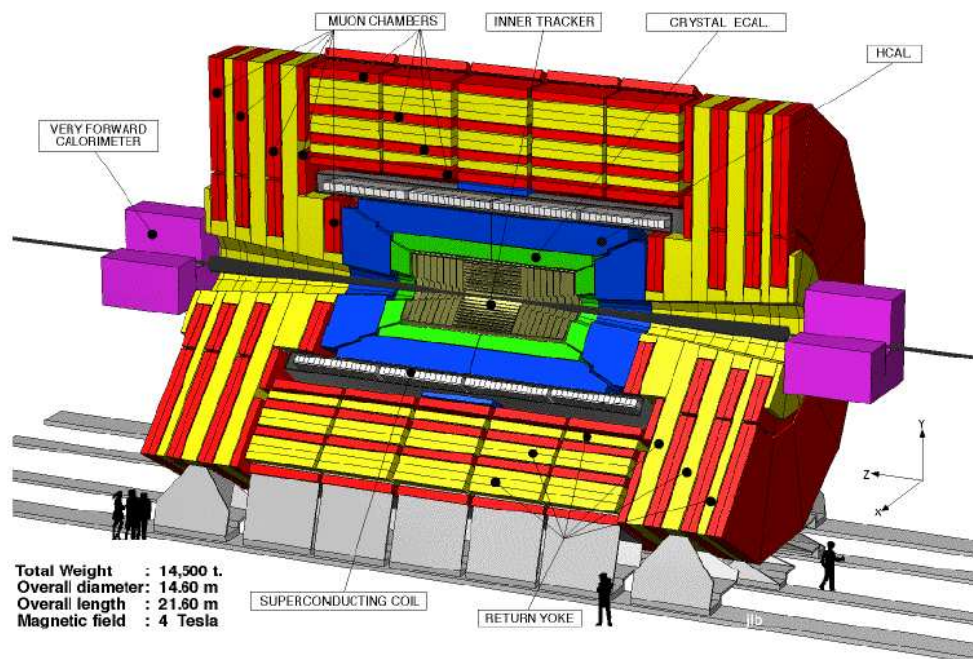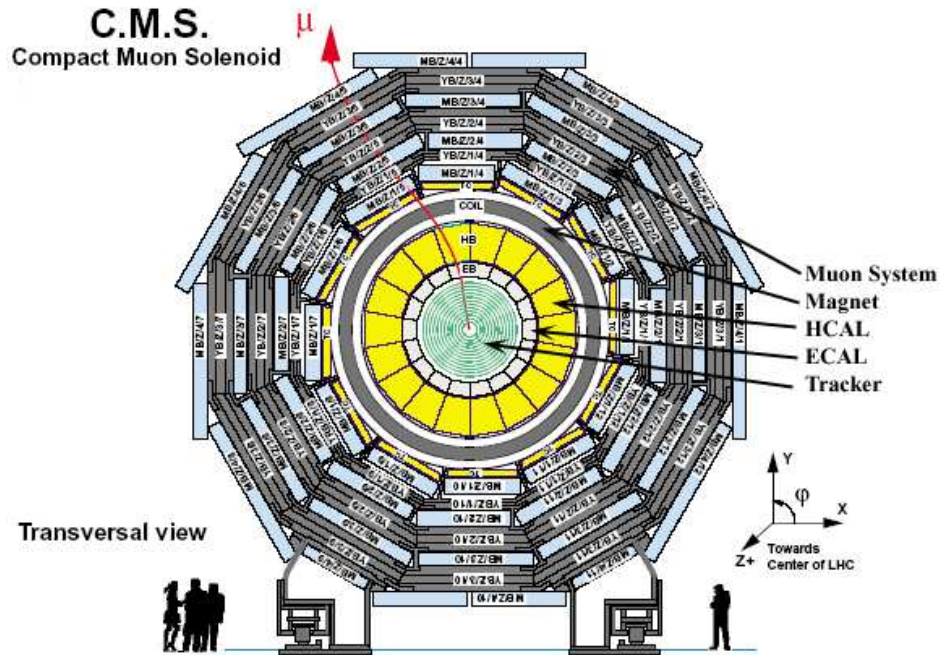

Figure 3.4: *Overview of the CMS detector.*

Figure 3.5: *Transversal view on the crosssection of the CMS experiment.*

It is usefull to introduce some coordinates for the following. The z coordinate is defined by the beam direction while the x coordinate is pointed towards the center of the LHC tunnel and the y coordinate is pointed upwards. To describe the angle between the outgoing particle and the undeflected beam (or the z axis), the polar angle θ is used. The angle in the transverse plane is ϕ. These variables are shown in Figures 3.4 and 3.5. Another variable is introduced along the longitudinal plane, which is called the pseudorapidity η. This Lorentzinvariant variable is defined by $ln(tan\frac{\theta}{2})$. On Figure 3.6 the longitudinal view of one quarter of the detector is shown, with some values for η.

In the following, a description of the different subdetectors and their capabilities will be given.

3.2.1   The Tracker System

The tracker is the subdetector closest to the interaction point. It is designed to measure precisely the momentum of charged particles. Its main goal is the reconstruction of charged tracks and vertices in the magnetic field of 4 T, e.g. the muons with a high transverse momentum, electrons and hadrons. It should provide a high momentum resolution and a high efficiency in the range of $\eta < 2.4$. The inner tracking detectors will be able to allow the identification of tracks coming from detached vertices. The tracker system will be a key device for searches for new physics and Standard Model physics. The system is completely based on semiconductor detectors, more exactly: on layers of silicon detectors. This layered charged particle detector is highly segmented and involves millions of channels. If a particle crosses a channel, its presence will be recorded and used for the reconstruction of its track.
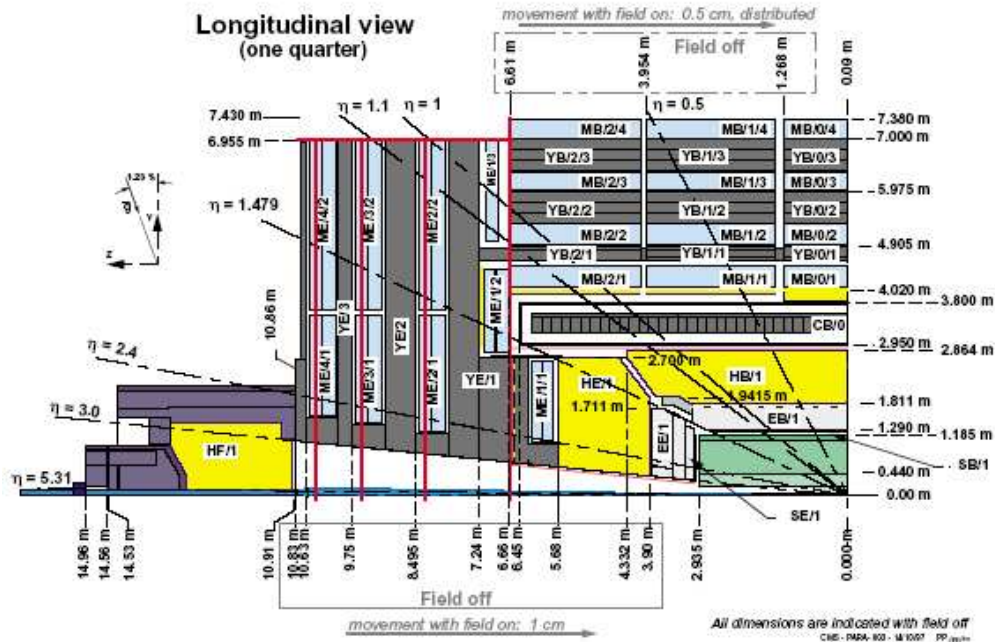
Figure 3.6: *Longitudinal view of one quarter of the CMS detector.*

The radius of curvature in the magnetic field will determine the momentum of the charged particle. Close to the beam pipe, where the density of tracks is large, layers of silicon pixels are used. Further away from the beam pipe layers of silicon strips are used. To enhance the radiation hardness, the system will be cooled down to -10 C. The total length will reach 540 cm and the radius extends up to 110 cm. The layout of the tracker is shown in Figure 3.7.

The innermost part of the tracker is made of two layers of silicon pixel detectors. This will provide a good precision in the extrapolation to the primary vertex. As can be seen on Figure 3.8 the pixel system consists of two barrel layers complemented by two disks in the forward region. The pixel detector will make very precise measurements of impact parameters and vertices possible, which is important for the tagging of the jets originating from the decay of heavy hadrons containing b and c quarks and for top quark studies. The resolution of the impact parameter will be 35 μm in the transverse plane and 75 μm in the longitudinal direction. The pixel layers consists of modular units. Each of these modules is composed of a segmented sensor plate with integrated readout chips connected to them using the bump bonding technique. The size of one pixel is 100×150 μm. There will be about 1400 detector modules and on each module there are 16000 readout chips. The total number of pixels or readout channels will be 45×10^6.

The silicon strip detector is placed around the pixel detector. This part of the tracker detector consists of four parts. The tracker inner barrel (TIB), organized in four barrel layers. At each side of this four barrel layers there are three minidisks, tracker inner disks (TIDs). The outer part is composed of six barrel layers, the tracker outer barrel (TOB) which surrounds the TIB. The tracker endcap (TEC) is placed at each side of the barrel with nine disks in each endcap. This geometry is depicted in Figure 3.9. These parts of the tracker allow
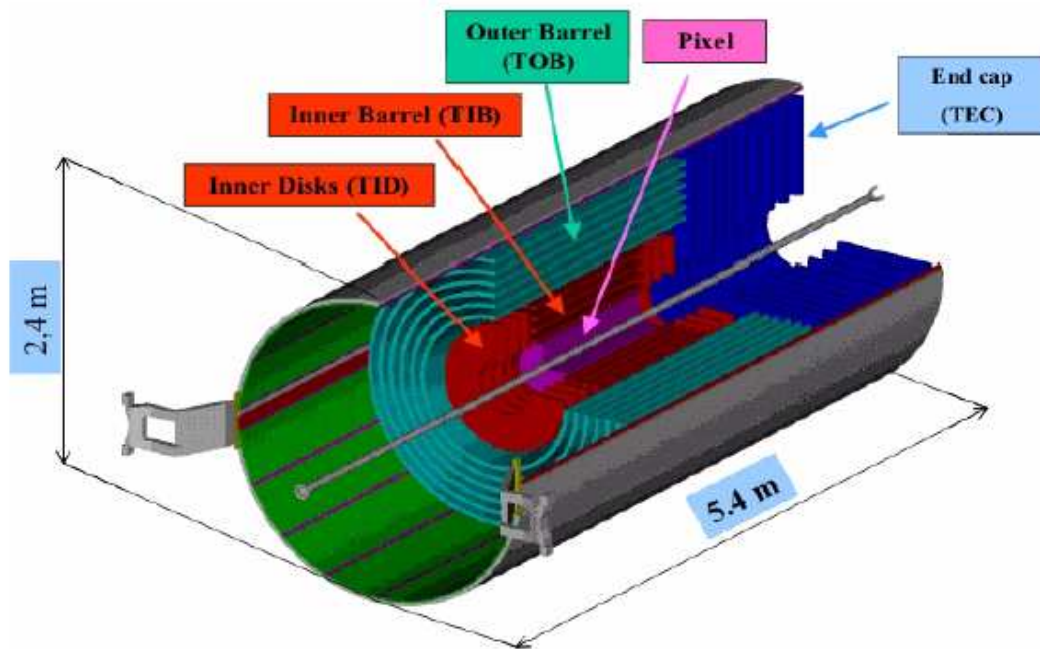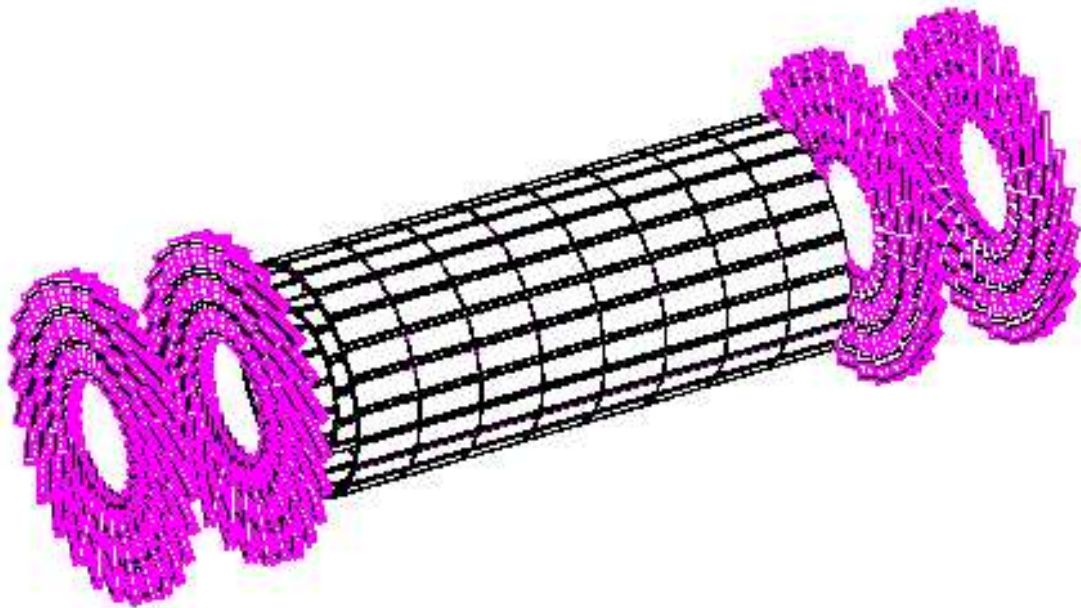
Figure 3.7: *The tracker system.*

Figure 3.8: *The pixel detector.*

an efficient pattern recognition, a precise measurement of the track momentum and a good matching with the outer detectors.
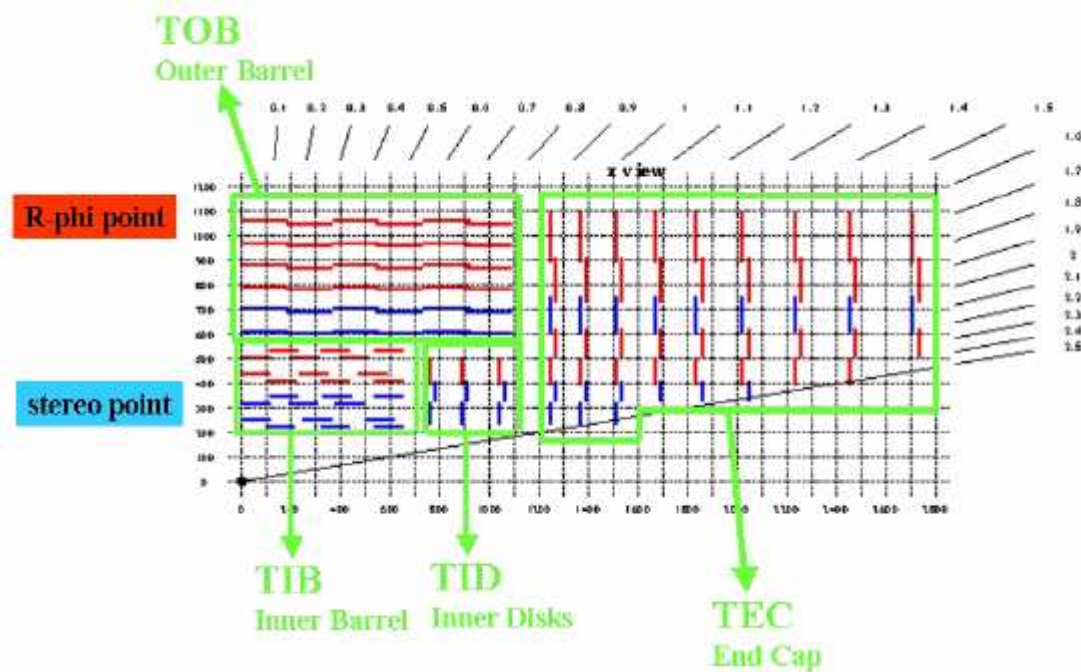
Figure 3.9: *The geometry of the silicon strip detector.*

3.2.2 The Electromagnetic Calorimeter

The electromagnetic calorimeter will measure the energy and the direction of photons and electrons in the rapidity region up to $\eta < 2.6$. As the reconstruction of the Higgs boson in the decay of the Higgs into two photons relies completely on the photon reconstruction, the electromagnetic calorimeter was designed in orde to achieve the best sensitivity for the decay of the Higgs boson in two photons. The electromagnetic calorimeter is made out of lead tungstate $PbWO_4$ crystal scintillators. This material was chosen because it is radiation resistent and chemically inhert. In addition, the material has a very short decay time (≈ 10 ns) for scintillation radiation emission and a small dead time. Because of its high scintillation speed, seperate bunch crossings are identified and pile-up effects minimized. The radiation length of the crystals is 8.9 mm, which allows a compact device. The layout of the ECAL is shown in Figure 3.10.

Barrel crystals have a length of 23 cm, which corresponds with 26 radiation lengths and allows an almost complete shower containment. The crystals in the endcaps have a length of 22 cm. The granularity in the barrel region is $\Delta\eta \times \Delta\phi \approx 0.0175 \times 0.0175$. This resolution will be high enough to seperate two photons from π^0 decay. Since the granularity decreases with increasing η, a maximum for the granularity is obtained when $\Delta\eta \times \Delta\phi \approx 0.05 \times 0.05$ in the very forward crystals. However, this will not be enough to separate the two photons of the π^0 decay. Therefore, a silicon detectors preshower will be installed in front of the endcaps. The preshower will be three radiation lengths deep, so the endcap crystal lengths will be reduced to 22 cm. To read out the signals, avalanche photodiodes were chosen in the barrel region, while vacuum phototriodes will be used in the endcap regions, because of the
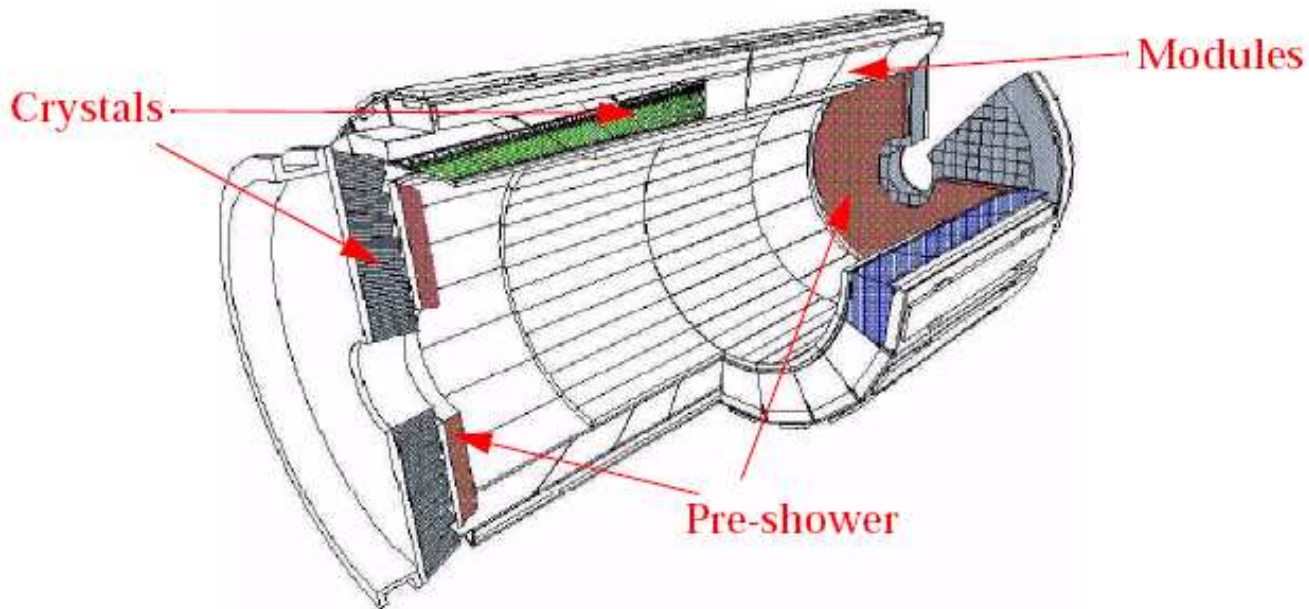
Figure 3.10: *Layout of the electromagnetic calorimeter.*

higher radiation dose.

3.2.3   The Hadron Calorimeter

The hadron calorimeter surrounds the ECAL and is used in conjunction with it to measure the energies and directions of particle jets and the missing energy of particles not interacting in the detector, such as neutrinos or new particles. It is also used to identify electrons, photons and muons. The detector must be thick enough to contain the fully hadronic shower and it must be completely hermetic. The calorimeter used in the CMS experiment will be made of active layers alternated with absorbers. For the active layers, plastic scintillators are used. The plastic scintillator tiles are 4 mm thick. This material has been chosen for its short interaction length and because it isn't affected by the magnetic field. The tiles are placed in projective towers with fine granularity to make a good di-jet separation and mass resolution possible. The HCAL segmentation is $\Delta\eta \times \Delta\phi \approx 0.087{\times}0.087$. The absorbers are made out of copper. The layout of the HCAL is shown in Figure 3.11.

The HCAL is about 8.9 interaction lengths deep in the barrel region and about 10 in the endcaps. The scintillation tiles and the copper in the forward region are replaced by quartz fibers embedded in steel absorbers, because of the high radiation dose expected there. Two forward HCALs will be used to increase the acceptance to rapidities of $\eta \leq 5$. In the area for $\eta = 0$ the calorimeter is about 79 cm thick, which will not be enough to contain the full hadronic shower. This results in a low-energy tail in the hadron distribution. Those tails can be avoided if one adds a so-called tail catcher. With this additional detector subsystem it is possible to identify and quantify jets from late starting showers.
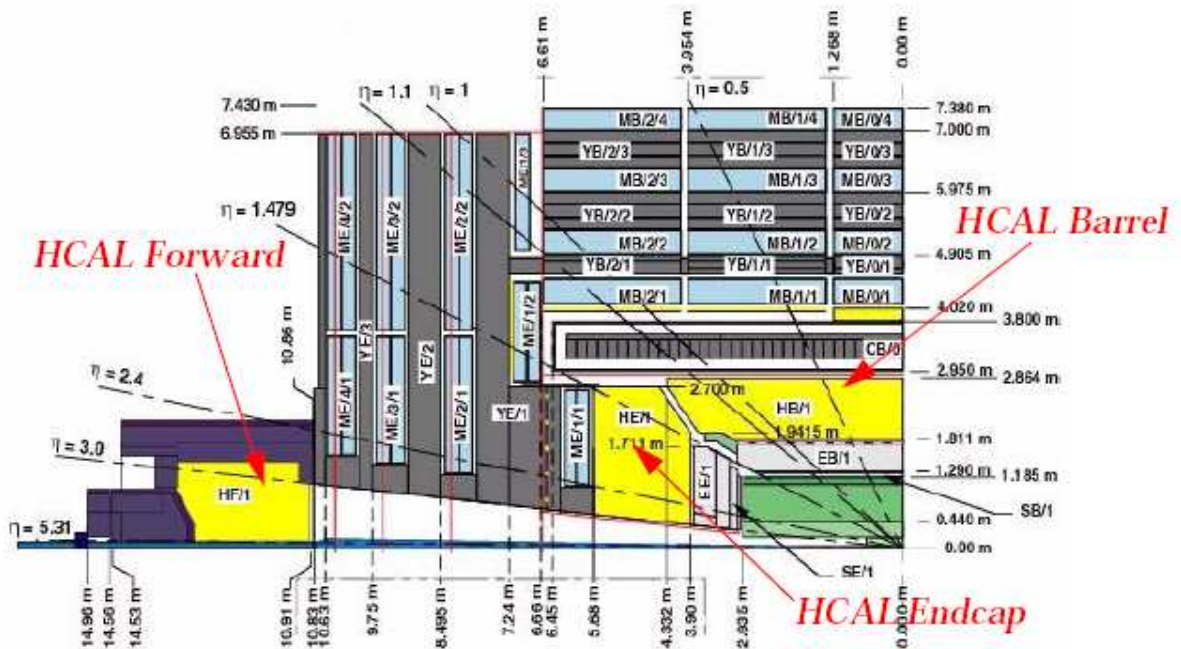
Figure 3.11: *Layout of the hadron calorimeter.*

3.2.4 The Muon System

The only particles able to pass the other detectors without being stopped are muons and neutrinos. The aim of the muon system is to detect the muons. Muons are key signatures for most of the physics the LHC is designed to explore and are often present in the final state topology. The central concept of the CMS experiment is the ability to trigger on and reconstruct muons at the highest luminosities. The layout of the muon system is shown in Figure 3.12.

The system consists of five cylinders surrounding the magnet and two endcaps. The detectors of the muon system are placed in the iron return yoke of the magnet. In different regions of the experiment, three different types of gaseous particle detectors will be used: drift tubes in the barrel region, cathode strip chambers in the endcap region and resistive parallel plate chambers in both regions. The drift tubes and the cathode strip chambers will be dedicated to precise measurements of the position of the muons. The resistive plate chambers will provide fast response and an excellent time resolution. The system will provide a coverage over $0 < \eta < 2.4$.

The barrel muon chambers consist of drift tubes and provide a coverage up to $\eta < 1.3$. A drift tube is made of aluminium cathodes of 1.2 mm thick and 9.6 mm long and stainless steel anode wires of 50 μm strung at the center of the tubes. The drift chambers have an area of 4×1.1 cm^2 and a maximum drift distance of 2 cm. They are filled with an ArCO$_2$ mixture. When an ionizing particle passes through the tube, it will liberate electrons, which will move along the field lines to the wire. The coordinate perpendicular to the wire will be obtained with high precision from the time taken by the ionization electrons to migrate to the
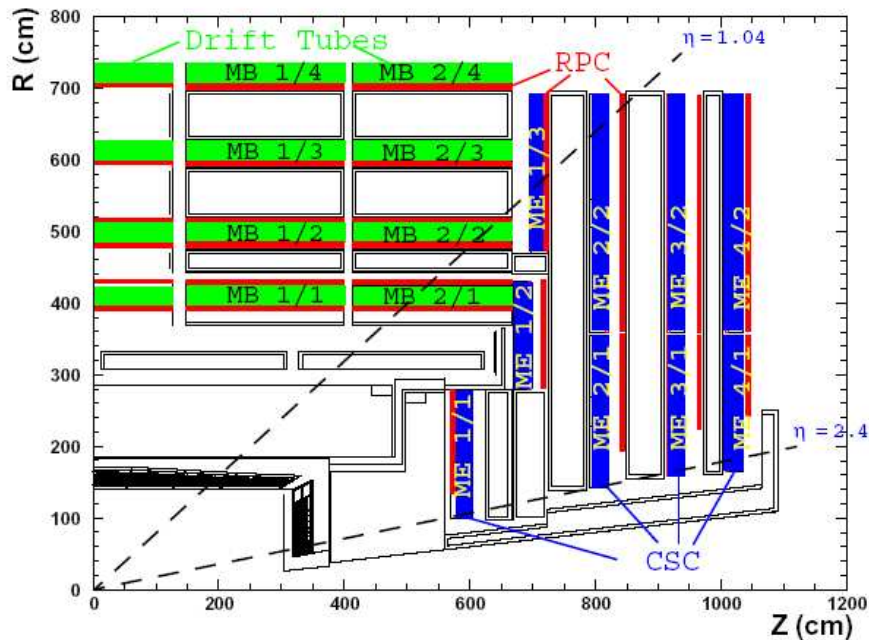
Figure 3.12: *Layout of muon system.*

wire. This time translates to the distance from the wire by mupltiplying it with the electron drift velocity in the gas. Each barrel muon chamber consists of twelve layers of drift tubes grouped into three superlayers of four layers each. The first and the third will measure the ϕ coordinate of the muon crossing point, while the second will measure the z coordinate. If the distance between the first and the third superlayers is maximized, a resolution of about 1 mrad will be obtained in the transverse plane. There will be about 250 chambers with 200000 individual electronics channels. Drift tubes will only be used in the barrel part, because the particle rate is low enough (lower than 10 Hz/cm^2), so that a response time of the order of 400 ns with cell occupancy below 1% is allowed.

Endcaps extend the coverage up to $\eta < 2.4$. In the endcaps cathode strip chambers are used to provide high precision measurements in the presence of the large and varying field. The cathode strip chambers have a faster response time, which will be necessary at the energies that will be produced in the LHC, as there will be a very high fraction of muons with a high rapidity. A cathode strip chamber is a multiwire proportional chamber in which the cathode is subdivided into strips running across wires. An avalanche developed near a wire will induce a charge on several strips of the cathode plane. Two coordinates per plane are made available in a cathode strip chamber by the simultaneous and independent detection of the signal induced by the same track on both the wires and the strips. The radial coordinate is given by the wires, while the strip measures the angle ϕ. The chambers are filled with an ArC0$_2$CF$_4$ gas mixture. The whole cathode stripchamber system is made of 540 chambers with 220000 anode wires and 320000 cathode strips.

An additional muon trigger is provided by the resistive plate chambers. These detectors have a high time resolution. They combine a good spatial resolution with time resolution of

≈ 1 ns, comparable to that of scintillators. They can be highly segmented to make it possible to measure transverse momentum at trigger time as they do not need a costly readout device. A resistive plate chamber consists of two phenolic resin planes separated by a gap of a few mm filled by a gas. The planes are placed parallel and are coated with a conductive graphite paint to form the electrodes. When a muon crosses the chamber, a cluster of electrons starts an avalanche multiplication. When the drift of this electrons approaches the anode, the anode will produce a signal by inducing a fast charge on the other anode. The spatial resolution is of the order of the strip size.

3.3   The CMS trigger system

The purpose of the trigger system is to reduce the 40 MHz event rate down to a value of about 100 Hz, which is the maximum that can be archived for offline analysis. This reduction is subdivided in several steps. The first level, Level 1, will reduce the event rate to 100 kHz. In a second stage, this rate will be reduced to 100 Hz by high levels, Level 2 and Level 3. At the lowest level, the bulk of background must be removed, while a more precise reconstruction is performed at higher levels. All trigger devices work in the pipeline: each unit synchronously performs its task in 25 ns and transmits its output to the following one. All detector information should be kept until a decision is made, which restricts the total Level 1 processing time. The High Level trigger (HLT) is implemented on farms of commercial processors which run selection algorithms on the readout data of the Level 1 accepted events. After that, the selected events are forwarded to the CMS data acquisition system (DAQ) for mass storage. A schematic view of the CMS trigger system is given in Figure 3.13.

The Level 1 trigger is entirely based on hardware and is organized in three major subsystems: the Level 1 calorimeter trigger, the Level 1 muon trigger and the Level 1 global trigger. In Figure 3.14 an overview of the Level 1 trigger flow is given.

The first phase is a regional phase, where calorimeter and muon data are analyzed locally to achieve a coarse reconstruction of jets and leptons. After that, the informations are combined together to extract the missing transverse momentum. The muon trigger is organized in three different subsystems, according to the three different muon detector systems, the drift tubes, the cathode strip chambers and the resistive plate chambers. The trigger information from these three detector systems is combined to the global muon trigger, which will check for ambiguities and remove fakes. After that, the information is send to the Level 1 global trigger. The calorimeter Level 1 trigger combines the coarse calorimetric towers from the ECAL, the HCAL and the circuits in the regional calorimeter trigger. This part of the trigger is able to reconstruct jets, leptons and photons, whereafter the information is send to the global trigger. The regional calorimeter trigger provides also a map of the inactive calorimetry regions to improve the muon isolation. The decision whether to trigger on a specific crossing or to reject it, is transmitted via the trigger timing and control system to all the detector subsystem front-end and read-out systems.

The Level 1 trigger exploits only a small subset of data, which can be collected very rapidly at each bunch crossing. Trigger candidates are constructed with the low resolution and coarse granularity information which is obtained from local pattern recognition in the muon system and from the calorimeters, macrogranular energy evaluation is used. For the
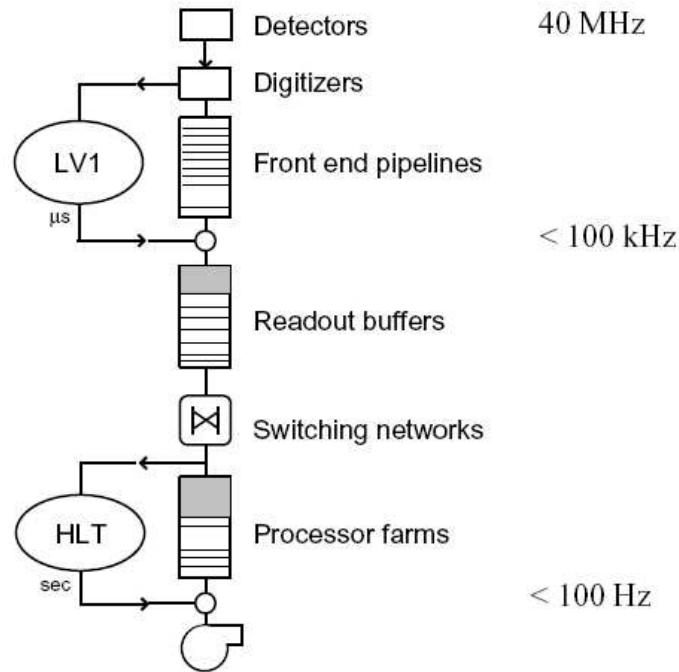
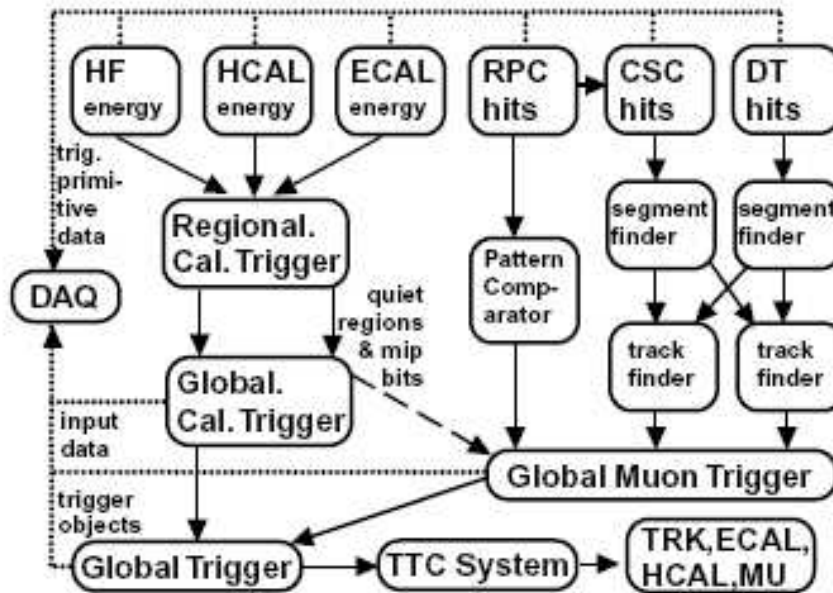Figure 3.13: *Data flow in the CMS trigger system.*

Figure 3.14: *Overview of the Level 1 trigger flow.*

following classes of physics objects: muon, isolated electrons and photons, non-isolated electrons and photons, central jets and forward jets, the four most energetic candidates are

identified. An estimation of the total visible and missing transverse energy will be calculated. A position and transverse momentum measurement together with other properties, will be provided for each of the trigger candidates. To these properties (quality indicators or bunch crossing identification), threshold cuts will be aplied, to select the most interesting events. After these threshold cuts, the output rate after the Level 1 trigger will be 50 (100) kHZ in the low (high) luminosity period. The accepted events after the Level 1 trigger are distributed to the subsystems and data is stored in 3.2 μs pipelines. After this Level 1 decision time the accepted signals are send to the PC farms. In Table 3.2 an example of the threshold cuts for the Level 1 trigger is given.

Trigger	Threshold (GeV)	Rate (kHZ)	Cumulative Rate
Inclusive isolated electron/photon	29	3.3	3.3
Di-electrons/di-photons	17	1.3	4.6
Inclusive isolated muon	14	2.7	7.0
Di-muons	3	0.9	7.9
Single tau-jet trigger	86	2.2	10.1
Two tau-jets	59	1.0	10.9
1-jet, 3-jets, 4-jets	177, 86, 70	3.0	12.5
Jet*E$_T^m iss$	88*46	2.3	14.3
Electron*Jet	21*45	0.8	15.1
Minimum bias (calibration)		0.9	16.0
Total			16.0

Table 3.2: *Level 1 trigger table at low luminosity. Threshold corresponds to values with 95% effi ciency.*

The High Level trigger is designed to reduce the rate from 100 kHz to 100 Hz. The High Level trigger consists of two triggers: the Level 2 and Level 3 trigger. All High Level trigger algorithms are executed in a single processor farm. In the first selection step of the High Level trigger, the event rate is reduced by a factor 10 by applying the treshold of Level 1 to more accurately reconstructed objects. Since an event is received every 10 μs more time is available to take a decision and finer granularity and resolution information can be used together with some primary tracking information from the pixel detectors, like primary vertex information and track reconstruction. Not all tracker information is used to avoid a saturation of the system bandwidth by reading out the large volume of data from the tracker detector. The leptons and jets reconstructions are refined. Only for the following step of the High Level trigger, the full event data will be transferred to the farm. The full tracker information will be used to perform an online analysis allowing to identify the physics process. The final output rate will be 100 Hz.

The High Level trigger decision will be sent to the data acquisition system and the whole event data will be recorded in the mass storage system.

Chapter 4

Production of the Z' boson in proton collisions

In a number of physics processes at the LHC it is possible to produce an addiditional gauge boson Z' motivated by Technicolor models. In this chapter, the cross section will be given for the production of a Z' boson in proton collisions at 14 TeV according to TC2 models. The decay of the Z' boson into top quark pairs will be considered as well as background. The event generator PYTHIA will be used to obtain the cross sections for the production of the Z' boson and the background.

4.1 Production and decay of the Z' boson

At the LHC a Z' boson could be produced by the collision of a quark and an anti-quark from the protons or by the collision of two gluons. As mentioned in chapter 2 (section 2.5) the Z' boson is strongly coupled to the third generation quarks. Therefore, in the following, the decay channel Z'$\rightarrow t\bar{t}$ will be observed. Other decay channels are possible, but will not be used in the analysis. The branching ratio of the Z' boson decaying in a $t\bar{t}$ pair will be taken 100% for simplicity. The top quark has a decay of almost 100% to the W gauge boson and the bottom quark [1]. The $t\bar{t}$ pair will thus decay into $WbW\bar{b}$. In this analysis one of the two W bosons is required to decay leptonically into an muon and neutrino in order to exploit the triggers based on isolated high p_T muons, while the other one is required to decay hadronically to increase statistics [2]. Thus, signal events will consist of two b-jets, two non b-jets from one of the W bosons, a muon and large E_T^{miss} due to a neutrino. This final state will be denoted as $bbpq\mu\nu$ [3]. This decay is chosen as signal because it is the simplest one from experimental point of view. Fully hadronic events will require a more complex jet reconstruction and suffer from a higher background and are therefore not considered. Fully leptonic events suffer from lower statistics and can not be used in a kinematical fit to calculate the mass of the $t\bar{t}$ spectrum as there are two neutrinos in this case instead of one.

---

[1]In the following the charges of the particles will be omitted. The quarks will be denoted with the first letter.

[2]The branching ratio of a W boson decaying leptonically is approximately 1/3 and for a W boson decaying hadronically approximately 2/3

[3]The notation to differentiate between particles and antiparticles is omitted for simplicity.

Background will be produced mainly by non-resonant $t\bar{t}$ production. The particle content in these events and the particle content in the decay of the Z' boson will be the same, therefore this contribution to the background is called irreducible background, as it can't be eliminated entirely by selection cuts. The main difference will be on the kinematics, since the Z'$\rightarrow t\bar{t}$ events will produce higher p_T particles and larger E_T^{miss} compared to non-resonant $t\bar{t}$ events. An other contribution may come from the QCD W+jets final state because it has a high cross section. However, this contribution will be reduced by the selection cuts for $t\bar{t}$ rejection and b-tagging. Other contributions, like events with a boson pair or Z+jets events may be considered negligible after the selection cuts.

4.2   The event generator PYTHIA

The primary interaction was generated with the PYTHIA version 6.223 package [35]. This package is used to generate high energy physics events in particle collisions. It simulates the hard interactions in ee, pp and ep colliders. Complete events are generated according to the Standard Model calculations or calculations based on models beyond the Standard Model. The effect of color confinement for example is simulated perturbatively by DGLAP equation and, when perturbation breaks, by the string model fragmentation. The event generator PYTHIA should contain a simulation of a number of physics aspects in order to describe a high energy event:

- The two beam particles are moving towards each other and each parton is characterized by a set of parton distributions.

- These incoming protons may branch to build up an initial state shower.

- From these initial state showers, one parton of each shower (the shower initiator) will enter the hard process, where a number of outgoing partons are produced. The nature of this process determines the main characteristics of the event.

- A set of short living resonances may be produced in the hard process. The normal partons originating from the decay of these resonances are considered in association with the hard process.

- The outgoing partons start off a sequence of branchings to build up final state showers.

- Semi hard interactions may occur between the other partons of two incoming hadrons.

- When the shower initiators interact in the hard process, the beam remnants are left behind. These remnants may have an internal structure and a net color charge, which relates the remnants to the final state.

- Due to the QCD confinement, the outgoing quarks and gluons are not observable as they fragment to color neutral hadrons.

- The produced hadrons possibly decay further.

Events are thus generated with a simulation of the high energy physics before, during and after the collision. Simulation of the detector response will be considered in chapter 5.

The main parameters of the PYTHIA program used for the generation of the events are summarized below:

- The center of mass energy is set with the parameter ECM at 14 TeV;

- The mass of the Z' boson is variated between 750 and 2000 GeV/c^2 (m$_{Z'}$ = 750, 1000, 1500, 2000 GeV/c^2);

- To produce Z' bosons, the parameter MSEL is put at 21. In this way an interference γ^*/Z'/Z^0 will be produced. To select only the Z' boson component, an additional parameter is used (MSTP 44 = 3);

- For the parton distribution a leading order parton distribution called CTEQ5L is used;

- b-fragmentation is taken into account with the parameter MSTJ 11 = 3, which uses b-fragmentation Peterson function;

- The decay channel of the Z' $\rightarrow$ $t\bar{t}$ is opened with the parameter MDME 294,1 =1. Other decay channels are closed;

- The requirement for one W boson decaying hadronically and the other leptonically is taken into account by the parameters MDME 190 $\rightarrow$ 209,1 = 1.

Background is generated in a similar way, for instance for non-resonant $t\bar{t}$ production, MSEL = 6 instead of 21.

4.3 Cross section for the Z' boson production and for the background

The data used for the analysis is generated for an integrated luminosity of 30fb^{-1}, which is the value for the integrated luminosity collected after three years in the low luminosity period of the LHC. The analysis is performed in the low luminosity running. For the high luminosity period a different detector performance is expected, therefore the analysis have to be revised for these accelerator settings.

The cross sections of the process $pp \rightarrow Z' \rightarrow t\bar{t}$ obtained with the PYTHIA program are leading order cross sections and are summarized in Table 4.1. The branching ratio of the Z' boson into $t\bar{t}$ is assumed to be 100%. The analysis aims to look for Z' boson masses between 750 and 2000 GeV/c^2 as the cross sections for higher masses are too small to be visible at low luminosity above the background. Another reason why high masses will not be considered is because the reconstruction tools don't suffy. For high masses, and thus higher energies and momentum, the jets overlap due to the boost of the top quark. Thus, it becomes difficult to reconstruct the jets resulting from the hadronically decay of the top quark. This can be seen from Figure 4.1. The largest angle between the direction of the generated top quark and the direction of the jets resulting from its hadronic decay becomes smaller for higher masses.
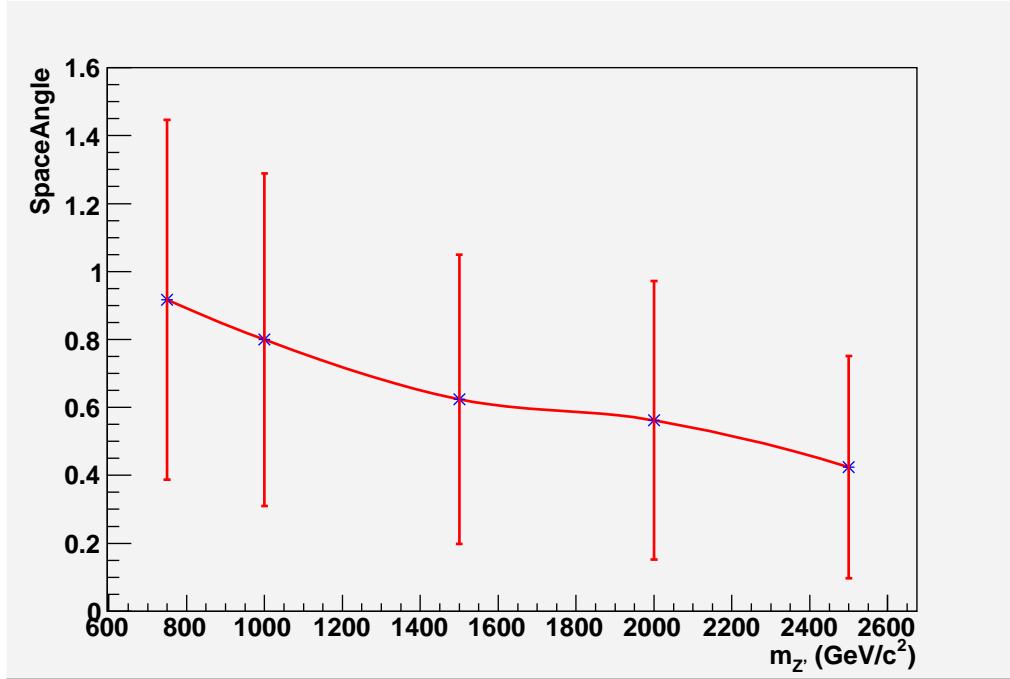
Figure 4.1: *The largest angle (in rad) between the direction of the generated top quark and the direction of the jets resulting from its hadronic decay becomes smaller for higher masses. The error bars reflect the RMS or spread on this angle.*

For high Z' boson masses, the cross section $\sigma\left(pp \rightarrow Z' \rightarrow t\bar{t}\right)$ is decreasing because for an increase of mass an increase of energy is needed. As the center of mass energy is fixed at 14 TeV, hence the cross section decreases with increasing mass of the Z' boson. As can be seen from Table 4.1 the cross section of non-resonant $t\bar{t}$ processes in the Standard Model is much larger compared to Z' boson production. It should be mentioned that all the cross sections are calculated for top quark pairs decaying inclusively and not only semi-leptonically. Therefore, if one is interested in the cross sections for the semi-leptonic decay only, the numbers in Table 4.1 should be multiplied with the branching ratio for the semi-leptonic decay. The signal that will be studied is the semi-leptonic muon decay of the Z'. The branching ratio of $t\bar{t}$ decaying to $bbpq\mu\nu$ is 4/27, as can be seen from Figure 4.2 where the possible final states of the $t\bar{t}$ decay are summarized. The cross sections are determined in leading-order. If next-to-leading order calculations are taken into account, the $t\bar{t}$ cross section increases to 840 pb [36]. The cross sections for the Z' boson are taken from calculations done in [37].

With the results in Table 4.1 one is able to calculate the number of events that have to be generated to obtain a sample of integrated luminosity of 30 fb^{-1}. The number of events for each mass of the Z' boson and for the $t\bar{t}$ background are summarized in Table 4.2.

It is interesting to know what happens to the cross section if one observes the interference $\gamma^*/Z'/Z^0$ boson instead of the Z' boson. Results for the cross section of the interference are summarized in Table 4.3. In Figure 4.3 the cross section dependence on the mass is shown, both for the Z' boson production and the production of the interference. The cross section

Sample	Cross section (fb)
$t\bar{t}$ background	$4.9 \ 10^5$
$m_{Z'} = 500 \text{ GeV/c}^2$	9139
$m_{Z'} = 750 \text{ GeV/c}^2$	3511
$m_{Z'} = 1000 \text{ GeV/c}^2$	1272
$m_{Z'} = 1500 \text{ GeV/c}^2$	265
$m_{Z'} = 2000 \text{ GeV/c}^2$	70
$m_{Z'} = 2500 \text{ GeV/c}^2$	22
$m_{Z'} = 3000 \text{ GeV/c}^2$	7.0
$m_{Z'} = 3500 \text{ GeV/c}^2$	2.2
$m_{Z'} = 4000 \text{ GeV/c}^2$	0.9
$m_{Z'} = 4500 \text{ GeV/c}^2$	0.5
$m_{Z'} = 5000 \text{ GeV/c}^2$	0.1

Table 4.1: *Cross section for signal $pp \rightarrow Z' \rightarrow t\bar{t}$ and background $pp \rightarrow t\bar{t}$ processes obtained with* PYTHIA *version 6.223.*

Sample	Number of events at 30 fb^{-1}
$t\bar{t}$ background	$147 \ 10^5$
$m_{Z'} = 500 \text{ GeV/c}^2$	274170
$m_{Z'} = 750 \text{ GeV/c}^2$	105330
$m_{Z'} = 1000 \text{ GeV/c}^2$	38160
$m_{Z'} = 1500 \text{ GeV/c}^2$	7950
$m_{Z'} = 2000 \text{ GeV/c}^2$	2100
$m_{Z'} = 2500 \text{ GeV/c}^2$	660
$m_{Z'} = 3000 \text{ GeV/c}^2$	210
$m_{Z'} = 3500 \text{ GeV/c}^2$	66
$m_{Z'} = 4000 \text{ GeV/c}^2$	27
$m_{Z'} = 4500 \text{ GeV/c}^2$	15
$m_{Z'} = 5000 \text{ GeV/c}^2$	3

Table 4.2: *Number of expected events that correspond to an integrated luminosity of 30 fb^{-1}.*

of the Z' boson with the interference is higher compared to the production of the Z' boson without the interference. This is because for higher masses of the Z' boson, the production of a Z^0 or γ^* boson with lower mass becomes more advantageous than the production of the heavier Z' boson. This is why for masses m_X higher than 1000 GeV/c^2 the resonance for the Z' boson disappears. This can be seen in Figure 4.4. The invariant $t\bar{t}$ mass distribution for the generated events is shown for both the interference and the Z' boson for the masses of 1000, 1500 and 2000 GeV/c^2. In the last figure, the invariant $t\bar{t}$ mass of the interference for a mass of 4000 GeV/c^2 is shown. The distribution is concentrated around 500 GeV/c^2
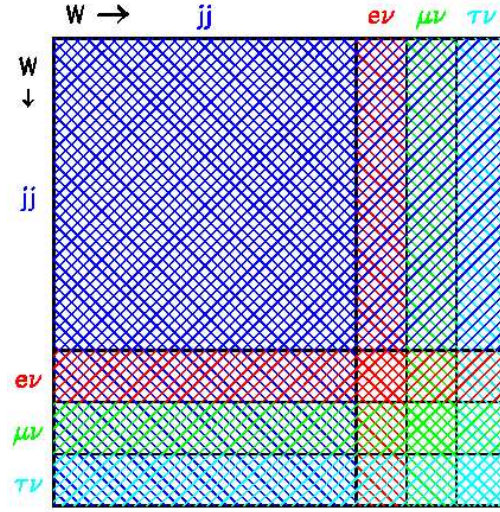
Figure 4.2: *Summary of the final states of the $t\bar{t}$ decay.*

instead of around 4000 GeV/c^2.

Sample	Cross section (fb)
$m_X = 500$ GeV/c^2	96795
$m_X = 750$ GeV/c^2	3746
$m_X = 1000$ GeV/c^2	1604
$m_X = 1500$ GeV/c^2	662
$m_X = 2000$ GeV/c^2	461
$m_X = 2500$ GeV/c^2	427
$m_X = 3000$ GeV/c^2	418
$m_X = 3500$ GeV/c^2	418
$m_X = 4000$ GeV/c^2	418
$m_X = 4500$ GeV/c^2	418
$m_X = 5000$ GeV/c^2	427

Table 4.3: *Cross section $pp \rightarrow \gamma^*/Z'/Z^0 \rightarrow t\bar{t}$ including the interference $\gamma^*/Z'/Z^0$ obtained with* PYTHIA *version 6.223. The branching ratio is taken 4/27 as the semi-leptonic decay of the $t\bar{t}$ into a muon is studied.*

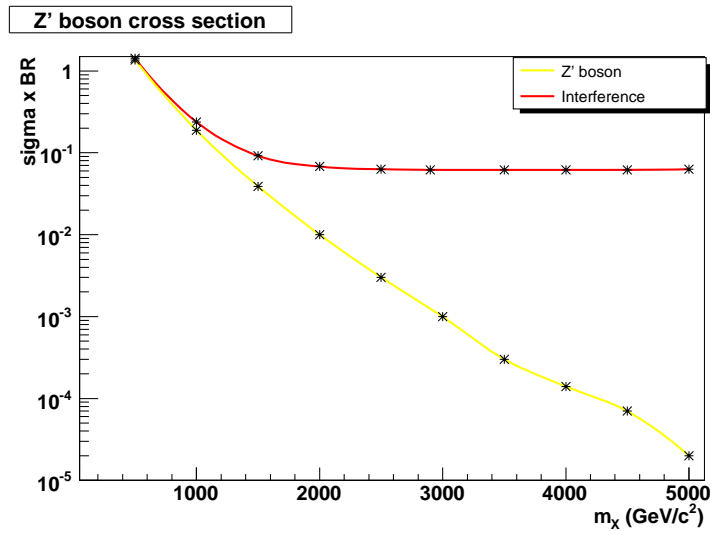In Figure 4.5 the generated mass of the $t\bar{t}$ system of non-resonant $t\bar{t}$ processes is shown.

Figure 4.3: *Comparison of the $\sigma \times BR$ in pb of the interference $\gamma^*/Z'/Z^0$ and the Z' boson as a function of the mass m_X. The cross section of the interference remains constant for masses higher than 1000 GeV/c^2 while the cross section of the Z' boson is decreasing.*
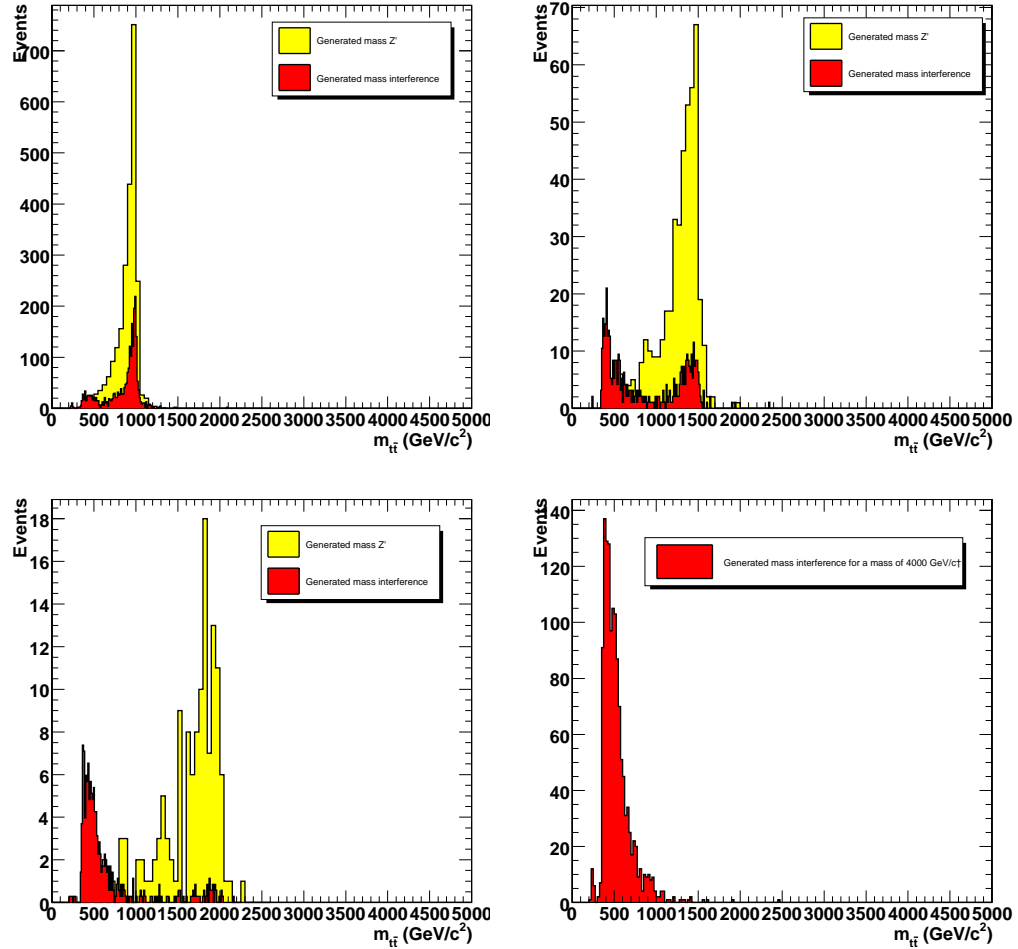
Figure 4.4: *Generated mass of the $t\bar{t}$ system with and without the interference. On the upper left figure the generated mass of the $t\bar{t}$ system for a mass of 1000 GeV/c^2 is shown, on the upper right for a mass of 1500 GeV/c^2 and on the lower left figure for a mass of 2000 GeV/c^2. In the lower right figure for a mass of 4000 GeV/c^2, the $t\bar{t}$ invariant mass distribution of the interference is concentrated around 500 GeV/c^2. It should be noted that for the interference, different bin size has been used than for the Z' resonance, the number of events has been scaled arbitrarily as the integrated luminosity is not the same for the intereference and the Z' boson.*
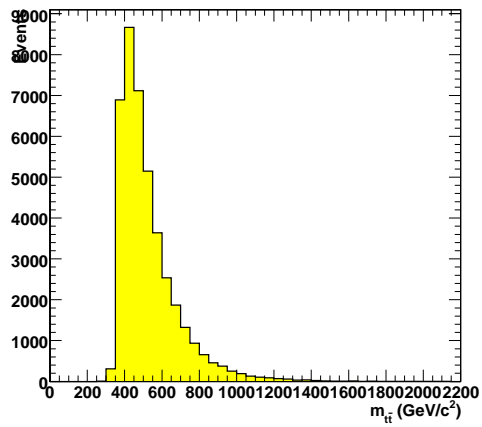
Figure 4.5: *Generated mass of the $t\bar{t}$ system of non-resonant $t\bar{t}$ processes.*

Chapter 5

Reconstruction and selection of $pp \rightarrow Z' \rightarrow t\bar{t}$ events

A method to generate events with the PYTHIA event generator was given in the previous chapter. These events are used as input for the detector simulation. In this chapter some information about the detector simulation is provided, as well as the methods used for the reconstruction of the lepton and jets in the simulated final state. The trigger and the selection cuts are described. In the last section the $t\bar{t}$ mass spectrum will be reconstructed.

5.1 Detector simulation

The object-oriented framework COBRA provides the reconstruction algorithms as well as the simulation tools to study the performance of these algorithms. In this framework, ORCA is implemented, consisting of the collection of the detector simulation and reconstruction code. Physics in the CMS detector is simulated by a package called OSCAR [38]. This package is based on the GEANT4 [39] simulation toolkit. After the generation of the events with an event generator, a configuration for the GEANT4 simulation is selected. With the generator events as input, persistent hits are produced in the sensitive detectors by the GEANT4-based simulation of CMS. The hit data are converted into digitizations to simulate the output of the CMS electronics. The GEANT4 simulation toolkit provides a full simulation. Electromagnetic and hadronic interactions are described in detail.

There exists also a framework for fast simulation of particle interactions in the CMS detector, referred to as FAMOS, which stands for FAst MOnte-Carlo Simulation [1]. All the events used for this thesis are simulated with FAMOS, because a many events will be simulated for the background. The list of particles obtained with the PYTHIA event generator is used as input for FAMOS. The particles in the list are characterized by their momentum and origin vertex, with mother and daughter relationships to make it possible to follow the various decay chains in the event. In FAMOS the following interactions are simulated:

- Electron Bremsstrahlung

---

[1]The computer time is about three orders of magnitude smaller than that needed in the full chain, for a level of agreement aimed at the percent level or below.

- Photon conversion

- Charged particle energy loss by ionization

- Charged particle multiple scattering

- Electron, photon, and hadron showering

As output a series of objects, such as reconstructed hits and energy deposits are delivered. These objects are used as input for the full reconstruction and analysis package. So, the complete reconstruction package is used with the fast simulation, which allows for comparison between the fast and the full simulation.

5.2   Event Reconstruction

The raw data, now coming from the simulation, has to be reconstructed to the physics quantities. In the following, some information about the reconstruction methods will be given. Several steps seperate the signal in the detector and the reconstructed particles.

First, there is the local reconstruction in individual detector modules. The information contained in these modules, for instance energy deposition and positions of particles, is used to construct so-called RecHits. After that, the global reconstruction algorithms combine the RecHits from a single detector module with the RecHits from other modules of the same subdetector. Thus, objects are constructed which represent the best measurement from that subdetector. Finally, the objects created in the previous step are combined to obtain objects based on the complete detector. The objects thus obtained are called combined reconstruction-high level objects.

5.2.1   Local reconstruction

The reconstruction itself relies on the specific subdetector. Therefore, in the following, some explanation is given for the reconstruction of particle information in the subdetectors.

- In the tracker detectors, the strips or pixels with a signal exceeding a threshold are selected to be used as seeds for the clusters. Neighbouring strips or pixels are added to build up these clusters.

- Muon drift chambers give after the local reconstruction, the position of a muon.

- Muon cathode strip chambers provide position and time of arrival of a muon hit.

- In the muon resistive plate chambers, the local reconstruction provide the position of a muon hit.

- In the ECAL, the position, time of arrival and energy of electromagnetic energy depositions is given.

- In the HCAL, likewise as in the ECAL, the postion, time of arrival and energy of hadronic energy depositions is given.

5.2.2 Global reconstruction

The global reconstruction in the tracker detectors is strongly depended of the use case. Therefore, different reconstruction units are permitted to run in parallel. Thus, several different tracking algorithms are possible.

Clusters in the two calorimeters are matched to each other to produce a projective tower in the calorimetry system. These towers are used for jet reconstruction as they have a definite position in the (η, ϕ) plane.

The global reconstruction in the muon system uses the track hits and segments from the previous step. The reconstruction algorithm reconstructs the possible muon trajectories, after which a χ^2 cut is applied to reject hits unlikely to be associated with the track.

5.2.3 Combined reconstruction-high level objects

Photon and electron selection proceeds in several steps. To differentiate between the electrons and the photons, clusters in the ECAL are matched with hits in the pixel detectors. If there is a match the particle is identified as an electron, if not, the particle is a photon. To select the electrons, full track reconstruction is used, based on the seeds from the pixel hits used by the matching. Photons are selected by isolation cuts.

Muons are identified with the global muon reconstruction algorithms after which silicon tracker hits are added.

Many reconstruction algorithms exist for the reconstruction of the jets arising from the hadronization of a scattered parton or from another origin. Most algorithms are based on a clustering technique, in which calorimetric towers close in (η, ϕ) to a high transverse energy tower are summed together.

Missing transverse energy is reconstructed by summing up transverse energy vector of all calorimeter towers. By the construction of the CMS detector a large effort has been made to have a design that provides an as complete η coverage as possible to allow for the needed measurement accuracy.

The previous description of the reconstruction methods has been independent of the signal that will be used. Therefore, in the next subsection, some more information will be given about the reconstruction algorithms in single leptonic $t\bar{t}$ events as well as about the calibration of jets and b-tagging.

5.3 Reconstruction tools

Reconstruction of events is one of the most important aspects of the analysis, as the result of the ability to observe (new) physics depends strongly on the reconstruction. To reconstruct the final state of the semi-leptonic (with a muon as lepton) event, an efficient b-tagging algorithm is necessary as well as a method to calibrate jets. Muon reconstruction is an other important part. A method to determine the missing transverse energy will be needed. In the following, the methods used to reconstruct the final state are described.

5.3.1 Reconstruction of jets

Jets are the most important part of the high-p_T physics at the LHC and will therefore be an important tool in the search for physics beyond the Standard Model. Thus, an accurate reconstruction and measurement of jets is required. The calorimeter towers in the ECAL and the HCAL will be used as input for several jet clustering algorithms. Those clustering algorithms are based on the treatment of towers as massless particles. In this way, the energy is given by the energy of the tower and the direction is defined by the interaction point and the center of the tower.

The jet reconstruction method used in this analysis is the ITERATIVECONEALGORITHM [41]. There are two recombination schemes for adding the constituents. In the first scheme, the energy scheme, constituents are added as four-vectors, which results in massive jets. In the second scheme, massless jets are produced by equating the jet transverse momentum to the $\sum E_T$ of the constituents. The direction of the jet is fixed as $sin\theta = \sum E_T/E$ where E is the jet energy and $E_T = p_T c$. Input objects are grouped together as an intermediate stage, whereafter the final determination of the jet quantities is done at the end of the jet finding.

The iterative cone algorithm creates a list of E_T-ordered input objects. Around the input object with the largest transverse energy a cone of size R in the (η, ϕ)-space is cast. With the objects inside this cone the "proto-jet" direction and energy is calculated with the second scheme described above. The obtained direction is used to seed a new proto-jet. This procedure is repeated until the direction changes by $\Delta R < 0.01$ between succesive iterations and the energy of the proto-jet changes by less than 1%. If this is the case, a stable proto-jet has been found. All objects in the proto-jet are removed from the list of input objects and the procedure is repeated until the list contains no input objects with an E_T above the seed threshold. This seed threshold as well as the cone size are parameters of the algorithm. Final jet kinematic properties may be defined by applying a different recombination scheme to the jet constituents. In this analysis, the cone size R is taken to be 0.5, which means that

$$\Delta R = \sqrt{\Delta\eta^2 + \Delta\phi^2}$$

between the jet direction and the input objects should be less than 0.5.

After the reconstruction of the jet, jet calibration takes place. Firstly, a reconstructed jet is corrected to the particle-level and secondly the particle-level jet is corrected to the parton-level, which depends on the parton level assumed in the analysis. In the particle-level step, the calibration is done by correcting the energy of the reconstructed jet so that it is equal to the energy of the particles in the jet from the hard scatter. These particles were independently clustered by the same algorithm applied to reconstruct the jet. After the clustering, the particles are matched to the reconstructed jet. In the second step, the energy of the corrected jet is again corrected to the energy of the parton that originated the jet [40].

Each jet algorithm and each set of parameters for this algorithm requires a derivation of the jet calibration. Jet calibration depends also on the p_T spectrum of the process. With the jet calibration, an average correction for reconstructed jets is provided.

Jet calibration of the two jets resulting from the hadronic decay of a W boson can be fine-tuned by using the W mass as a constraint [42]. An estimate was made in a selected sample of $t\bar{t} \rightarrow bW\bar{b}W \rightarrow bb q\bar{q}\mu\nu$. A b-tag probability was constructed from the combined b-tag discriminant variable. From the light quark jets in the final state, the W boson mass can be

determined. The obtained invariant W mass spectrum can be fitted with a gaussian function and the mean value can be taken as an estimate of the reconstructed W boson mass. This value should agree with the world average for M_W, which is not the case, therefore an extra calibration shift ΔC is taken into account with a value resulting in a fitted agreement with the precise world average for M_W. A value for ΔC of $-12.9 \pm 0.4\%$ is obtained. Using the W mass constraint, the uncertainty for low p_T jets will be around 3%, whereas the uncertainty in the jet energy scale without applying this constraint will be around 5%. A similar method can be used to estimate the jet energy scale of jets originating from b-quarks by using the W boson mass and the top quark mass as constraints. In Figure 5.1 the transverse momentum of the generated (with the Monte-Carlo simulation), the reconstructed and the calibrated jets is compared for the jets resulting from a Z' boson with a mass of 1000 GeV/c^2. The generated and the calibrated transverse momentum are not entirely the same. For the two jets resulting from the hadronic decay of the W boson, this is because the p-jet can be chosen as q-jet after the reconstruction and vice versa.

5.3.2   Reconstruction of primary vertex

Another important aspect is the association of the jets with the signal vertex. Reconstructed charged tracks can be associated to primary vertices and to jets if a significant fraction of the tracks in the jet should originate from the primary vertex. For this, the reconstruction of the primary vertex will be essential.

The reconstructions of the vertex involves usually two steps, vertex finding and vertex fitting. Vertex-finding algorithms depend on the physics case. For the vertex fitting, the best estimate of the vertex parameters for a given track must be found as well as indicators of the fit quality.

There exist several vertex-fitting algorithms The Kalman filter is the most often used algorithm for vertex fitting [43]. This algorithm is mathematically equivalent to a global least-squares minimization, which is the optimal estimator for Gaussian measurements and when the fitted parameters depend linearly on those measurements.

For the primary vertex finding, two main categories are distinguished. In the first category, the primary vertex finding is based on pixel hits, which provides the High Level trigger with a primary vertex position measurement. As the High Level trigger uses this measurement subsequently for track seeding and in analyses, the algorithms must be fast and reasonably precise. Therefore, the primary vertex finding is reduced to a one dimensional search along the z-axis. The pixel hits are collected and the pixel "tracklet" parameters are evaluated. The pixel parameters are then grouped into primary vertex candidates. The second catergory is based on the information of the fully reconstructed tracks. A precise estimation of the vertex position and of the vertex position covariance matrix as well as a list of tracks associated to the primary vertex is provided.

The reconstructed jets are then associated to the reconstructed primary vertices. A jet is associated with the primary vertex if the following criteria is satisfied:

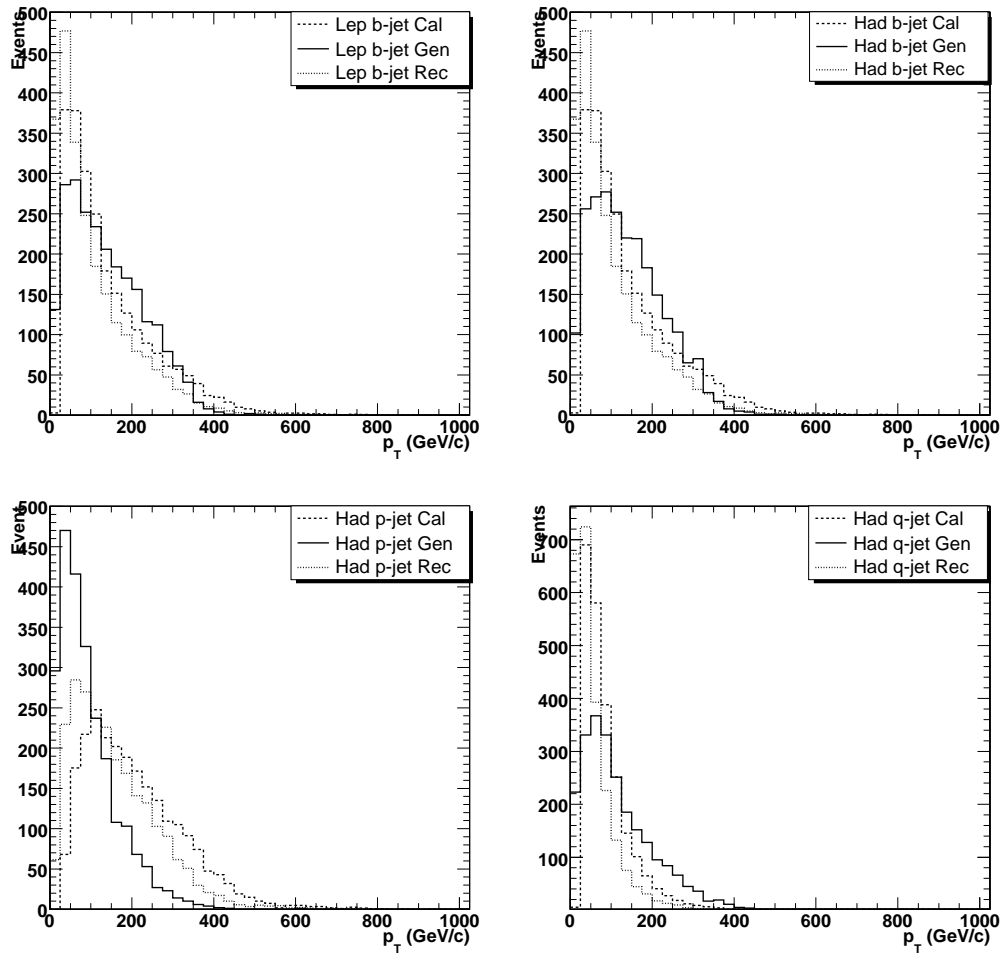$$\beta = \frac{\sum_{track,PV,jet} p_T}{\sum_{track,jet} p_T} > 0.04$$

Figure 5.1: *Transverse momentum of the generated, the reconstructed and the calibrated jets, for a Z' boson mass of 1000 GeV/c². The upper left figure shows the b-jet which originate from the same top quark as the leptonically decaying W boson, while the upper right figure shows the b-jet originating from the same top quark as the hadronically decaying W boson. The lower figures show the jets originating from the hadronically decaying W boson. From these two jets, the p-jet is always defined as the one with the highest transverse momentum.*

The sum in the nominator is over the transverse momentum of those tracks in the jets associated with the primary vertex, while the sum in de denominator is over the transverse momentum of all tracks in the jet. The low value for β reflects the aim that the tracks with the highest transverse momentum should dominate.

5.3.3 Reconstruction and identification of muons

An other important aspect of reconstructing the final state $Z' \to t\bar{t} \to b\bar{b}pq\mu\nu$ is the reconstruction of the muon.

The software for muon reconstruction has been designed to allow its use in the offline

reconstruction and the High Level trigger or online event selection. This concept, usually called regional reconstruction, requires only small parts of the detector to be reconstructed. Offline reconstruction is performed in three steps: local reconstruction of local-pattern recognition, standalone reconstruction and global reconstruction. For the second step only information from the muon system is used. The global reconstruction uses also silicon tracker hits. In the High Level trigger, the standalone and global reconstruction are respectively called Level 2 and Level 3 reconstrution.

For the standalone reconstruction, only data from the muon detectors: the drift tubes, the cathode strip chambers and the resistive parallel plate chambers is used. First the reconstruction track segments from the muon chambers obtained by the local reconstruction are used. To seed the muon trajectories, the state vectors associated with the innermost chambers are utilized. The Kalman filter technique [48] is applied while working from inside out. After the outermost detector surface of the muon system is reached, the procedure is repeated from outside in and the track parameters are defined at the innermost station. The track is extrapolated to the nominal interaction point and a vertex constraint fit to the track parameters is applied.

During the global reconstruction, the muon trajectories obtained with the standalone reconstruction are extended by including hits in the silicon tracker. Silicon layers compatible with the muon trajectory are determined and a region of interest within these layers is then defined. In this region of interest, seeds for the muon trajectory are built from pairs of reconstructed hits. From these seeds tracks are reconstructed inside the region of interest. The reconstruction algorithm relies on the Kalman filter technique, which consist of the following steps: trajectory building, trajectory cleaning and trajectory smoothing. The trajectory builder transforms each seed into a set of trajectories. The trajectory is then propagated to the next tracker reachable layer, and updated with compatible measurements found on that layer. The trajectory cleaner resolves all ambiguities between the multiple trajectories resulting from a single seed. In the final step, the reconstructed tracks are fitted using the hits in the muon chambers from the standalone reconstruction together with the hits in the silicon tracker. The final muon candidates are selected after a χ^2 cut to resolve possible ambiguities.

An additional complementary tool to select muon candidates is provided by the muon identification algorithm. This algorithm uses all reconstructed tracks from the silicon tracking detector to quantify a muon comptability for each. Information of other detectors not used in the reconstruction is taken into account. The algorithm is able to make use of hit information from individual layers of the muon detectors, even in cases where those hits are not associated with a reconstructed, standalone muon track. For example hits found in the inner muon detector can be matched with reconstructed silicon tracks and by examining the associated calorimeter energy deposits one is able to see if they are compatible with the hypothesis that the silicon track and the associated calorimeter energy deposits are produced by a muon.

In ORCA the algorithm used to reconstruct and identify the muon candidates is the GLOBALMUONRECONSTRUCTOR algorithm. In Figure 5.2 the transverse momentum of the generated and the reconstructed muon is shown resulting from the semi-leptonic decay of the top quark pair from the decay of a Z' boson for mass of 1000 GeV/c^2.

An important tool is a method to distinguish between the muons produced in jets and those coming from the decay of heavy objects. The muon selected by a transverse momen-
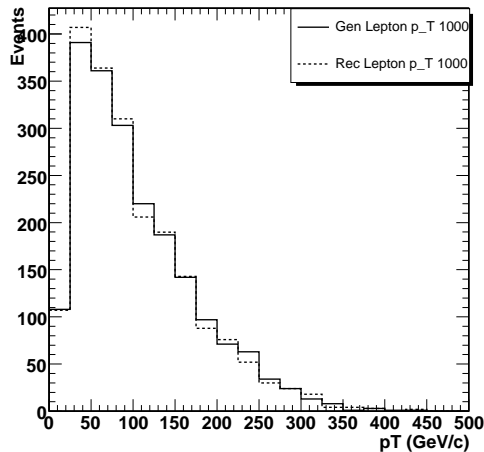
Figure 5.2: *The transverse momentum of the generated and the reconstructed muon resulting from the semileptonic $t\bar{t}$ decay into a muon.*

tum cut in the muon trigger are mostly real muons. In the momentum range relevant for triggering, the muons coming from b and c decays or K and π decays are dominant. The muons produced in these jets are accompanied by nearby particles. For a p_T above 30 GeV/c the muons coming from W and Z decays become dominant. Those muons are accompanied by particles from pile-up and by uncorrelated particles from the underlying event and should therefore be "isolated". Isolation algorithms rely on the comparison of the total energy deposited in a cone around the muon with a predefined threshold.

Another method to discriminate between leptons originating from the decay of the W boson or from the fragmentation process of the partons in semi-leptonic $t\bar{t} \rightarrow WbW\bar{b} \rightarrow b\bar{b}pq\mu\nu$ decay was investigated [47]. A likelihood ratio method was proposed based on variables which discriminate between the leptons of both categories. For muons no significant improvement was observed compared to the High Level trigger lepton isolation criteria.

5.3.4   Application of a constrained kinematic fit

To improve the resolution of the measured object in the final state of proton collisions well-defined kinematic hypothesis can be forced on the event [50]. These constraints can be applied by means of Lagrange multipliers in a general event-by-event non-linear least square fitting technique. The χ^2 can then be transformed in a probability of the proposed kinematic hypotheses to be true for the observed event. For instance the resolution of the invariant mass of top quark pairs decaying in the $WbW\bar{b} \rightarrow b\bar{b}pq\mu\nu$ final state can be improved. The invariant mass of the two-jet system $W \rightarrow pq$ resulting from the hadronically decay of the W boson can be determined as well as the invariant mass of the three-jet system resulting from the top quark decay into $t \rightarrow Wb \rightarrow pqb$. The four jets and the lepton four-momentum as well as the transverse missing energy as an estimate of the transverse component of the neutrino are used as input for the kinematic fit. The neutrino longitudinal momentum is determined from the fit. Two constraints can be applied, one on the reconstructed hadronic

W boson mass and one on the leptonic W boson mass. The W boson masses thus obtained are forced to be equal to the current world average. To reconstruct the $t\bar{t}$ mass, the top quark mass itself can be used as additional input in the fitted event hypothesis. Four constraints are then applied.

5.3.5 Algorithm for b-tagging

In the final state of many physics events b jets will be produced. Those b jets need to be distinguished from background which contains mainlylight flavoured jets. Inclusive b-tagging relies mainly upon distinct properties of b-hadrons such as a large proper lifetime ($\tau \approx 1.5$ ps), large mass, decays to final states with high charged track mulitplicities, relatively large semileptonic branching ratios and a hard fragmentation function. Algorithms for b-tagging can be applied both offline and at the level of the High Level trigger.

The b-tagging algorithms rely on the reconstruction of lower level physics objects. For instance, accurate jet reconstruction algorithms are necessary. Most of the b-hadron properties used for b-tagging are exploited using charged particle tracks because only tracking detectors offer the spatial resolution needed to detect the significant decay length of the b-hadrons. Efficient track reconstruction and precise spatial resolution close to the interaction point is the most important ingredient for almost all b-tagging algorithms. The impact parameter resolution is the most relevant for the track measurement close to the interaction point. A physics motivated lifetime-based definition of the sign of the track impact parameters is used for b-tagging. The impact parameter is considered positive if the track is reconstructed to originate downstream from the primary vertex with respect to the jet direction (in most cases taken to approximate the original flight path of the b-hadron), negative otherwise. The reconstruction of the primary vertex is essentialin many b-tagging algorithms.

The efficiency ϵ_b to tag a jet with a certain flavour as a b-jet is defined as:

$$\epsilon_b = \frac{Number - of - jets - of - flavour - q - tagged - as - b}{Number - of - jets - of - flavour - q} \tag{5.1}$$

Thus, the true flavour of a reconstructed jet must be determined. This is done by analyzing the parton content in a cone around the jet direction, where the assignment of a parton flavor to the jet follows a physics-based definition. A reconstructed jet is matched to the initial parton from the primary process (for instance in $t\bar{t}$ events the initial partons are the quarks from the top decays and the hadronic W decays) if it is within a cone of radius $\Delta R <$ 0.3.

There exist many b-tagging algorithms, but only one will be described in the following: the combined secondary vertex tag. This b-tagging algorithm is based on the reconstruction of the secondary vertex of the weakly decaying b-hadron. A discriminating variable is being formulated based on different topological and kinematic vertex variables together with track impact parameter significances. Using this variable it is possible to distinguish between jets originating from b-quarks and other jets [51].

Secondary vertices are reconstructed in an inclusive way inside the jet using the Trimmed Kalman Vertex Finder [45]. The algorithm uses the presence of a secondary vertex and topological and kinematical variables related to the vertex. The decay vertex should be reconstructed as complete as possible in order to increase the discriminating power of these

topological and kinematic variables. To select secondary vertex candidates coming from b-hadron decays cuts are applied on the vertices.

For instance, the following variables may enter into the combination for the discriminator:

- The invariant mass of charged particles associated to the secondary vertex.

- The multiplicity of charged particles associated to the secondary vertex.

- The distance from the primary vertex to the secondary vertex in the transverse plane divided by its error.

- The energy of charged particles associated to the secondary vertex divided by the energy of all charged particles associated to the jet.

- The rapidities of charged particle tracks associated to the secondary vertex with respect to the jet direction. This variable enters for n tracks, where n is the secondary vertex multiplicity.

- The track impact parameter significances in the transverse plane.

- The track impact parameter significance of the first track exceeding the charm threshold as described above.

By using a likelihood ratio technique, the variables described above can be combined into a single discriminating variable. With the quantities

$$\mathcal{L}^{b,c,q} = f^{b,c,q}(\alpha) \times \prod_i f^{b,c,q}_\alpha(x_i) \tag{5.2}$$

the variable d is defined as:

$$d = f_{BG}(c) \times \frac{\mathcal{L}^b}{\mathcal{L}^b + \mathcal{L}^c} + f_{BG}(q) \times \frac{\mathcal{L}^b}{\mathcal{L}^b + \mathcal{L}^q} \tag{5.3}$$

where α denotes the vertex category (as different vertex categories can be defined after the application of the selection cuts on the secondary vertex candidates), x_i are the individual variables, q stands for u,d,s-quark jets and gluon jets, $f_{BG}(c, q)$ is the expected prior for the c- and q-content in non-b jets ($f_{BG}(c) + f_{BG}(q) = 1$), $f^{b,c,q}(\alpha)$ is the probability for flavour b,c and q to fall into the category α and $f^{b,c,q}_\alpha(x_i)$ is the probability density function for variable x_i for category α and flavour b,c,q. The quantity d is then used as final discriminator.

The b-tag discriminator is shown in Figure 5.3. Although the discriminator in this figure is not entirely the same as this in the previous section, it is constructed according to the same principle. From this discriminator, a probability to tag b-jets is constructed. The selection cuts in the next section are motivated with this probability.
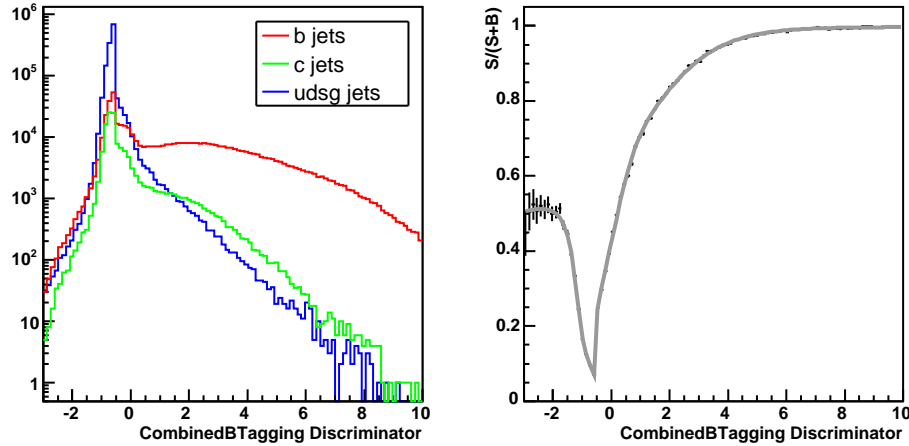
Figure 5.3: *Distribution of the combined b-tagging discriminator for jets in semi-leptonic $t\bar{t}$ events originating from different flavoured quarks (left). On the right the probability to tag a jet as a b-jet as a function of the combined b-tagging discriminator.*

5.4   Event selection

Selection criteria are an important means to reduce background events and select the signal. In this section the selection criteria and the motivation for the cuts resulting from these criteria are described.

The following selection criteria are applied:

- First of all, trigger criteria are applied. An isolated muon with a transverse momentum exceeding 19 GeV/c must be present in the range of the detector with $|\eta| < 2.4.$.

- At least four jets which match the primary vertex, must have a transverse momentum exceeding 30 GeV/c with a pseudo-rapidity $|\eta| < 2.4$.

- The transverse momentum of the isolated muon must exceed 20 GeV/c an must be found in a range with a pseudo-rapidity $|\eta| < 2.4$.

- Two of the four jets with a p_T higher than 30 GeV/c must be tagged as b-jets (therefore the value of the discriminator must exceed 0.6).

The motivation and description of the trigger is described in chapter 3. The trigger is designed to reduce background. In Tables 5.1 and 5.2 the different selection criteria are given with the number of events after applying these criteria. From this table it is clear that a fundamental background rejection comes from the trigger selection, but this will not be enough to extract the signal. Therefore, other selection criteria are applied.

The criterium for the transverse momentum of the jets is motivated by Figure 5.4. From this figure it can be seen that a better cut can be applied by asking for jets with a higher transverse momentum as the background will be relatively more reduced than the signal.

Selection	$m_{Z'} = 0.75$ TeV	$m_{Z'} = 1$ TeV	$m_{Z'} = 1.5$ TeV	$m_{Z'} = 2$ TeV
Before selection	15609 (100%)	5662(100%)	1178 (100%)	311 (100%)
Trigger + pre-selection	6098 (39%)	2305 (40%)	439 (37%)	111 (36%)
Jets $p_T > 30$ GeV/c	5307 (34%)	2036 (36%)	379 (32%)	98 (32%)
Muon $p_T > 20$ Gev/c	5183 (33%)	1987 (35%)	369 (31%)	98 (32%)
b-tag criteria	2016 (13%)	756 (13%)	121 (10%)	34 (11%)

Table 5.1: *Result of the selection criteria applied on the signal events for (30 fb^{-1}).*

Selection	$t\bar{t}$ background
Before selection	218 10^4 (100%)
Trigger + pre-selection	553690 (25%)
Jets $p_T > 30$ GeV/c	424170 (19%)
Muon $p_T > 20$ Gev/c	410130 (19%)
b-tag criteria	168076 (8%)

Table 5.2: *Result of the selection criteria applied on the background events.*

The cut on the transverse momentum of the muon is motivated by the fact that a muon with a high p_T is expected from the decay of the W boson. In Figure 5.5 the transverse momentum of the muon is shown for the signal and background events.

From this figure it can be seen that it could be advantageous to apply a higher cut on the transverse momentum. By asking for instance for a muon with a transverse momentum exceeding 30 GeV/c, the background is almost completely eliminated, but applying this cut has also an enormous reduction of the number of $Z' \to t\bar{t}$ events as a consequence. This can be seen from Table 5.3.

Selection	$m_{Z'}$=0.75TeV	$m_{Z'}$=1TeV	$m_{Z'}$=1.5TeV	$m_{Z'}$=2TeV	$t\bar{t}$ background
Previous cuts	5307 (34%)	2036 (36%)	379(32%)	98(32%)	424170 (19%)
Muon $p_T > 30$ GeV/c	1753 (11%)	693 (12%)	109 (9%)	30 (9%)	10110 (0.04%)

Table 5.3: *Number of events before and after applying a more severe cut on the transverse momentum of the muon.*

The b-tag criterium is motivated with Figure 5.3 in the previous section.

If these criteria are applied, the background is reduced by 92%. For the signal $Z' \to t\bar{t} \to b\bar{b}pq\mu\nu$ around 12% of the events are selected.

By applying these selection criteria, the contribution of the W + jets background is almost completely suppressed [42].

From Tables 5.1 and 5.2 it is clear that the background is relatively more reduced than
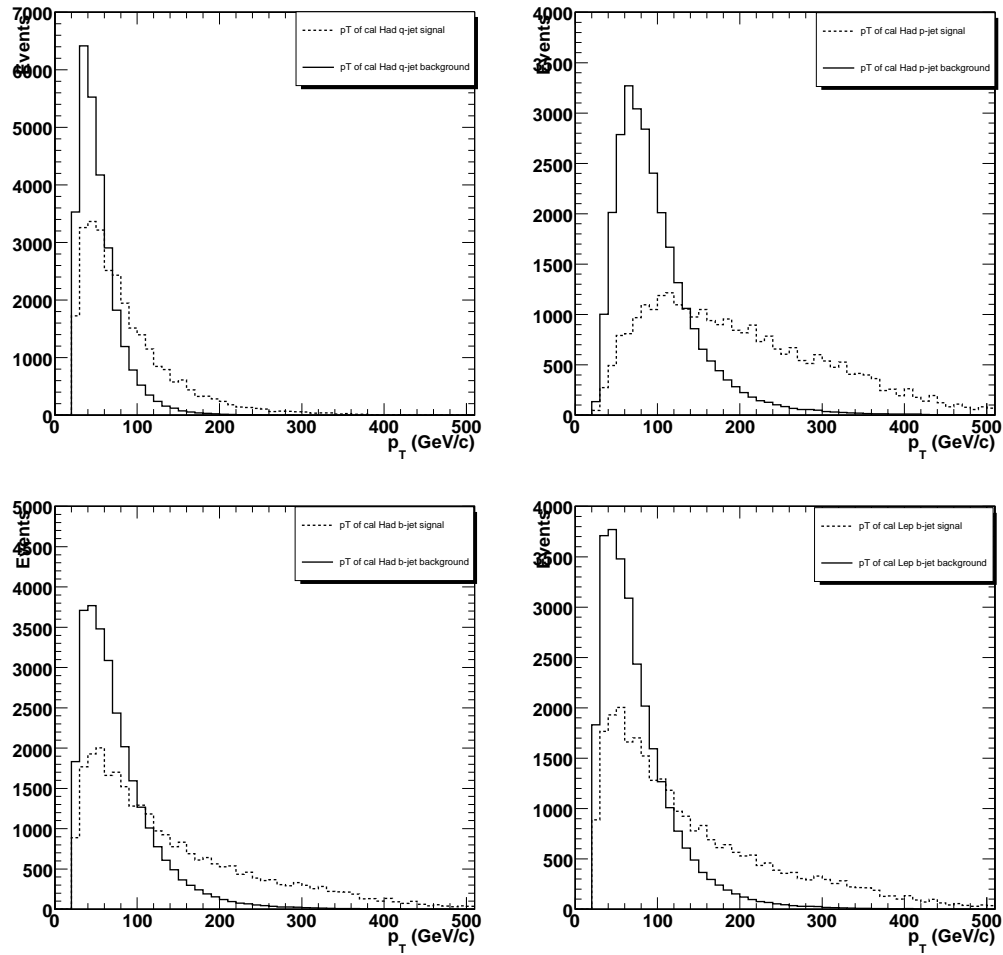
Figure 5.4: *Transverse momentum of the jets for a Z' boson mass of 1000 GeV/c^2 and for the jets resulting from the non-resonant $t\bar{t}$ background.*

the signal events. The biggest reduction comes from the pre-selection and the trigger as well as from the b-tag criterium and the transverse momentum of the jets. The criterium on the transverse momentum of the muon reduces signal and background by $\approx$ 1% but reduces QCD background very significantly.

For the remaining events, a reconstruction of the $t\bar{t}$ mass spectrum is made. For the signal events, this reconstruction is the reconstruction of the Z' boson mass, as the Z' boson decays into a top quark pair.

5.5 Reconstruction of the $t\bar{t}$ mass spectrum

In this section the method used to reconstruct the $t\bar{t}$ mass spectrum will be described. With the calibrated jets there are twelve possible combinations of the jets for reconstructing the $t\bar{t}$ invariant mass. One of the twelve combinations is choosen, but if the reconstruction is
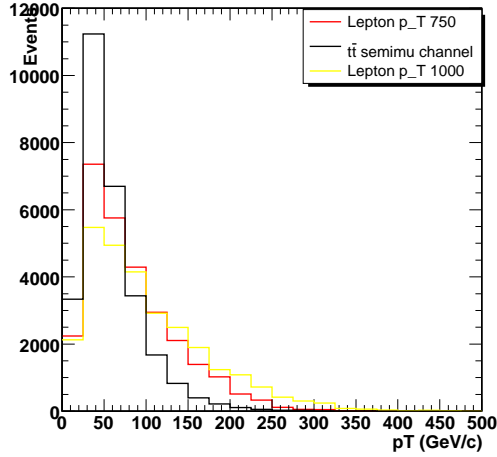
Figure 5.5: *The transverse momentum of the reconstructed muon for a Z' boson mass of 750 and 1000 GeV/c² and the background.*

done with the calibrated information, it is not important which solution is choosen as all possible combinations will result in the same reconstructed $t\bar{t}$ mass. If a kinematical fit is applied on the calibrated information it is important to choose the best solution out of the twelve combinations. If this fit converge, the best solution is choosen as the one with the smallest angle between the calibrated muon and the calibrated b-jet from the leptonic top quark decay [53]. The $t\bar{t}$ mass spectrum is reconstructed with the following formula:

$$m_{t\bar{t}} = \sqrt{\left(\sum_{i=1}^{6} E_i\right)^2 - \left(\sum_{i=1}^{6} p_{x,i}\right)^2 - \left(\sum_{i=1}^{6} p_{y,i}\right)^2 - \left(\sum_{i=1}^{6} p_{z,i}\right)^2} \qquad (5.4)$$

where the sum runs over the 6 calibrated objects: the 4 jets, the muon and the neutrino. For the neutrino $E_{T,\nu}$ is calculated as the missing transverse energy:

$$E_{T,\nu} = -\sum_{i=1}^{5} E_{T,i} \qquad (5.5)$$

As the mass of the neutrino is taken 0, the transverse momentum is equal to the transverse energy. The z-component of the momentum $p_{z,\nu}$ is calculated from the mass of the W boson:

$$m_W = \sqrt{(E_l + E_\nu)^2 - (p_{x,l} + p_{x,\nu})^2 - (p_{y,l} + p_{y,\nu})^2 - (p_{z,l} + p_{z,\nu})^2} \qquad (5.6)$$

In this analysis, because of the very low statistics and the relatively low reconstruction efficiency, the kinematical fit is not used. On Figure 5.6 the reconstruction of the $t\bar{t}$ mass spectrum based on the calibrated objects is shown as well as the reconstruction using the fitted objects. In Table 5.4 the effect of applying the fit on the mean and the RMS is shown. After applying the constraints of the kinematical fit, the number of events for the masses below 1 TeV is 81%, for masses higher than 1 Tev the convergence rate decreases to about 60%.
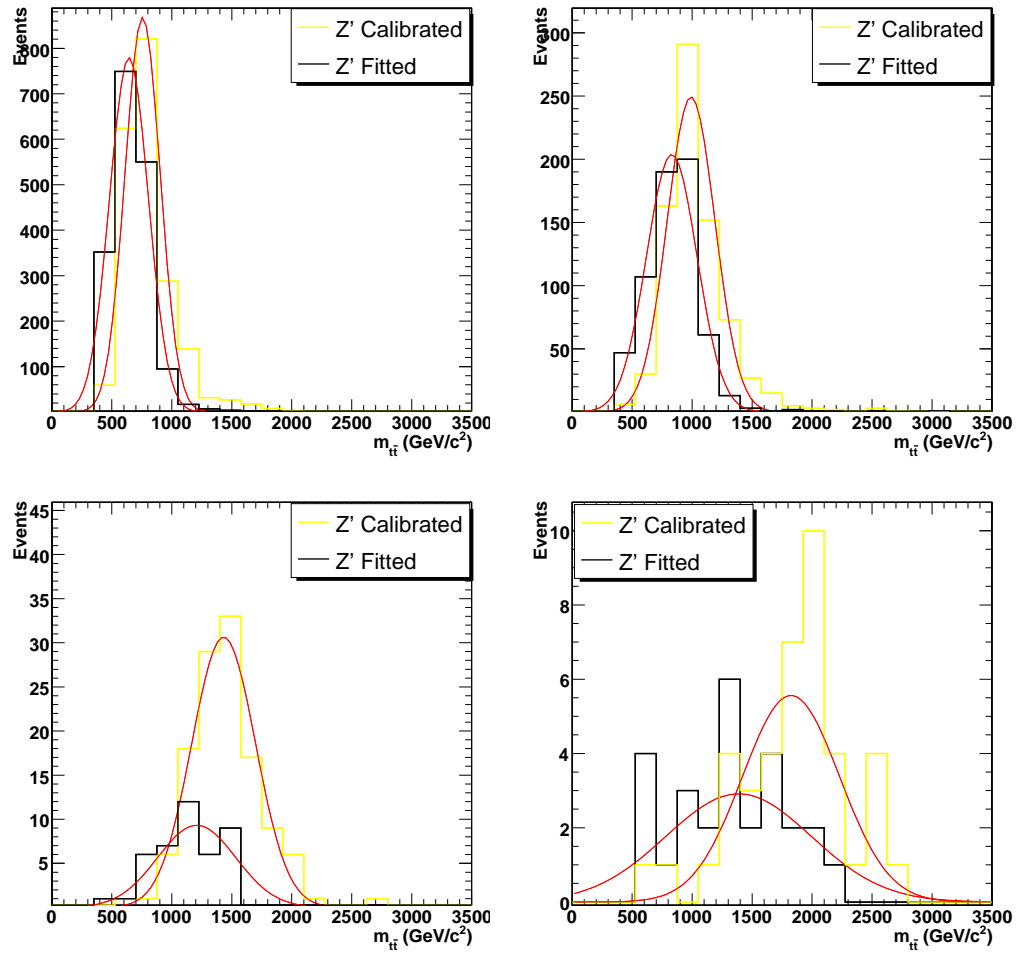
Figure 5.6: *Gaussian fit applied on the calibrated and fitted events for a Z' boson mass of 750, 1000, 1500 and 2000 GeV/c².*

		$m_{Z'} = 0.75$ TeV	$m_{Z'} = 1$ TeV	$m_{Z'} = 1.5$ TeV	$m_{Z'} = 2$ TeV
Fitted objects	mean	643	830	1207	1387
	width	162	211	326	607
Calibrated objects	mean	756	991	1432	1824
	width	146	200	266	406

Table 5.4: *Result of applying a gaussian fit to the fitted and calibrated objects, the values are given in GeV.*

The $t\bar{t}$ invariant mass of the generated and the calibrated information are compared in Figure 5.7. As can be seen from this figure, the $t\bar{t}$ mass spectrum reconstructed with the calibrated and the generated information are very similar.
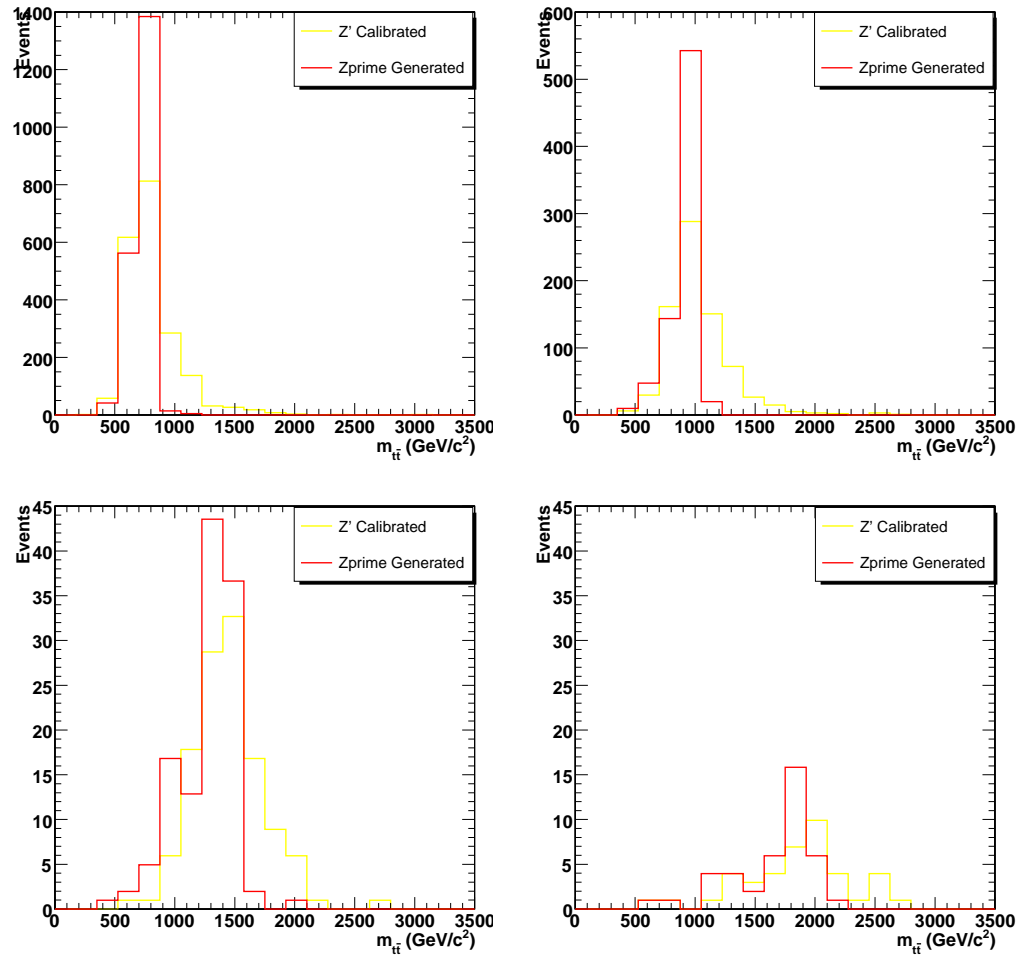
Figure 5.7: *The $t\bar{t}$ invariant mass of the generated and the calibrated information for a Z' boson mass of 750, 1000, 1500 and 2000 GeV/c^2.*

Chapter 6

Observability of the $Z' \rightarrow t\bar{t}$ excess

There exist several methods to quantify the significance of signal events. In this chapter, two methods are used to obtain the significance of the signal and are compared. Model-independent lower limits on the cross section times the branching ratio for the discovery of resonances decaying to a top quark pair are obtained with both methods for four different hypothesized masses. The significance and the model-independent limits are calculated using 2 fb^{-1} of generated data and using a cross section 15 times higher than the cross section of the Z' boson as obtained with PYTHIA. Thus, the significance calculated in the next sections is not the significance for the Z' boson signal events, but for a hypothesized resonance X with a higher cross section. However, the model-independent limits calculated in the last section give an indication for the observability of the $Z' \rightarrow t\bar{t}$ excess.

The significance S of an observed signal is the number of standard deviations the observed signal is above the expected background fluctuations. To claim the observation of a signal, the agreement is that the value of S should exceed five.

6.1 Significance of signal events using a fitting procedure

In this section, the significance of the signal events is obtained using a fitting procedure [54]. The number of signal events N_S is taken to follow a gaussian distribution, whereas the number of background events N_B is taken to follow an exponential distribution. The observed distribution of invariant masses with known normalised signal and background distribution f_s and f_b may be described as:

$$f(p_1^s, ...p_n^s, p_1^b, ...p_m^b) = N_S f_s(p_1^s, ...p_n^s) + N_B f_b(p_1^b, ...p_m^b)$$ (6.1)

where p_i^s and p_i^b are the parameters of the signal and background distributions. The significance is then defined as follows:

$$S = \frac{N_S}{\Delta N_S}$$ (6.2)

The resolution of the reconstructed $Z' \rightarrow t\bar{t}$ mass is determined by fitting the spectrum with a gaussian function, hence in Equation 6.1 $f_s = f_s(m_X, \sigma_X)$. To eliminate one parameter in the fit the resolution σ_X was taken from simulation. It is however found that the resolution depends on the mass m_X. The results of these fits are shown in Figure 6.1.
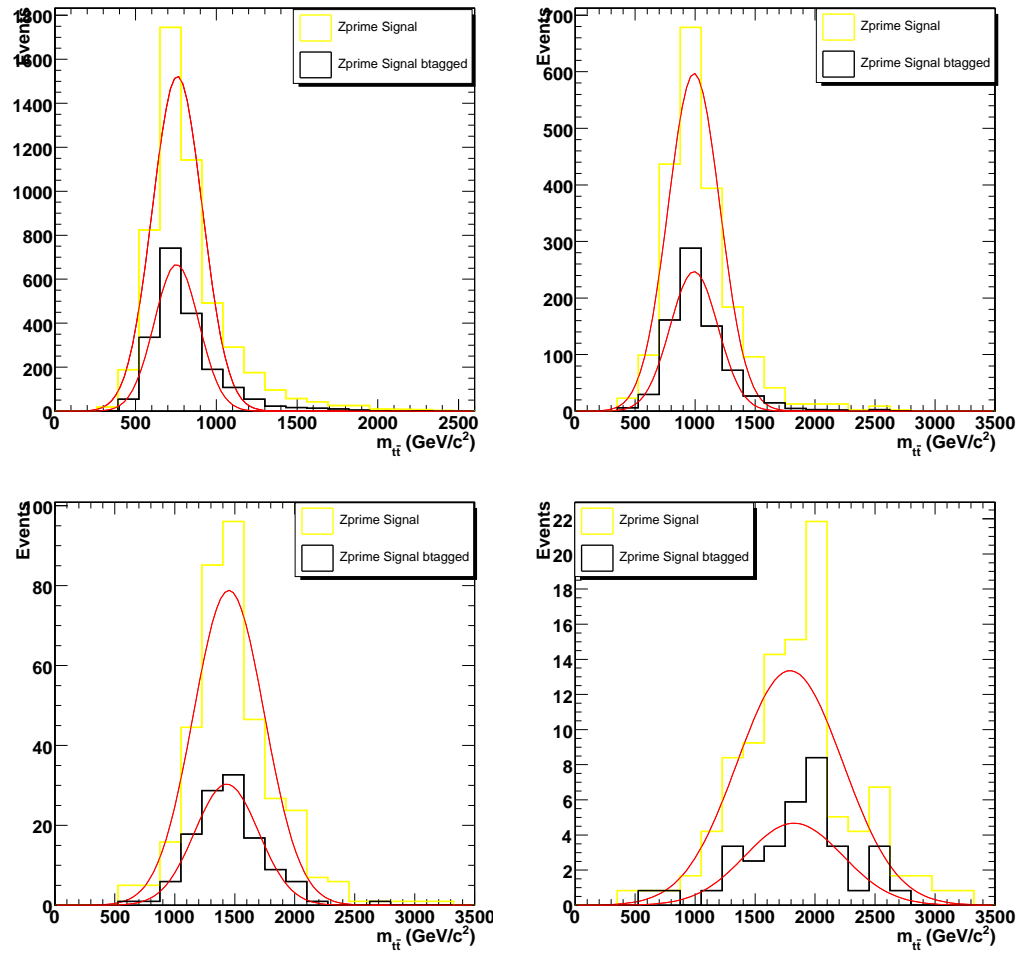
Figure 6.1: *Gaussian fit applied on the $t\bar{t}$ mass spectrum before and after the application of the b-tagging criteria for Z' masses of 750, 1000, 1500 and 2000 GeV/c².*

It should be noted that due to the low statistics, the spectra in Figure 6.1 are made with the events with and without asking for the b-tagging criteria. The $t\bar{t}$ mass spectrum is not too much affected by the b-tagging criteria, which can be seen from the same figure. In Table 6.1 the parameters of the gaussian fit of the $Z' \rightarrow t\bar{t}$ are given. Both parameters of the fit, expectation value and the resolution or variance, remain about invariant when applying the b-tag criteria. This is because the b-tag discriminator is independent from the energy and thus from the mass. The bias on the expectation values in Table 6.1 is for instance for the 2 TeV resonance about 0.2 ± 0.08, which results in 2.5 standard deviations from zero. An optimal bias should be compatible with 0. As the bias is not exceeding 5 standard deviations anytime, it is considered neglible. However it is possible to take the bias into account, but more data needs to be analyzed to reduce the uncertainty on the bias. From the results in Table 6.1 it is clear that the gaussian approximation can be used even for low statistics. In the following the b-tagging criteria are applied, but the gaussian width obtained with the events without b-tagging are used in the fit function.

		$m_{Z'} = 0.75$ TeV	$m_{Z'} = 1$ TeV	$m_{Z'} = 1.5$ TeV	$m_{Z'} = 2$ TeV
With b-tag	mean (GeV)	753.7 ± 4.1	991.0 ± 8.7	1432.1 ± 26.7	1824.2 ± 81.9
	width (GeV)	138.2 ± 2.9	199.6 ± 7.7	266.2 ± 21.9	405.8 ± 120.8
Without b-tag	mean (GeV)	758.9 ± 2.8	991.1 ± 5.9	1451.0 ± 18.7	1791.0 ± 46.9
	width (GeV)	154.6 ± 2.3	216.0 ± 4.8	296.2 ± 19.3	442.2 ± 49.1

Table 6.1: *Results of applying a gaussian fit to the signal events before and after b-tagging.*

The resolution σ_X obtained with the events without b-tagging is shown in Figure 6.2 as a function of the mass. It is clear that there is a relation between the width and the mass. The slope of the straight line is 0.226 ± 0.016. Thus, in the expression of the total distribution, Equation 6.1, one parameter is fixed.
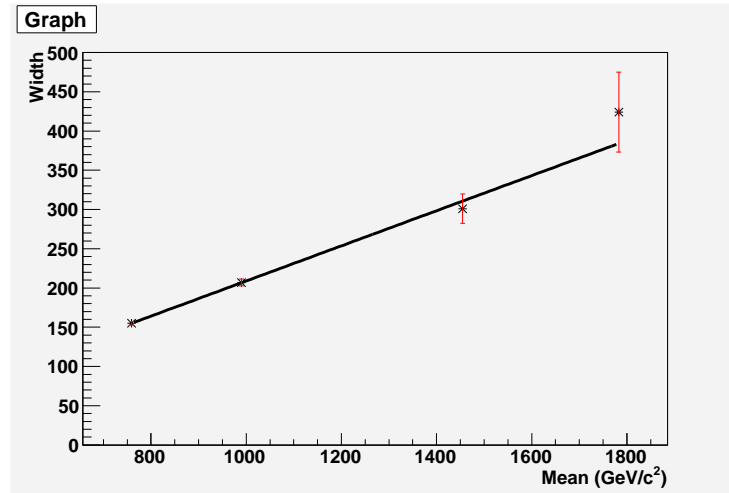

Figure 6.2: *Relation between the mean and the width from the gaussian fit before applying the b-tag criteria for the different masses of the Z' boson.*

Also the background shape is estimated from simulation eliminating another parameter in the fit. The background $pp \to t\bar{t}$ is fitted with an exponential function, $f_b = e^{p_1^b x}$. The result is shown in Figure 6.3. To make this fit possible, the $t\bar{t}$ invariant mass spectrum is considered for values higher than 600 GeV/c^2. As can be seen from Figure 6.4 the exponential approximation breaks down for masses of about 550 GeV/c^2. But the Tevatron has excluded the existence of $X \to t\bar{t}$ resonances up to 725 GeV/c^2, hence in this analysis no effort is made to go to lower mass values.

The slope of the exponential fit is $p_1^b = $ -0.0048 $\pm$ 0.0007. This value for the parameter will be used in Equation 6.1. In the original expression for the fit function, there are five unknown parameters: the number of signal events N_S, the expectation value of the gaussian function m_X, the width of the gaussian function σ_X, the number of background events N_B and the slope of the exponantial function p_1^b. Two out of these five parameters can be expressed as a function of the others. As is shown above, the width and the mean are related,
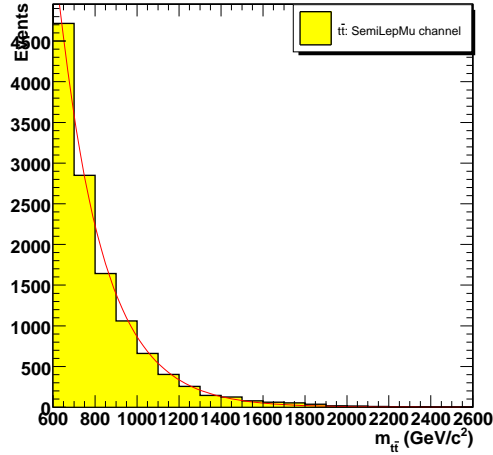
Figure 6.3: *Exponential fit applied on the distribution of the non-resonant $t\bar{t}$ background for masses higher than 600 GeV/c². *
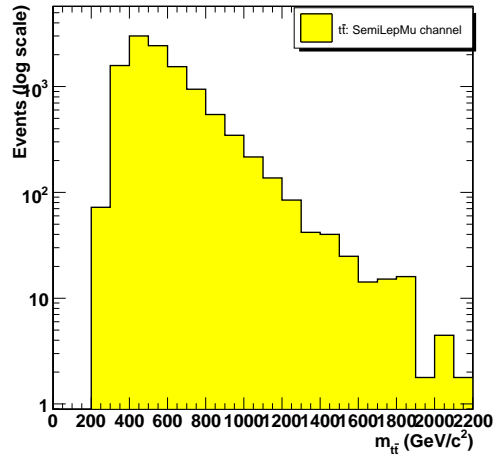

Figure 6.4: *Exponential fit applied on the distribution of the non-resonant $t\bar{t}$ background for masses higher than 600 GeV/c². *

thus a parameter is eliminated. The sum of the number of signal and background events must be equal to the total number of events in the observed mass range: $N = N_S + N_B$. The number of background events is expressed as the total number minus the number of signal events or $N_S = N - N_B$. The slope of the exponantial distribution is fixed to p_1^b = -0.0048. The mean of the gaussian distribution is also fixed, because due to low statistics it is difficult to leave this parameter free. However, this can be done because if the mass of the resonance is unknown, a scanning procedure can be applied which fits the spectrum for each hypothesized mass. For each mass, a corresponding significance is found. The highest significance among these obtained for the tested resonance masses corresponds to the most probable hypothesized mass.

It is than important that the bias is accounted for. Thus, the only parameter that is free is the number of signal events N_S. The result of applying the fit function is shown in Figure 6.5. The number of signal events and the obtained significance are given in Table 6.2. For $m_X = 750$ GeV/c^2 the value for the significance is lower than for higher masses, this is because the signal disappears in the slope of the background. For increasing masses m_X above 1 TeV the value for the significance is decreasing, because the cross section of the process and thus the number of signal events decreases.
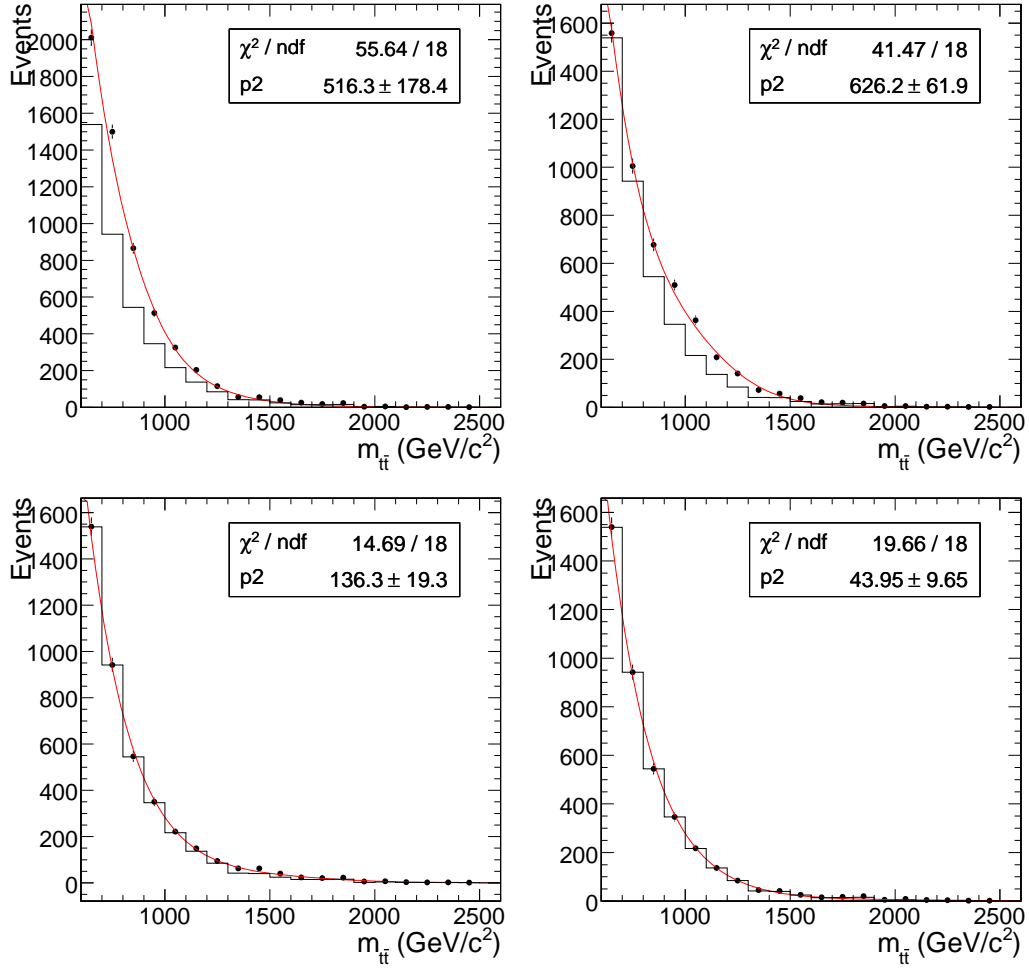

Figure 6.5: *Application of the fit to the signal+background events. The parameter p2 represents the excess of the number of signal events N_S visible above the background which has an exponantial shape. This is done for the masses of 750, 1000, 1500 and 2000 GeV/c^2 for a hypothezised resonance X with a cross section $\sigma\left(X \to t\bar{t}\right) = 15\sigma\left(pp \to Z' \to t\bar{t}\right)$ and for an integrated luminosity of 2 fb^{-1}.*

	$m_X = 0.75$ TeV	$m_X = 1$ TeV	$m_X = 1.5$ TeV	$m_X = 2$ TeV
N_S	516	627	136	44
ΔN_S	178	62	19	10
$S = N_S/\Delta N_S$	2.9	10.1	7.2	4.4

Table 6.2: *Significance of the signal events. The fit function with one free parameter N_S for several masses m_X as described in the text is applied on the reconstructed $t\bar{t}$ mass spectrum for 2 fb^{-1} of data.*

6.2 Significance of signal events using a counting procedure

In a specified signal region, the number of signal events N_S and the number of background events N_B is used to define the significance S. In this analysis and using the counting method, the significance is defined as the ratio between the number of signal events and the background fluctuation, which is assumed to be Poissonian distributed:

$$S = \frac{N_S}{\sqrt{N_B}} \tag{6.3}$$

In this analysis, the signal region is specified as the region of two times the width of the gaussian centered around the mean value for the tested mass m$_X$, hence $[m_X - 2\sigma_X, m_X + 2\sigma_X]$. The number of signal and background events and the resulting values for the significance are given in Table 6.3. The significance is decreasing because the cross section and thus the number of signal events decreases with increasing mass. Figure 6.6 shows the background and the signal events added to this background for the different masses and the mass regions of two times the width around the generated mass.

	$m_X = 0.75$ TeV	$m_X = 1$ TeV	$m_X = 1.5$ TeV	$m_X = 2$ TeV
N_S	1764	692	116	32
N_B	7438	3851	943	251
$S = N_S/\sqrt{N_B}$	20.5	11.2	3.8	2.0

Table 6.3: *Significance of the signal events. The counting procedure for several masses m$_X$ as described in the text is used on the reconstructed $t\bar{t}$ mass spectrum for 2 fb^{-1} of data.*

The significance obtained with the two different methods is shown in Figure 6.7. For masses below 1000 GeV/c^2 the counting method gives a higher significance. This is because when using the fit function, the resonance disappears in the background for lower masses than 1000 GeV/c^2. The obtained significances using the fitting procedure are better than thos obtained with the counting procedure above a mass of 1000 GeV/c^2 using 2 fb^{-1} of data for a hypothesized resonance X with a cross section fifteen times that of the Z' resonance. However, in the next section, the robustness of both methods against background fluctuations is shown. The advantage of the fitting procedure will be clear.
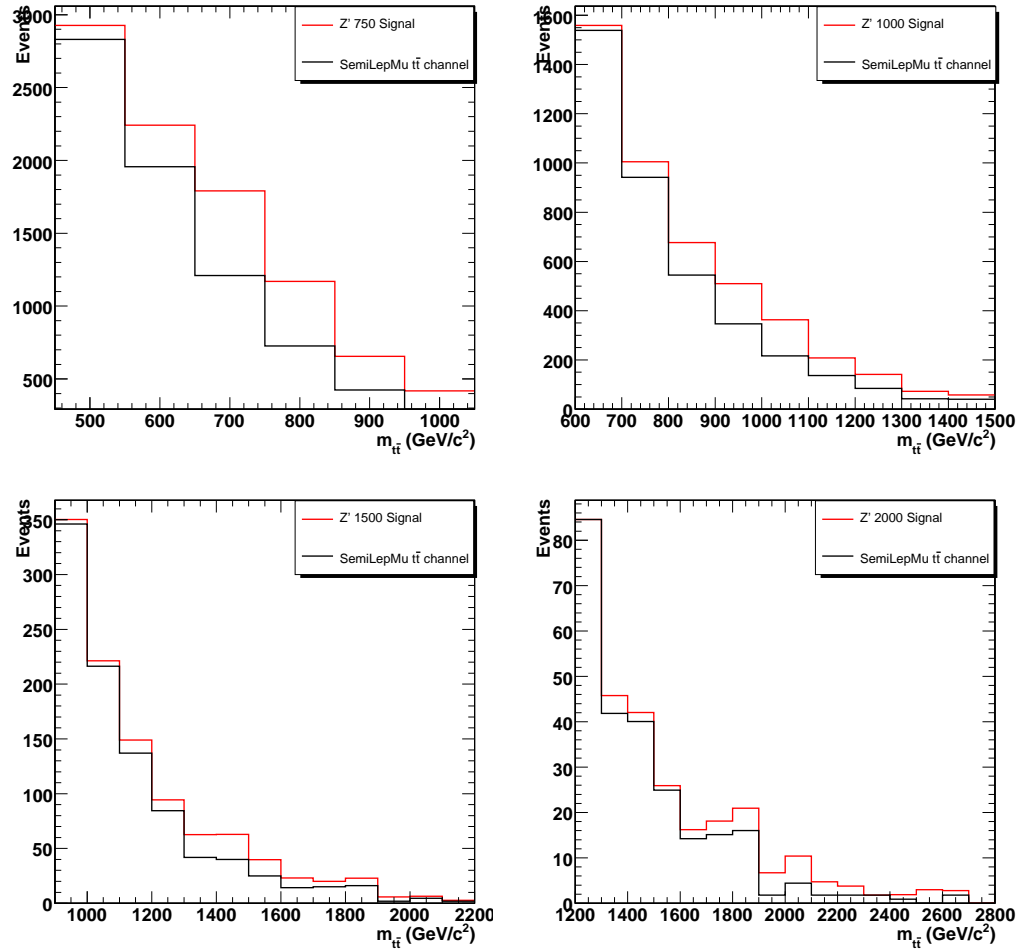
Figure 6.6: *Background and signal+background events for a mass region of two times the width around the generated masses of 750, 1000, 1500 and 2000 GeV/c². This is done for a hypothezised resonance X for the masses of 750, 1000, 1500 and 2000 GeV/c². It should be remarked that a fixed bin size is taken, which is not optimal, but makes no difference for the counting.*

6.3 Model-independent results

To obtain model-independent limits, the cross section times the branching ratio or $\sigma\left(pp \rightarrow X\right) \cdot BR\left(X \rightarrow t\bar{t}\right)$ is calculated. This cross section times branching ratio is the minimum a resonance production cross section must have to exceed the required value of five for the significance to claim a discovery. Using 2 fb^{-1} of generated data, the cross sections are calculated and given in Table 6.4. The result is shown in Figure 6.8. Resonances with a cross section times branching ratio exceeding the discovery contour can potentially be discovered. If this is not the case, a higher integrated luminosity is needed to increase the discovery potential for a $t\bar{t}$ resonance decaying semi-leptonically into a muon. It is clear that the Z' boson cross sections are to low to claim a discovery of the resonance with an integrated luminosity of 2
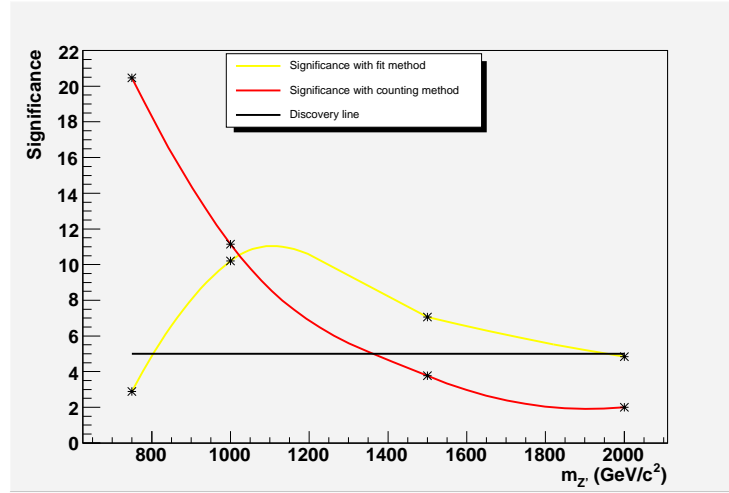
Figure 6.7: *The significances for the masses of 750, 1000, 1500, 2000 GeV/c^2 for the resonance X with a cross section $\sigma \left(X \to t\bar{t} \right) = 15\sigma \left(pp \to Z' \to t\bar{t} \right)$ as obtained with the counting procedure and the fitting procedure and using 2 fb^{-1} of data.*

fb^{-1}.

$\sigma \times BR(pb)$	$m_X = 0.75$ TeV	$m_X = 1$ TeV	$m_X = 1.5$ TeV	$m_X = 2$ TeV
Fitting method	13.50	1.39	0.42	0.16
Counting method	1.91	1.27	0.78	0.31
Z' boson	0.520	0.188	0.039	0.010

Table 6.4: *Corresponding cross sections times branching ratio needed to exceed the significance value of five, using the fitting procedure and the counting procedure, for the semileptonic decay of a resonance $X \to t\bar{t}$ in a muon for 2 fb^{-1} of data.*

The effect of including the semi-leptonic decay into an electron results in two times more data, as the selection and analysis for the electron and the muon are about the same. The result with the electron included and for an integrated luminosity of 30 fb^{-1} is shown in Figure 6.9. From this figure can be seen that even with the inclusion of the decay via the electron channel and with an integrated luminosity of 30 fb^{-1}, the Z' resonance does not exceed the required value of five for the significance.

The robustness of the analysis procedures against the systematic uncertainty of the background level is tested. A systematic shift of ϵ on the background level of 10% is included as the $pp \to t\bar{t}$ spectrum will be measured with this uncertainty at the LHC [55]. The significance obtained with the counting method is then calculated as follows:

$$S = \frac{N_S}{\sqrt{N_B + (\epsilon * N_B)^2}}$$
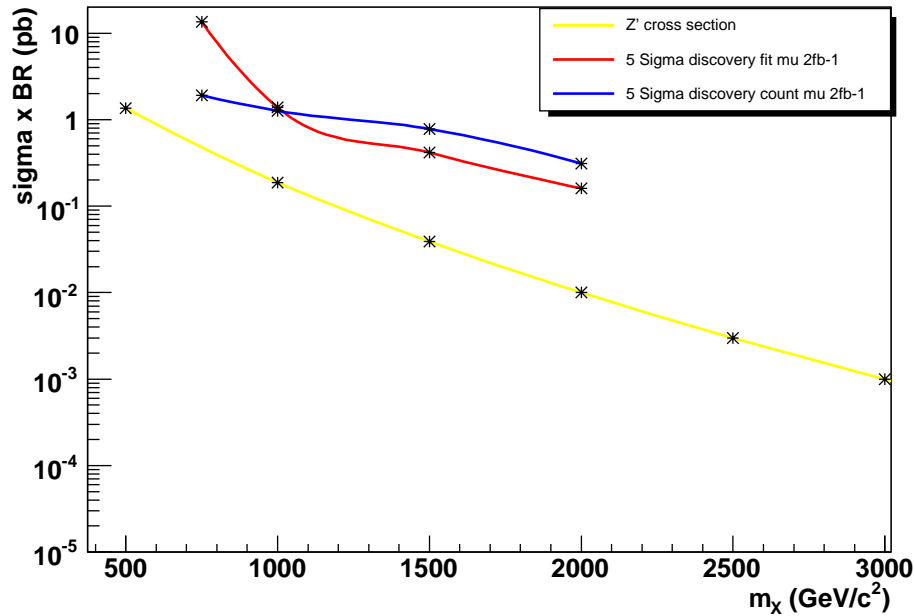
(6.4)

Figure 6.8: *Model-independent discovery contour of a resonance X decaying in a top quark pair using 2 fb^{-1} of data and considering the semi-leptonic decay into a muon. As the cross section times branching ratio of the Z' boson is below the line for the tested masses, it can not be discovered.*

In the denominator the standard deviation on the distribution is represented. The standard deviation is defined as the square root of the variance. The total variance is the sum of the variance resulting from the statistical uncertainty N_B (for a Poissonian distribution) and the variance resulting from the systematic uncertainty which is $(\epsilon * N_B)^2$.

The result of considering the background systematics is shown in Figure 6.10 for the counting procedure. It is clear that the uncertainty on the background level has have an influence which can not be neglected. In Figure 6.11 the same uncertainty is considered using the fitting procedure, the discovery region is only slightly reduced. The uncertainty was taken into account by applying the fit function on the reconstructed $t\bar{t}$ spectrum with a higher background level which is done by multiplying the background with the factor obtained with the counting procedure. On this figure it is shown that the fitting procedure is more robust against systematics on the background level.
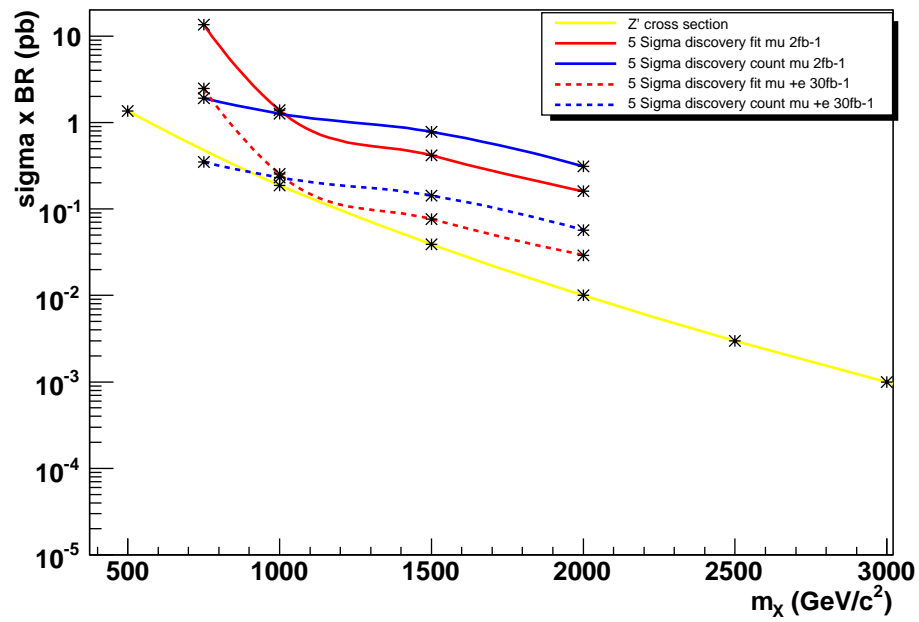
Figure 6.9: *Model-independent discovery contour of a resonance X decaying in a top quark pair using 30 fb^{-1} of data and considering two times more data, as if the electron channel is taken into account.*

Figure 6.10: *Effect on the discovery contour of a resonance X decaying in a top quark pair including background systematics as described in the text and using the counting procedure using 2 fb^{-1} of data.*
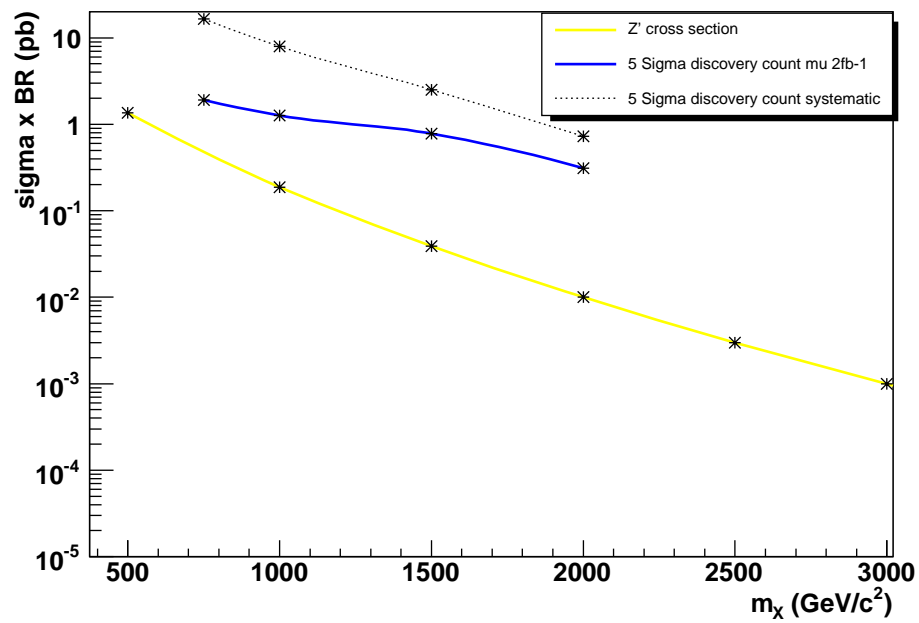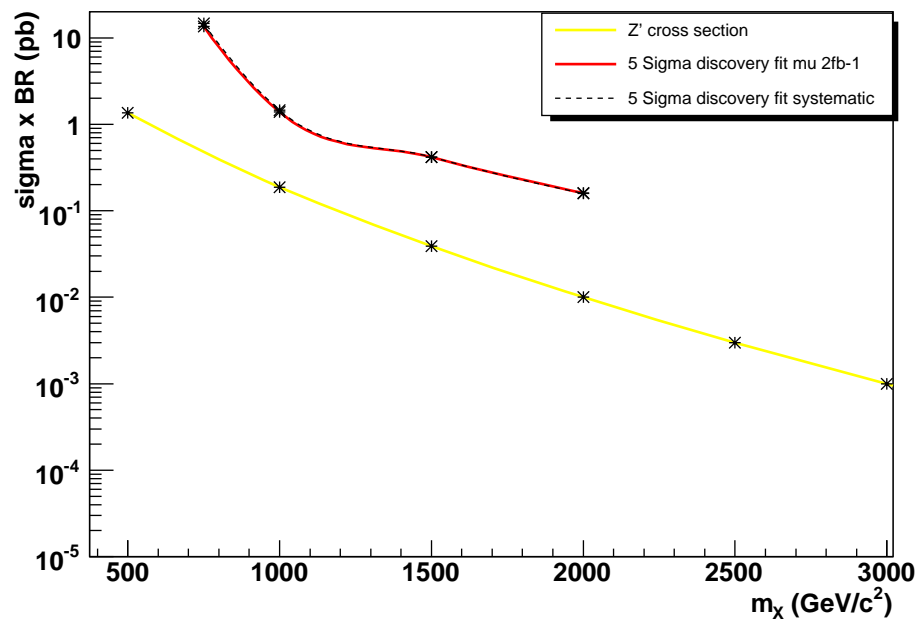
Figure 6.11: *Effect on the discovery contour of a resonance X decaying in a top quark pair including background systematics as described in the text and using the fi tting procedure using 2 fb^{-1} of data.*

Chapter 7

Conclusions

In the previous chapter, model-independent lower limits on the cross section times branching ratio were obtained for the discovery of a $t\bar{t}$ resonance. In the following section, the obtained result is compared with the lower limits of a likewise study for the ATLAS experiment. The result for the observability of the Z' boson is compared with the results of D0 and CDF at Tevatron. In the last section, possible improvements are discussed.

7.1 Conclusion and comparison with other studies

In Chapter 6 lower limits on the cross section times branching ratio for a discovery of $t\bar{t}$ resonances were obtained for masses between 750 and 2000 GeV/c^2. As these lower limits are model-independent, it is possible to apply this analysis to each $t\bar{t}$ resonance predicted by any model beyond the Standard Model. From the previous chapter it was also clear that the cross section of the Z' boson decaying into $t\bar{t}$ is too low to have a possible observation with data with an integrated luminosity of 30 fb^{-1} and inclusion of the semi-leptonic decay into an electron. More data is needed to observe the Z' boson for masses higher than 750 GeV/c^2 predicted by Topcolor-assisted Technicolor.

The event selection performed by the D0 experiment at the Tevatron Collider is done by using the following selection criteria.

- To identify b-jets a lifetime tag was used.

- There was asked for an isolated electron with a p_T exceeding 20 GeV/c and $|\eta| < 1.1$ or for an isolated muon with a p_T exceeding 20 GeV/c and $|\eta| < 2.0$.

- The missing transverse energy was required to exceed 20 GeV and not to be collinear with the lepton direction in the transverse plane.

- For the reconstruction of the jets, a cone algorithm was used which defined the jets using a radius of $\Delta R = 0.5$. Four or more jets were required with a p_T exceeding 15 GeV and $|\eta| < 2.5$.

In the kinematical fit the four jets with the highest p_T are choosen. From the twelve possible jet combinations the one with the lowest χ^2 is choosen. Assuming there is no resonance

signal, a Bayesian approach was used to calculate 95% confidence level upper limits on the cross section times branching ratio for each hypotesized mass M_X. Using 370 pb^{-1} of data the existence of a Z' boson with a mass $M_{Z'}$ below 680 GeV/c^2 and a width $\Gamma_{Z'}$ of 0.012 $M_{Z'}$ was excluded.

A likewise study performed at the CDF experiment at the Tevatron Collider used the same selection cuts with exception of the following: jets are defined using a cone algorithm with a radius of ΔR =0.4. An integrated luminosity of 680 pb^{-1} was used to exclude the existence of a Z' boson with a mass below 725 GeV/c^2.

The ATLAS experiment at the LHC performed a study of the sensitvity to a generic narrow resonance decaying to $t\bar{t}$ [55]. To select the the signal events, the following requirements are asked for:

- The missing transverse energy must exceed 20 GeV.

- An isolated electron or muon with $p_T > 20$ GeV/c and $|\eta| < 2.5$.

- Between four and ten jets with $p_T > 20$ GeV/c and $|\eta| < 3.2$.

- At least one jet tagged as b-jet.

These cuts reduce the background to a domination of continuum $t\bar{t}$ production. Reconstruction of the neutrino is done by setting its mass to zero and assigning the missing transverse energy to the transverse energy of the neutrino. The longitudinal momentum p_z of the neutrino is then calulated by requiring that the invariant mass of the lepton and the neutrino form the mass of the W boson. The W boson that decayed hadronically is reconstructed by selecting pairs of jets which were not b-tagged. The top mass was reconstructed by combining each b-jet with the possible W bosons. If only one jet was tagged as a b-jet, each of the still unassigned jets was considered as a candidate for the other b-quark.

From the possible combination of the jet-parton assignments the one was choosen which minimized:

$$\chi^2 = (M_{jjb} - m_t)^2/\sigma^2(M_{jjb}) + (M_{l\nu b} - m_t)^2/\sigma^2(M_{l\nu b}) + (M_{jj} - M_W)^2/\sigma^2(M_{jj})$$

If $M_{l\nu b}$ or M_{jjb} disagreed with the known value of m_t by more than 30 GeV/c^2, the events were rejected.

The required cross section times branching ratio for a discovery or exclusion of a narrow resonance X decaying to $t\bar{t}$ is shown in Figure 7.1. With an integrated luminosity of 30 fb^{-1} a 1 TeV resonance could be discovered if its cross section times branching ratio exceeds 830 fb and for a 2 TeV resonance 160 fb.

In Figure 7.2 the same plot is shown for the CMS experiment with the analysis described in the previous chapters. Using the fitting procedure and 30 fb^{-1} of data, a 1TeV resonance could be discovered if its cross section times branching ratio exceeds 2420 fb and for a 2TeV resonance 280 fb. It should however be noted that ATLAS performed its search using a fast simulation with parametrized detector resolutions, hence the results are not necessarily realistic.
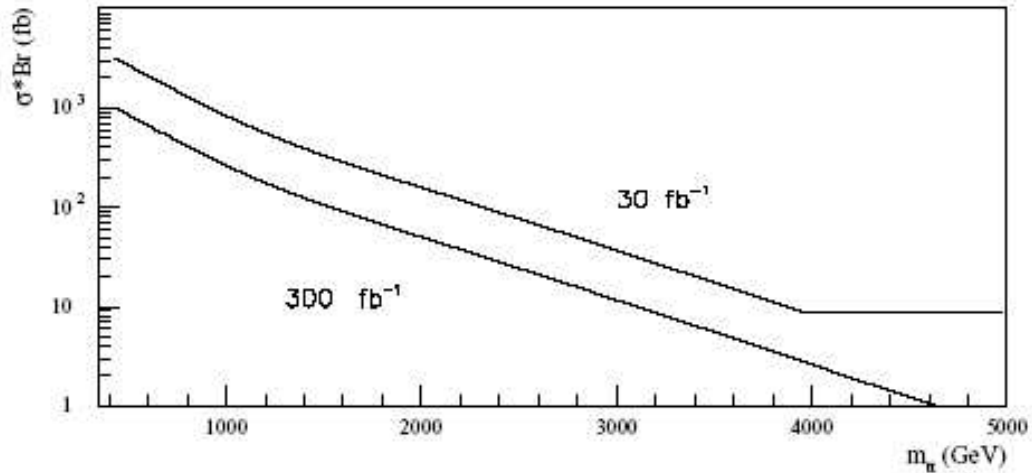
Figure 7.1: *Value of $\sigma \times BR\left(X \to t\bar{t}\right)$ required for the discovery of a narrow resonance decaying to $t\bar{t}$ as a function of M_X and for an integrated luminosity of either 30 or 300 fb−1 as obtained for ATLAS.*
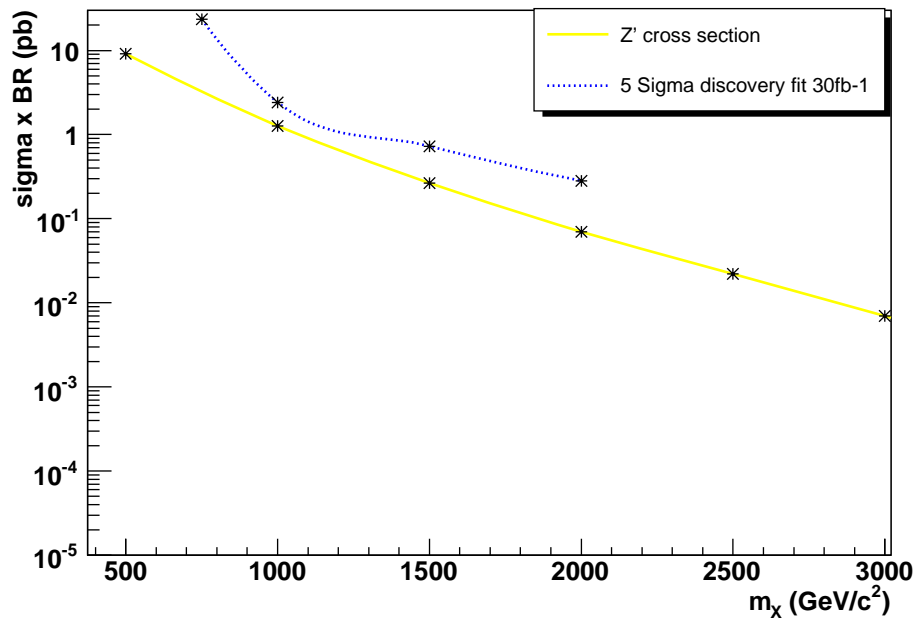

Figure 7.2: *Value of $\sigma \times BR\left(X \to t\bar{t}\right)$ required for the discovery of a narrow resonance decaying to $t\bar{t}$ as a function of M_X and for an integrated luminosity of 30 fb^{-1} as obtained for CMS using a fi tting procedure. An example of Z' production is shown.*

The obtained results in Figure 7.2 can be used to determine the sensitivity and discovery potential for models which predict a resonance with a specific natural mass, width and cross section times branching ratio.

7.2   Possible improvements

It is possible to improve the reconstruction of the jets at high energies by decreasing the cone radius from $\Delta R = 0.5$ to 0.4. In the analysis used by the CDF experiment, the jets were defined with a cone radius of 0.4. It is then possible to apply an analysis for resonances with masses higher than 2000 GeV/c^2 as more events will be selected. Decreasing the cone radius for jet reconstruction will improve the result as it was shown in chapter 4 on Figure 4.1 that the boost of the top quark for high mass resonances results in overlapping jets.

Another improvement can be done, provided that there is enough data, by applying a kinematical fit. This will improve the resolution of the resonance in the reconstruction of the invariant $t\bar{t}$ mass distribution. However, the kinematical fit itself should be revised in order to obtain a higher reconstruction efficiency so that, even with low statistics, the fit can be used.

An improvement may come from the b-tag criteria, there can be asked for two b-tagged jets and two jets that are anti-b-tagged. The selection criteria on the transverse momentum of the lepton and the jets can be made more severe by requiring a higher transverse momentum, and this can certainly be done for resonances expected with a high mass as these will result in higher p_T for the jets and the lepton.

The extrapolation of the significance to higher integrated luminosities is done by a $S \sim \sqrt{\mathcal{L}}$ law in this analysis, but this is not optimal. For non-gaussian errors the interval which corresponds to the value of five for the significance is not simply five times the interval which corresponds to the value of one for the significance. Another method must then be applied [54]. Another improvement can be done by leaving the parameter for the mean in the fit of the total distribution free, as it is normally not known at which mass the resonance will appear. However, this can only be done if there is enough data to distinguish the signal above the background.

Summary

From 2007 the Large Hadron Collider will collide protons up to energies of 14 TeV. This will allow us to explore new energy frontiers to enravel the nature of particle physics. The Compact Muon Solenoid is one of the detectors which will measure the proton collisions. One of the remaining problems of the Standard Model is the generation of particle masses. Several models are proposed to explain this feature, among them the Topcolor-assisted Technicolor model (TC2). This model predicts new particles which can decay into a pair of top quarks. In this thesis an analysis is constructed to search for the resonances in the future LHC data. By fitting the reconstructed $t\bar{t}$ invariant mass spectrum model-independent lower limits on the cross section times branching ratio, $\sigma \times BR$, of resonances decaying into top quark pairs. In a data set of an integrated luminosity of 30 fb^{-1} a generic resonant $pp \rightarrow X \rightarrow t\bar{t}$ process can be observed if its production cross section exceeds 2420 fb for m$_X$ = 1 TeV or 280 fb for m$_X$ = 2 TeV. With these limits, the discovery potential for models which predict a resonance with a specific natural mass, width and cross section times branching ratio can be determined. This was tested with the Z' boson predicted by Topcolor-assisted Technicolor. It was shown that, although improvements are possible, the Z' boson can not be discovered with 30 fb^{-1} of data in the $t\bar{t}$ decay mode.

The obtained model-independent lower limits were compared with the limits from the ATLAS experiment. In the presented study, using a full detector simulation, there is a reduction of the discovery potential compared to ATLAS where a fast simulation has been used. The possibility of the Tevatron for discovering new resonances is extended.

Improvements or extensions of this study are proposed, the analysis can be improved by searching for the optimal selection criteria to distinguish the continuum $t\bar{t}$ production from the signal events. Therefore, the reconstructed kinematics of the signal and background events must be extensively studied. Improving jet reconstruction tools is required for resonance masses exceeding 2 TeV. Other decay channels may be studied and added.

Samenvatting

Vanaf 2007 zullen protonen botsen in de Large Hadron Collider bij een massamiddelpuntsenergie van 14 TeV. Dit zal ons toelaten nieuwe grenzen te verkennen en de fysica van de elementaire deeltjes te ontsluieren. Een van de detectoren die de proton botsingen zullen waarnemen is de Compact Muon Solenoid detector. In het Standaard Model van de elementaire deeltjes is een van de onbeantwoorde vragen de generatie van de massa's van de deeltjes. Om dit probleem op te lossen werden verschillende modellen of mechanismen voorgesteld, waaronder Topcolor-assisted Technicolor (TC2). Dit model voorspelt nieuwe deeltjes die vervallen naar een paar van top quarks. In deze thesis werd een analyse opgesteld om in de toekomstige LHC data deze $t\bar{t}$ resonanties te ontdekken. Door het gereconstrueerde invariante $t\bar{t}$ massa spectrum te fitten werden model-onafhankelijke onderlimieten bekomen op de cross sectie maal vertakkingsverhouding, $\sigma \times BR$, van resonanties die vervallen in een top quark paar. Met data die overeenkomt met een geïntegreerde luminositeit van 30 fb^{-1} (3 jaar LHC) kan een resonantie $pp \rightarrow X \rightarrow t\bar{t}$ waargenomen worden als de cross sectie van dit proces groter is dan 2420 fb voor m$_X$ = 1 TeV of 280 fb voor m$_X$ = 2 TeV. Aan de hand van de bekomen limieten kan men nagaan of nieuwe modellen die deze $X \rightarrow t\bar{t}$ resonanties omvatten, ontdekt kunnen worden. Deze methode werd getest op het Z' boson dat voorspeld wordt door Topcolor-assisted Technicolor. Het was duidelijk dat, hoewel verbeteringen mogelijk zijn, dit boson niet ontdekt kan worden met een geïntegreerde lumminositeit van 30 fb^{-1} in de $t\bar{t}$ vervalmode. De LHC zal meer gegevens moeten produceren om een ontdekking mogelijk te maken.

De bekomen limieten werden vergeleken met dezelfde limieten van het ATLAS experiment. De limieten die bekomen werden in deze analyse met de volledige detectorsimulatie zijn hoger dan de limieten van het ATLAS experiment waar een snelle detectorsimulatie toegepast werd. De parameter ruimte die toegankelijk is voor de Tevatron experimenten wordt door de voorgestelde methode toegepast op de LHC data uitgebreid. Men zal hiermee het bestaan van $X \rightarrow t\bar{t}$ resonanties bij hogere massa's m_X kunnen uitsluiten.

Verbeteringen worden voorgesteld om de resonantie duidelijker te onderscheiden van de achtergrond. Daarvoor is het noodzakelijk dat de gereconstrueerde kinematica van achtergrond en signaal uitvoerig bestudeerd wordt om eventueel betere selectie criteria toe te passen. Een verbeterde jet reconstructie is nodig, zeker voor resonanties met massa's die hoger zijn dan 2 TeV. Bovendien kunnen andere vervalkanalen bestudeerd en toegevoegd worden.

Bibliography

[1] F. Mandl and G. Shaw, *Quantum Field Theory*, John Wiley Sons, New York, 1984.

[2] R. Brout and F. Englert, *Broken symmetry and the mass of gauge vector mesons*, Phys. Rev. Lett.**13**(1964) 321.

[3] P.W. Higgs, *Broken symmetries, massless particles and gauge fields*, Phys. Rev. Lett.**12**(1964) 132, Phys. Rev. Lett.**13**(1964) 508.

[4] LEP Electroweak Working Group, *Preliminary constraints on the Standard Model*, http://lepewwg.web.cern.ch/LEPEWWG/plots/winter2005.

[5] F. Zwirner, *Beyond the Standard Model*, DFPD-98-TH-17 (1998).

[6] M. Peskin, *Beyond the Standard Model*, hep-ph/9705479.

[7] S. Weinberg, *The Quantum Theory of Fields, Vol 3: Supersymmetry*, Cambridge University Press, Cambridge, 2000.

[8] K. Lane, *An introduction to Technicolor*, hep-ph/9401324v2.

[9] R. Peccei, *QCD, strong CP and axions*, hep-ph/9606475.

[10] S. Weinberg, *Theories of the Cosmological Constant*, astro-ph/9610044.

[11] K. Lane, *Two lectures on technicolor*, hep-ph/0202255.

[12] R. Sekhar Chivukula, *Models of Electroweak Symmetry Breaking*, hep-ph/ 9803219v2.

[13] C. Hill and E. Simmons, *Strong Dynamics and Electroweak Symmetry Breaking*, hep-ph/0203079.

[14] S. Dimopoulos and L. Susskind, *Mass without scalars*, Nucl. Phys. B155 (1979).

[15] E.Eichten and K. Lane, *Dynamical breaking of weak interaction symmetries*, Phys. Lett. B90 (1980).

[16] E. Simmons, *Technicolor Evolutions*, www.slac.stanford.edu/econf/C010630/papers/p110.pdf

[17] C.Hill, *Topcolor: top quark condensation in a gauge extension of the standard model*, Phys. Lett. B 266 (1991).

[18] C. Hill, S. Parke, *Top quark production: Sensitivity to new physics*, Phys. Rev. D 49 (1994) 4454.

[19] C.Hill, *Topcolor assisted technicolor*, Phys. Lett. B 345 (1995).

[20] K. Lane, *Symmetry breaking and generational mixing in top-color-assisted technicolor*, Phys. Rev. D 54 (1996) 2204.

[21] R.S. Chivukula, J. Terning, *Precision electroweak constraints on top-color assisted technicolor*, Phys. Lett. B 385 (1996) 209.

[22] K. Lane, *A new model of topcolor-assisted technicolor*, Phys. Lett. B 433 (1998) 96.

[23] R. Lynch, S. Mrenna, M. Narain, E. Simmons, *Finding Z' Bosons Coupled Preferentially to the Third Family at CERN LEP and the Fermilab Tevatron*, hep-ph/0007286 v5.

[24] Y. Su, G.F. Bonini and K. Lane, *Fermilab Tevatron Constraints on Topcolor-Assisted Technicolor*, Phys. Rev. Lett. 79 (1997) 4075.

[25] K.S. Babu, C. Kolda, *The Z' searches*, http://pdg.lbl.gov/ reviews/rppref/mini/2005/zprime.pdf

[26] R. Harris, C. Hill, S. Parke, *Cross section for Topcolor Z'_t decaying to $t\bar{t}$*, Fermilab-FN-687.

[27] A. Kounine, *Search for the technicolour production at LEP*, L3 Collaboration note 2428, contributed paper to the International Europhysics Conference on High Energy Physics 99, Tampere, Finland, 1999.

[28] The D0 Collaboration, *Search for Narrow $t\bar{t}$ Resonances in $p\bar{p}$ Collisions at $\sqrt{s} = 1,8$ TeV*, hep-ex/0307079.

[29] The D0 Collaboration, *Search for a $t\bar{t}$ Resonance in $p\bar{p}$ Collisions at $\sqrt{s} = 1,96$ TeV in the Lepton+Jets Final State*, D0 note 4880-CONF.

[30] The CDF Collaboration, *Search for New Particles Decaying to $t\bar{t}$ in $p\bar{p}$ Collisions at $\sqrt{s} = 1,8$ TeV*, Phys. Rev. Lett. 85 (2000) 2062.

[31] The CDF Collaboration, *Search for resonant $t\bar{t}$ production in $p\bar{p}$ collisions at $\sqrt{s} = 1,96$ TeV*, CDF Note 8087.

[32] CERN Document Server, World Wide Web, http://cdsweb.cern.ch/?c=Thesesas=0ln=en

[33] LHC homepage, World Wide Web, http://lhc.web.cern.ch/lhc/

[34] CMS homepage, World Wide Web, http://cms.cern.ch/

[35] T. Sjöstrand, P. Eden, C. Friberg, L. Lönnblad, G. Miu, S. Mrenna and E. Norrbin, Computer Physics Commun. 82 (1994) 74.

[36] G. Altarelli, M.L. Mangano, *Proceedings of the workshop on Standard Model physics (and more) at the LHC*, CERN-Service d'information scientifique-RD/1001-2000-mai 2000.

[37] G. Altarelli, B. Mele, M. Ruiz-Altaba, *Searching for new heavy vector bosons in $p\overline{p}$ colliders*, Z. Phys. C45 (1989) 109.

[38] *OSCAR: CMS Simulation Package Home Page*, http://cmsdoc.cern.ch/oscar.

[39] GEANT4 Collaboration, S.Agostinelli et al. *GEANT4: A simulation toolkit*, Nucl. Instrum. and Methods A506 (2003) 250-303.

[40] CMS Physics, *Technical Design Report, Volume I: Detector performance and Software*, CERN-LHCC-2006-001

[41] S.V. Chekanov, *Jet algorithms: A mini review*, arXiv:hep-ph/0211298.

[42] J. D'Hondt, S. Lowette, J. Heyninck and S. Kasselman, *Light quark jet energy scale calibration using the W mass constraint in single-leptonic $t\overline{t}$ events*, CMS Note 2006/025 (2006).

[43] R. Frühwirth, P. Kubinec, W. Miratoff and M. Regler, *Vertex reconstruction and track bundling at the LEP collider using robust algorithms*, Comput. Phys. Commun. 96 (1996) 189-208.

[44] J. D'Hondt, P. Vanlaer, R. Frühwirth and W. Waltenberger, *Sensitivity of robust vertex fitting algorithms*, IEEE Trans. Nucl. Sci. 51 (2004) 2037)2044.

[45] T. Speer et al., *Vertex Fitting in the CMS Tracker*, CMS Note 2006/032 (2006).

[46] K. Prokofiev and T. Speer, *A kinematic fit and a decay chain reconstruction library*, CERN 2005-002 (2005).

[47] J. D'Hondt, S. Lowette, J. Heyninck, *Electron and muon reconstruction in single leptonic $t\overline{t}$ events*, CMS Note 2005/024 (2005).

[48] R. Früwirth, *Application of Kalman Filtering to Track and Vertex Fitting*, Nucl. Instrum. and Methods A262 (1987) 444.

[49] V. Innocente, M. Maire and E. Nagy, *GEANE: Average Tracking and Error Propagation Package*, CERN Program Library, IT-ASD W5013-3 (1991).

[50] J. D'Hondt, S. Lowette, O. Buchmüller, S. Cucciarelli, F.-P. Schilling, M. Spiropulu, S. Paktinat Mehdiabadi, D. Benedetti, L. Pape, *Fitting of Event Topologies with External Kinematic Constraints in CMS*, CMS Note 2005/025 (2005).

[51] C. Weiser, *A Combined Secondary Vertex Based B-tagging Algorithm in CMS*, CMS Note 2005/042 (2005).

[52] S. Lowette, J. D'Hondt, J. Heyninck, P. Vanlaer, *Offline Calibration of b-Jet Identification Efficiencies*, CMS Note 2006/013 (2006).

[53] J. Heyninck, J. D'Hondt, S. Lowette, *Top quark mass measurement in single leptonic $t\bar{t}$ events*, CMS Note 2006/066 (2006).

[54] V. Bartsch, G. Quast, *Expected signal observability at future experiments*, IEKP-KA/2003-30.

[55] G.Altarelli, M.L. Mangano, *Proceedings of the workshop on Standard Model physics (and more) at the LHC*, CERN Yellow Report 2000/004.